DIPARTIMENTO
DI INGEGNERIA
DELL'INFORMAZIONE

Università degli Studi di Padova

Dipartimento di Ingegneria dell'Informazione

Corso di Laurea Magistrale in Bioingegneria

Quantitative post-mortem MRI of the human brain: Exploring the impact of temperature and iron on T1 relaxation

Tesi di Laurea Magistrale

Relatrice:

Prof.ssa Alessandra Bertoldo

Co-Relatore:

Dr. Christian Langkammer

Laureanda:

Anna Capponi

2086332

Anno Accademico 2024–2025

Data di laurea: 08/07/2025

Ringraziamenti

Alla mia splendida famiglia, che ha sempre esultato con me per ogni conquista, ma ancor di più mi ha sostenuta nelle cadute.
Grazie mamma, papà e Simone: l'amore incondizionato che mi date ogni giorno è la mia forza più grande.

Agli amici di una vita, che, nonostante la distanza, non ho mai smesso di sentire vicini.
Grazie Elisa, sei la sorella che ho scelto.
Grazie Albi, per esserci sempre.

Alle splendide persone che ho incontrato durante il periodo a Padova, che, in tanti momenti difficili, hanno reso il percorso un po' più leggero.
Grazie Cami, Ele e Carla, per ogni parola scambiata fino a tardi, tra risate leggere e pensieri che pesavano come macigni.

A chi ha reso speciale il mio tempo a Graz, trasformando un'esperienza intensa e impegnativa in un capitolo umano indimenticabile: mai avrei pensato di costruire legami così veri e profondi.
Matteo, Luca e Paola: con voi mi sono sentita a casa.
Max, sono infinitamente grata di averti incontrato.

Infine, ringrazio di cuore tutti i colleghi della Neuroimaging Research Unit, Medical University of Graz, per la gentilezza e disponibilità con cui mi hanno accolta fin dal primo giorno.
Un grazie particolare a Christian, il mio supervisor, per il suo supporto e per aver contribuito ad accendere in me un interesse sempre più vivo per il mondo della ricerca, facendomi apprezzare la sua profondità e complessità.

Alla me stessa di ogni giorno,

che ha tenuto duro, ha creduto,

e ha avuto il coraggio di arrivare fino in fondo.

Abstract

Quantitative magnetic resonance imaging (qMRI) enables non-invasive characterization of brain tissue properties and has become increasingly relevant in *post-mortem* research. In particular, *post-mortem* MRI (PMMRI) allows for high-resolution imaging under controlled conditions, free from motion artifacts and time constraints, and can be directly correlated with histological and biochemical analyses. Among qMRI parameters, the longitudinal relaxation time (T_1) and its inverse (R_1) are sensitive to tissue microstructure, temperature, and iron content—two key modulators of relaxation processes in biological tissues. This study investigates the effect of these variables on T_1 and R_1 in unfixed, *in situ* human brain tissue.

Thirteen *post-mortem* subjects were scanned using a 3T MRI system with a multi-TI turbo spin-echo (IR-TSE) sequence. For each subject, T_1 mapping was performed twice: once at the beginning of the MRI protocol, and once at the end, to capture any intra-scan changes potentially induced by tissue warming. Core body temperature was recorded prior to scanning, and regional iron concentrations were determined *post-mortem* via inductively coupled plasma mass spectrometry (ICP-MS). T_1 and R_1 values were extracted from manually defined regions of interest in the basal ganglia, cortex, and white matter, selected to match the anatomical locations of the tissue samples used for iron quantification. The effects of temperature and iron were analyzed using linear and mixed-effects models.

Results show a significant relationship between T_1 and initial body temperature in gray matter regions (cortex and basal ganglia), with weaker or non-significant trends in white matter. Intra-scan analyses demonstrated a

consistent increase in T_1 from the beginning to the end of the session, likely due to radiofrequency-induced tissue warming. Iron concentration was significantly associated with R_1 in the basal ganglia; however, subregional analyses suggested that this effect may be largely driven by region-specific differences in iron levels rather than a uniform paramagnetic contribution. No consistent association was found in white matter or cortex.

These findings underscore the importance of temperature control and region-specific modeling in post-mortem MRI studies. They highlight the complex interplay between tissue composition, thermal state, and iron in modulating relaxation dynamics, and support the use of multimodal approaches to improve interpretation and comparability with *in vivo* data.

This thesis is the result of an eight-month research period conducted at the Department of Neurology of the Medical University of Graz (Austria), where the entire experimental work, data processing, and interpretation were performed.

La risonanza magnetica quantitativa (qMRI) consente di caratterizzare in modo non invasivo le proprietà del tessuto cerebrale e ha assunto un ruolo sempre più rilevante nella ricerca *post-mortem*. In particolare, la risonanza magnetica *post-mortem* (PMMRI) permette acquisizioni ad alta risoluzione in condizioni controllate, prive di artefatti da movimento e vincoli temporali, offrendo la possibilità di correlare direttamente i dati di imaging con analisi istologiche e biochimiche. Tra i parametri della qMRI, il tempo di rilassamento longitudinale (T_1) e il suo reciproco (R_1) risultano sensibili alla microstruttura tissutale, alla temperatura e al contenuto di ferro: due fattori chiave, spesso difficili da isolare *in vivo*. Questo studio analizza l'effetto di tali variabili su T_1 e R_1 in tessuto cerebrale umano non fissato, acquisito *in situ*.

Tredici soggetti *post-mortem* sono stati sottoposti a scansioni con uno scanner MRI da 3T utilizzando una sequenza turbo spin-echo con inversioni multiple (IR-TSE). Per ciascun soggetto, la mappatura di T_1 è stata effettuata due volte: all'inizio e alla fine del protocollo di acquisizione, al fine di rilevare eventuali variazioni intra-scan dovute al riscaldamento del tessuto. La temperatura corporea interna è stata registrata prima della scansione, mentre le concentrazioni regionali di ferro sono state quantificate tramite spettrometria di massa al plasma accoppiato induttivamente (ICP-MS). I valori di T_1 e R_1 sono stati estratti da regioni di interesse disegnate manualmente nella corteccia, nei gangli della base e nella sostanza bianca, in corrispondenza delle aree anatomiche da cui sono stati prelevati i campioni per l'analisi chimica. Gli effetti della temperatura e del ferro sono stati analizzati mediante modelli lineari e a effetti misti.

I risultati mostrano un'associazione significativa tra T_1 e la temperatura corporea iniziale nelle regioni di sostanza grigia (corteccia e gangli della base), mentre nella sostanza bianca le tendenze sono risultate più deboli o non significative. Le analisi intra-scan hanno evidenziato un incremento costante di T_1 tra l'inizio e la fine della sessione, verosimilmente dovuto al riscaldamento indotto dalla radiofrequenza. La concentrazione di ferro è risultata significativamente associata a R_1 nei gangli della base; tuttavia, le analisi subregionali suggeriscono che tale effetto possa dipendere principalmente da differenze re-

gionali nei livelli di ferro, piuttosto che da un contributo paramagnetico omogeneo. Nessuna associazione consistente è stata osservata nella sostanza bianca o nella corteccia.

Questi risultati sottolineano l'importanza del controllo della temperatura e della modellizzazione specifica per regione negli studi di risonanza magnetica *post-mortem*. Essi mettono in evidenza la complessa interazione tra composizione tissutale, stato termico e contenuto di ferro nella modulazione della dinamica di rilassamento, e supportano l'utilizzo di approcci multimodali per migliorare l'interpretazione dei dati e la loro comparabilità con quelli *in vivo*.

La ricerca è stata interamente condotta nel corso di otto mesi presso il Dipartimento di Neurologia della Medical University of Graz (Austria), che ha messo a disposizione i dati di risonanza magnetica *post-mortem* e le infrastrutture necessarie alle analisi.

Contents

Chapter 1

Introduction

Quantitative magnetic resonance imaging (qMRI) has become an indispensable tool for investigating the structural and biochemical properties of brain tissue, both in clinical and research contexts. Among qMRI parameters, the longitudinal relaxation time (T_1) and its inverse (R_1) are widely used to probe microstructural and compositional features of the brain, offering insight into physiological and pathological processes such as myelination, water content variation, and possibly iron accumulation [1, 2, 3, 4].

In recent years, post-mortem MRI (PMMRI) has gained increasing relevance as a complementary approach to in vivo imaging, enabling high-resolution acquisitions under controlled conditions and facilitating direct correlation with histological and biochemical analyses. PMMRI is particularly suited for exploring factors that modulate relaxation properties, such as temperature and iron content, which may be difficult to isolate in living subjects. However, the interpretation of T_1 (and R_1) values in post-mortem settings is complicated by a range of variables, including tissue degradation, absence of thermoregulation, and altered metabolic states [5, 6, 7].

Temperature is a critical determinant of relaxation behavior in biological tissues [8, 9, 10]. In the absence of active heat dissipation, post-mortem samples are subject to RF-induced heating [11] and passive equilibration toward room temperature [12] during MRI acquisition. This thermal drift can lead to significant changes in T_1 values over the course of a scan and must be accounted for in both experimental design and data interpretation. Furthermore, differences in initial temperature across subjects may affect inter-individual comparisons, especially when extrapolating T_1 to physiological values *in vivo*.

Iron is another key modulator of relaxation, particularly relevant in deep gray matter structures where it is higher than in other tissues [1, 13, 14]. Its paramagnetic properties influence local magnetic field inhomogeneities, thereby enhancing proton relaxation [15]. However, the relationship between iron and R_1 is complex and may be confounded by other tissue-specific factors, such as myelin content, compartmentalization, water content, or temperature [1, 16, 17].

This thesis investigates how temperature and iron concentration influence

longitudinal relaxation in unfixed, in situ post-mortem human brain tissue. By combining quantitative MRI with inductively coupled plasma mass spectrometry (ICP-MS) measurements of regional iron levels, this study aims to characterize the biophysical mechanisms underlying relaxation variability and to assess the robustness of T_1 under post-mortem conditions.

Specifically, the objectives of this work are:

- To evaluate the effect of temperature on T_1 values across major brain regions using regression models;
- To assess intra-scan changes in T_1 as an indirect marker of tissue warming during MRI acquisition;
- To explore the relationship between iron concentration and R_1, both at regional and subregional levels, using linear and mixed-effects models.

The thesis is organized as follows. Chapter 2 provides a theoretical background on T_1 relaxation mechanisms, the role of temperature and iron in MRI, and the specific characteristics of post-mortem imaging. Chapter 3 describes the experimental methods, including subject selection, MRI acquisition protocols, T1 mapping, iron quantification, and statistical analyses. Chapter 4 presents the results of temperature and iron analyses, while Chapter 5 discusses their physiological and methodological implications. The work concludes with a synthesis of findings and future research directions.

Chapter 2

Theory and State of the Art

Magnetic Resonance Imaging (MRI) is an advanced non-invasive imaging technique widely used in both clinical and research fields to obtain detailed information about the structure and composition of biological tissues, particularly within the central nervous system. MRI provides high-resolution images without the use of ionizing radiation, making it especially valuable for studying the human brain *in vivo*, due to its safety profile and non-destructive nature [18].

In recent years, MRI has also become increasingly relevant in *postmortem* studies, providing new insights into tissue microstructure and pathology under controlled experimental conditions [6]. These postmortem approaches enable detailed examinations that are otherwise challenging in vivo, due to practical, ethical, or methodological constraints.

Quantitative MRI parameters, such as T_1, T_2, T_2^* and Magnetization Transfer Ratio (MTR), are routinely employed to investigate the physical and biological characteristics of brain tissue [19]. These parameters are influenced by several biological factors, including myelin content, iron deposition, and water concentration, whose variations significantly modulate the MRI signal. Additionally, temperature plays a significant role in modulating these MRI parameters by affecting molecular mobility and proton relaxation mechanisms [20].

A thorough understanding of how these factors modulate the MRI signal is crucial for interpreting tissue properties and identifying abnormalities associated with various neurological disorders [21, 22, 23].

2.1 T_1 Longitudinal Relaxation Time

Physical Basis of Longitudinal Relaxation

The longitudinal relaxation time, denoted as T_1, is a fundamental parameter in magnetic resonance imaging (MRI) that describes the rate at which nuclear magnetization returns to its equilibrium state along the direction of the static magnetic field B_0 after perturbation by a radiofrequency (RF) pulse. This energy exchange process between the spin system and its molecular environ-

ment—commonly referred to as the *lattice*—is known as *spin-lattice relaxation*.

When RF radiation is applied at or near the Larmor frequency, it perturbs the magnetization from its equilibrium alignment. Once the RF pulse is turned off, the system relaxes back to equilibrium, releasing the absorbed energy. This recovery of the longitudinal magnetization M_z follows an exponential behavior governed by T_1. In absence of further perturbations, the evolution of M_z is described by the Bloch equation:

$$\frac{dM_z(t)}{dt} = \frac{M_0 - M_z(t)}{T_1} \tag{2.1}$$

where $M_z(t)$ is the longitudinal component of the net magnetization at time t, M_0 is the equilibrium magnetization along the static magnetic field B_0, and T_1 is the longitudinal relaxation time. This first-order differential equation describes the exponential recovery of M_z toward its equilibrium value after RF excitation. The mono-exponential recovery of the longitudinal magnetization is given by:

$$M_z(t) = M_0 \left(1 - e^{-t/T_1}\right) \tag{2.2}$$

The theoretical recovery curve shown in Figure 2.1 demonstrates the exponential return of $M_z(t)$ toward equilibrium. By convention, the time point at which $M_z(t)$ reaches 63 % of its final value is defined as the longitudinal relaxation time T_1. This definition reflects the characteristic timescale of energy transfer from the spin system to its molecular environment.

At the microscopic level, longitudinal relaxation arises from the interaction between nuclear magnetic moments (spins) and fluctuating magnetic fields in their molecular environment. These fluctuations are primarily caused by random rotational and translational motions of molecules that modulate the local magnetic field experienced by each spin. The energy exchange with the lattice occurs efficiently only when the frequency of these fluctuations matches the Larmor frequency ω_0 of the nuclear spin.

This process is described in quantum mechanical terms as a transition between energy states of the spin system, mediated by dipole-–dipole coupling.

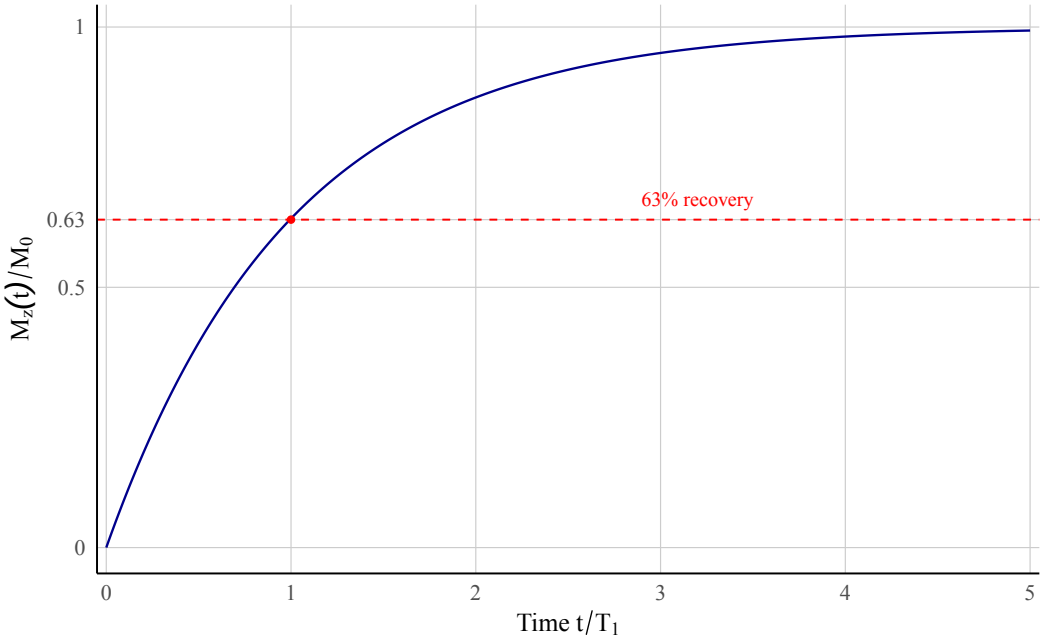

Figure 2.1: Normalized exponential recovery of the longitudinal magnetization $M_z(t)/M_0$ as a function of time, expressed in units of the longitudinal relaxation time T_1. The red dot marks the point at $t = T_1$, where the magnetization reaches 63% of its equilibrium value.

The probability of such transitions depends on the spectral density $J(\omega_0)$ of the local magnetic field fluctuations at ω_0. Relaxation is most efficient when the characteristic timescale of molecular motion, given by the correlation time τ_c, satisfies the condition $\omega_0\tau_c \approx 1$. If molecular motion is too fast ($\omega_0\tau_c \ll 1$) or too slow ($\omega_0\tau_c \gg 1$), energy exchange becomes inefficient, resulting in longer T_1 values.

The rate of longitudinal relaxation thus depends on the efficiency of dipole–dipole interactions between water protons and nearby molecules, making T_1 a sensitive marker of water mobility, molecular binding, and tissue microstructure. This principle explains why tissues with restricted water mobility—such as myelinated white matter—generally exhibit shorter T_1 values due to more effective spin-lattice coupling.

T_1 Mapping via Inversion Recovery

A widely used and robust technique for measuring longitudinal relaxation times in MRI is the *inversion recovery* (IR) sequence. This method provides accurate

T_1 estimates and is considered the gold standard for quantitative T_1 mapping.

In IR sequences, the longitudinal magnetization is initially inverted by applying a 180° radiofrequency (RF) pulse, which flips the magnetization vector from $+M_0$ to $-M_0$. Following this inversion, the system is allowed to recover towards equilibrium along the z-axis for a variable inversion time (TI), after which a 90° pulse is applied to bring the partially recovered magnetization into the transverse plane. The resulting signal–commonly acquired as a free induction decay (FID)–is proportional to the z-component of magnetization at time TI.

The measured signal as a function of inversion time follows the expression:

$$S(TI) = S_0 \left(1 - 2e^{-TI/T_1}\right) \tag{2.3}$$

where $S(TI)$ is the signal at inversion time TI, S_0 is the fully recovered equilibrium signal, and T_1 is the longitudinal relaxation time. The factor 2.0 arises from the assumption of a perfect 180° inversion pulse. In practice, deviations from this ideal condition—such as RF pulse imperfections or B_1 inhomogeneities—can lead to reduced inversion efficiency. For this reason, the factor is often treated as a fit parameter (e.g., α), yielding a generalized form of the recovery equation:

$$S(TI) = S_0 \left(1 - \alpha e^{-TI/T_1}\right) \tag{2.4}$$

where α is typically close to 2 and reflects the effective inversion efficiency.

By repeating the sequence across multiple TI values and fitting the resulting signal curve to the equation above, it is possible to accurately estimate T_1. To ensure full magnetization recovery between acquisitions, a repetition time (TR) of at least $5T_1$ is typically used, making the method relatively time-consuming. However, its accuracy and straightforward biophysical interpretation make it particularly suitable for quantitative studies.

Figure 2.2 illustrates the signal recovery process in an inversion recovery sequence, showing both the theoretical curve and simulated measurements at

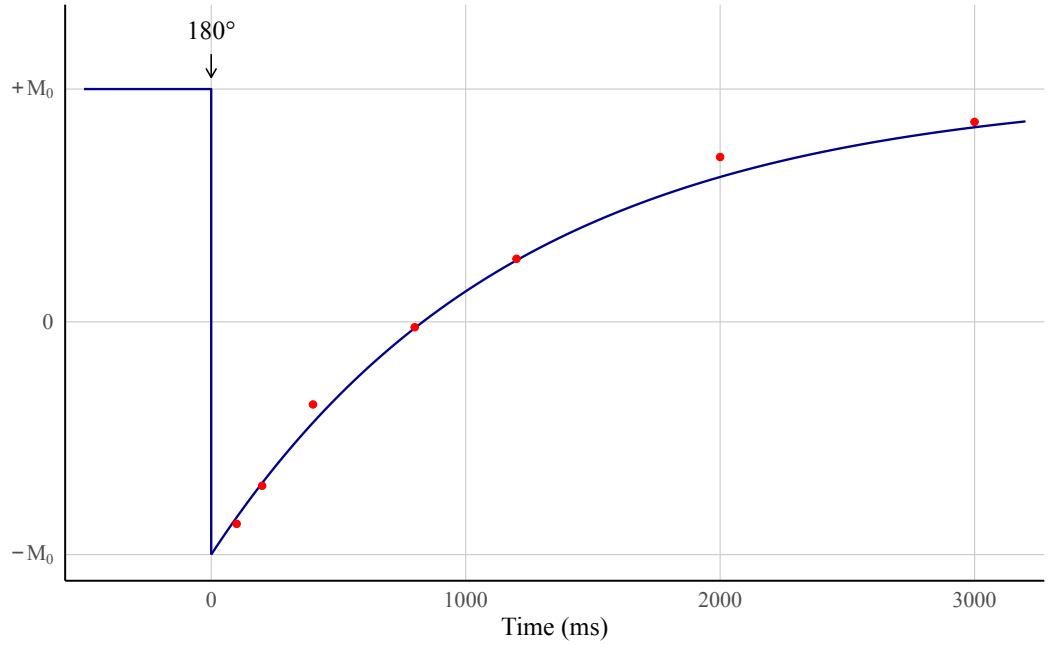

Figure 2.2: Illustration of the variation in signal amplitude as a function of inversion time (TI) in an inversion recovery (IR) sequence. Following a 180° RF pulse at $t = 0$, the longitudinal magnetization inverts from $+M_0$ to $-M_0$ and then recovers exponentially toward equilibrium. The black curve represents the theoretical signal model $S(TI) = S_0(1 - 2e^{-TI/T_1})$, while red points illustrate simulated measurements for visual demonstration.

different inversion times.

T_1 in Different Brain Tissues

T_1 values vary considerably across brain tissues due to differences in water content and macromolecular density. The presence of paramagnetic substances, such as iron, may also contribute to longitudinal relaxation, although their effects can be complex and region-dependent. These microstructural characteristics influence spin–lattice interactions and contribute to intrinsic MRI contrast.

White matter has shorter T_1 values, primarily due to its high myelin content. Myelin creates a structured microenvironment that restricts water mobility and enhances dipole–dipole coupling, accelerating longitudinal relaxation [24]. At 3T, typical white matter T_1 values are around 838 ± 50 ms [25].

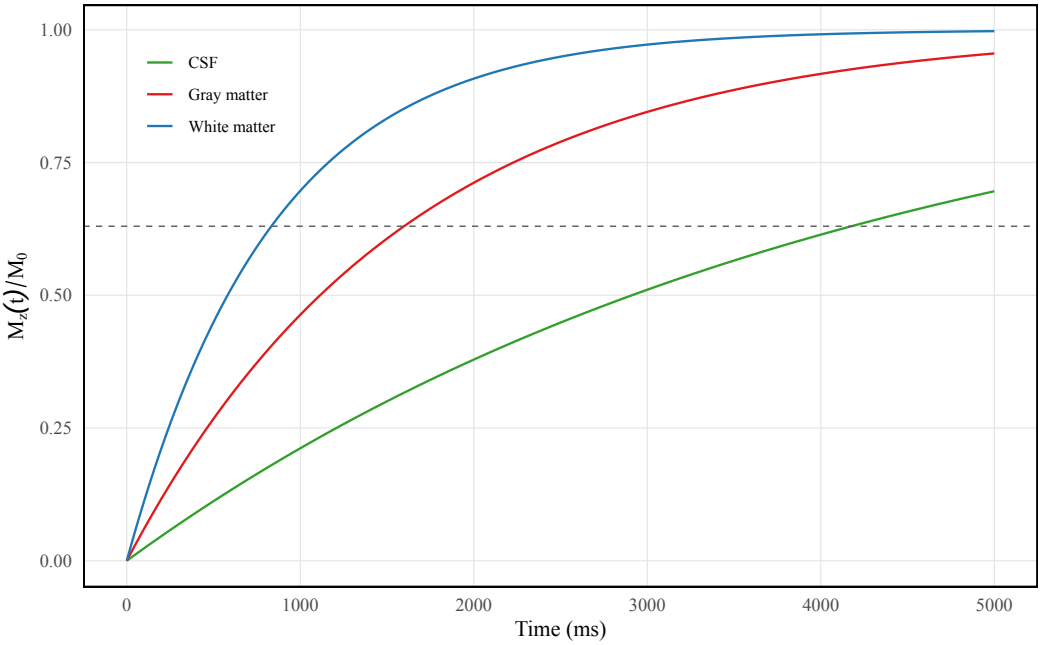

Figure 2.3: Simulated longitudinal magnetization recovery curves $M_z(t)/M_0$ for cerebrospinal fluid (CSF), gray matter (GM), and white matter (WM), modeled using the standard exponential recovery function. The T_1 values used correspond to those reported at 3T: 838 ms for white matter, 1607 ms for gray matter, and 4200 ms for CSF. The dashed line marks the 63% recovery threshold, which by definition corresponds to one T_1.

Gray matter shows intermediate T_1 values, influenced by moderate macromolecular density and iron deposition. Paramagnetic iron shortens T_1 by increasing local magnetic field inhomogeneities [19]. At 3T, cortical gray matter and deep nuclei exhibit T_1 values of approximately 1607 ± 112 ms and 1363 ± 58 ms, respectively [26].

Cerebrospinal fluid (CSF) has the longest T_1 values, due to its high free water content and low interaction with macromolecules. Typical values at 3T range from 3900 to 4426 ms [27].

To visually illustrate these differences, Figure 2.3 shows the simulated recovery curves of longitudinal magnetization for white matter, gray matter, and CSF using the typical T_1 values reported above. The exponential nature of T_1 relaxation is evident, as well as the progressively slower recovery in tissues with longer T_1. The dashed line marks the 63% recovery threshold, corresponding to one time constant T_1.

Biological and Pathological Modulation of T_1

In biological tissues, T_1 is modulated by several factors: water content, molecular mobility, water binding to macromolecules, and local magnetic field heterogeneities. Changes in these parameters under pathological conditions can alter the T_1 value significantly.

In multiple sclerosis (MS), acute lesions with vasogenic edema and inflammation show prolonged T_1, due to increased water content. Chronic lesions, where myelin loss predominates, also exhibit elevated T_1 values. Conversely, the rim of active MS lesions may present reduced T_1 because of debris accumulation acting as relaxation centers. Similarly, T_1 is increased in brain tumors and areas of inflammation, whereas iron accumulation (e.g., in Parkinson's disease) shortens T_1 due to paramagnetic effects.

Clinical Relevance of T_1 Mapping

Beyond its role in characterizing tissue composition, T_1 mapping has gained increasing attention in both clinical and research settings as a quantitative imaging biomarker. Changes in T_1 relaxation times can indicate pathological alterations such as demyelination, edema, gliosis, or abnormal iron deposition.

As a non-invasive and contrast-free technique, T_1 mapping is particularly valuable in longitudinal studies, allowing for the monitoring of disease progression and therapeutic response across a wide range of neurological disorders, including multiple sclerosis, Alzheimer's disease, and brain tumors [19].

Moreover, in dynamic contrast-enhanced studies, the presence of paramagnetic contrast agents such as Gd-DTPA significantly reduces T_1 by increasing local relaxation rates. This property enables quantitative monitoring of contrast agent concentration and has been employed to assess blood–brain barrier integrity and cerebral perfusion.

2.2 R_1 Longitudinal Relaxation Rate

Definition and Modeling Relevance

The longitudinal relaxation rate, R_1, is defined as the inverse of the T_1 relaxation time:

$$R_1 = \frac{1}{T_1} \tag{2.5}$$

The recovery of magnetization can equivalently be described in terms of R_1 as:

$$M_z(t) = M_0 \left(1 - e^{-R_1 \cdot t}\right) \tag{2.6}$$

While T_1 is commonly used to describe physical tissue properties, expressing longitudinal relaxation as a rate (R_1) is often advantageous in quantitative modeling and regression analyses, as it allows for linear relationships with underlying tissue components. In particular, the effect of iron accumulation on relaxation can be modeled by assuming an additive contribution to the relaxation rate:

$$R_1 = R_{1,0} + R_{1,C} \cdot [\mathrm{Fe}] \tag{2.7}$$

where R_1 is the observed longitudinal relaxation rate, $R_{1,0}$ is the baseline rate in the absence of excess iron, $R_{1,C}$ is the effective longitudinal relaxivity (slope) relating iron content to R_1, and [Fe] is the tissue iron concentration. This linear model is used in relaxometry to quantify the specific contribution of paramagnetic species such as iron to R_1, and forms the basis for regression-based estimation of tissue iron content.

Factors Influencing R_1

Since R_1 is mathematically derived from T_1, it is influenced by several biological and physical parameters, including water mobility and compartmentalization, macromolecular binding, myelin content, the presence of paramagnetic species

(e.g., iron), and temperature.

Notably, iron and myelin shorten T_1 via distinct mechanisms: iron accelerates spin-lattice relaxation through local magnetic field inhomogeneities, while myelin reduces water mobility and enhances dipole–dipole interactions.

These mechanisms are particularly relevant in post-mortem imaging, where altered temperature and lack of perfusion can modify relaxation dynamics.

Clinical Applications

Understanding R_1 differences across brain tissues is essential for quantitative MRI, as it enables the identification of healthy versus pathological tissue states. Alterations in R_1 can serve as valuable biomarkers for a variety of conditions characterized by structural or biochemical changes, such as demyelination, inflammation, and neurodegeneration.

Quantitative R_1 mapping has been used to non-invasively assess tissue integrity, detect subtle pathological changes, and monitor disease progression in neurological disorders including multiple sclerosis, Alzheimer's disease, and Parkinson's disease [19]. As both myelin and iron influence R_1, it is considered a composite marker reflecting multiple microstructural features. However, disentangling their respective contributions remains a challenge in quantitative MRI. In particular, the effect of iron on R_1 is modulated by several factors, including myelin content, tissue microstructure, and the presence of pathological changes. While increased iron levels may locally enhance R_1, similar changes can also arise from demyelination, edema, or other tissue alterations. This complexity makes interpretation of R_1 values challenging and the subject of ongoing research.

2.3 Post-Mortem MRI

Post-mortem MRI (PMMRI) has emerged as a valuable tool in forensic and biomedical research, offering a non-invasive alternative or complement to conventional autopsy, e.g. the investigation of trauma victims [28, 29]. It also

serves as a powerful bridge between in vivo neuroimaging and histological validation [30], enabling the acquisition of ultra-high-resolution images under controlled conditions, free from motion artifacts and scan time constraints that are inherent to in vivo imaging [31]. These advantages allow for extended acquisition protocols with high signal-to-noise ratio (SNR), particularly when using ultra-high-field scanners [32, 33, 34]. Such features make PMMRI especially suitable for studying the microstructural and biochemical underpinnings of MRI contrast mechanisms, with potential implications for the development of imaging biomarkers in neurodegenerative diseases.

The primary goal of PMMRI is to replicate as closely as possible the image contrast observed under in vivo conditions. However, this goal is challenged by several technical and biological limitations inherent to the post-mortem setting. There are three main approaches for post-mortem brain MRI acquisition: (i) *in situ* MRI of the intact body, (ii) *ex vivo* MRI of the extracted brain, and (iii) MRI of individual brain slices. The last two can be performed either on unfixed or fixed tissue. The choice of method significantly influences image quality, as well as the interpretability and generalizability of results.

Several factors impact the success of a post-mortem MRI study, beginning with the biological processes that occur after death. Autolysis and tissue degradation lead to an increase in water content and a reduction in pH, both of which alter the tissue's composition and microstructural properties. In particular, the drop in pH—mainly caused by lactic acid accumulation due to anaerobic glycolysis—can affect protein conformation, membrane integrity, and water–macromolecule interactions. Although pH was not directly measured, *Tashiro et al.* [7] suggest that reduced pH contributes to the prolongation of T_2 observed in post-mortem brain tissue, in agreement with similar findings in animal models [35]. However, no direct correlation between reduced pH and T_1 has been reported, and its influence on longitudinal relaxation remains unclear, likely being negligible compared to the dominant effects of temperature and tissue hydration. These biochemical changes, together with increased water content and decreased temperature, significantly impact MRI contrast and quantitative parameters.

The post-mortem interval (PMI)—the period between death and MRI acquisition—is a particularly influential factor, as a longer interval allows for more pronounced degradation processes that can distort the MRI signal.

In addition to PMI, the preparation of tissue is a key consideration. Whole extracted brains or brain slices can be measured in either unfixed or fixed conditions, with fixation solutions influencing both the contrast and quantitative MR parameters [9, 36, 37]. In particular, chemical fixation using formaldehyde alters tissue biochemistry and microstructure, modifying relaxation times, diffusion properties, and susceptibility effects [36, 38, 39]. This process differs substantially from thermal changes: while fixation induces long-term alterations through cross-linking of proteins and membrane stabilization [40], temperature-related changes are dynamic and reversible, primarily modulating water mobility and relaxation behavior. It is therefore essential to distinguish between these two types of effects when designing and interpreting post-mortem MRI studies.

Another critical factor is temperature, which profoundly influences tissue biophysics and MRI signal characteristics. Unlike in vivo conditions—where tissue heating caused by radiofrequency (RF) pulses is counteracted by active thermoregulatory mechanisms such as blood vessel dilatation and perfusion—post-mortem tissue lacks any physiological heat dissipation. Consequently, during MRI acquisition, tissue temperature passively drifts toward the ambient environment. If the specimen was initially colder (e.g., after refrigeration), this drift leads to warming; if warmer, it leads to cooling. This passive equilibration is further compounded by RF-induced heating during high-SAR or prolonged MRI acquisitions [31].

Such heating has direct implications for both image stability and the interpretation of quantitative MRI parameters, including relaxation times and diffusion coefficients, which are known to be temperature-dependent [20, 41, 42, 43]. Furthermore, in unfixed tissue, increased temperature may accelerate enzymatic degradation and bacterial activity [44], introducing variability and potential artifacts that compromise both imaging and downstream histological validation [31].

Finally, the temperature at the time of acquisition must be carefully considered when comparing post-mortem and in vivo data. While in vivo MRI is typically performed at physiological core body temperature (∼37°C), post-mortem imaging is often conducted at room temperature or lower due to cooling. This temperature discrepancy affects both MR signal intensity and relaxation behavior and therefore must be accounted for when interpreting results or attempting to extrapolate them to physiological conditions.

The following section explores in detail the influence of temperature on quantitative MRI metrics, with a particular focus on its effects on longitudinal relaxation time (T_1).

Effect of Temperature on T_1 Relaxation Time

Previous studies have demonstrated that temperature significantly influences spin-lattice relaxation (T_1) by affecting the translational and rotational motion of hydrogen protons [20, 42]. A key contribution to this understanding comes from *Nelson et al.* [20], who proposed two main models to explain the behavior of T_1 and T_2 as a function of temperature and frequency: the *Molecular Motion Model* and the *Fast Exchange Two States* (FETS) model.

Molecular Motion Model

According to the *Molecular Motion Model*, biological tissues consist mainly of liquids within a solid framework, with molecules in rapid and random motion. The molecular mobility is characterized by the correlation time τ_c, defined as the average time a molecule persists in the same position before a collision causes a change in its state or motion. For small molecules such as water, the correlation time τ_c is inversely proportional to the absolute temperature (T) and directly related to fluid viscosity η, as expressed by the following relationship:

$$\tau_c = \frac{4\eta a^3}{k_B T} \tag{2.8}$$

where a is the radius of the molecule treated as a sphere, and k_B is the

Boltzmann constant. The model assumes that proton relaxation is predominantly driven by dipolar interactions between water protons. The relationship between the longitudinal relaxation rate (T_1) and τ_c is mathematically described by:

$$\frac{1}{T_1} = C\left(\frac{2\tau_c}{1+\omega_0^2\tau_c^2} + \frac{8\tau_c}{1+4\omega_0^2\tau_c^2}\right) \tag{2.9}$$

where C is a constant depending on the gyromagnetic ratio and the internuclear distance for protons and ω_0 is the Larmor frequency. Fig. 2.4 shows a log-plot of relaxation time versus τ_c reproduced from *Nelson and Tung* [20].

In the limit of rapid molecular motion, i.e., when the condition $\omega_0\tau_c \ll 1$ is satisfied—which typically holds for water protons at standard MRI frequencies and physiological temperatures—the expression for $1/T_1$ simplifies considerably. Under this approximation, the model predicts a linear relationship between T_1 and temperature, and an inverse dependence on viscosity:

$$T_1 \propto \frac{T}{\eta} \tag{2.10}$$

This simplified form is valid over a narrow temperature range (e.g., $\sim$ 40°C) and reflects the fact that higher temperatures or lower viscosities increase molecular mobility, thereby prolonging the longitudinal relaxation time. In this regime, protons experience rapidly fluctuating local magnetic fields, which facilitates efficient energy exchange with the lattice and governs the temperature dependence of relaxation.

Fast Exchange Two-State Model (FETS)

The *Fast-Exchange Two-State Model (FETS)* extends the simple molecular motion framework to account for more complex biological environments, such as tissues with multiple water compartments or aqueous solutions of paramagnetic ions. In this model, water protons are assumed to exchange rapidly between two compartments: (i) a free compartment consisting of bulk-water (usually comprising >90% of total water), and (ii) a bound compartment, where

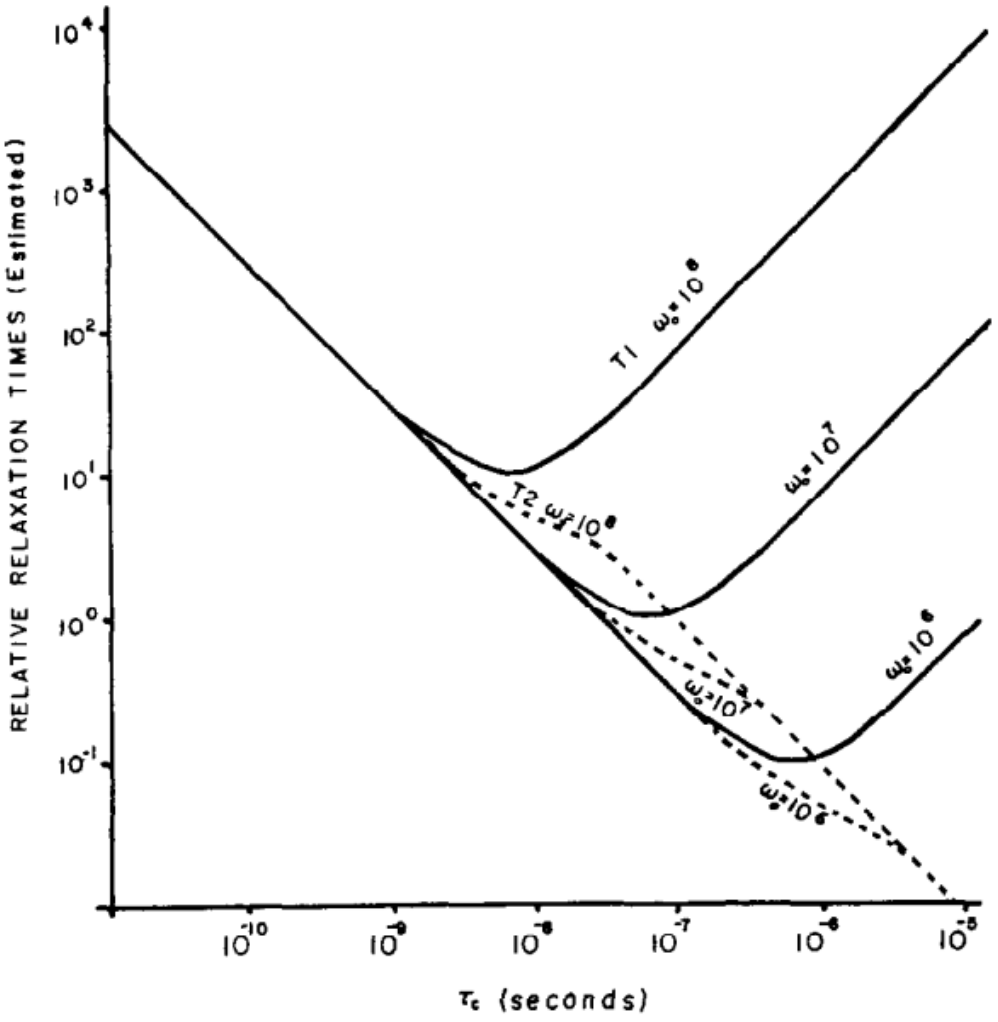

Figure 2.4: A log-log plot of relaxation times versus τ_c for both T_1 and T_2 (dashed line), reproduced from [20]. The plot is divided into three regions: (i) when $w_0\tau_c > 1$, the spin-lattice relaxation time (T_1) depends on both the Larmor frequency (w_0) and the correlation time (τ_c); (ii) when $w_0\tau_c = 1$, T_1 reaches its minimum value when the average molecular tumbling frequency is equal to the nuclear precession frequency; (iii) when $w_0\tau_c \ll 1$, both T_1 and T_2 depend only on τ_c, and not on w_0. This is typically true for pure water at MRI frequencies ($w_0 < 60$ MHz).

water molecules form structured hydration layers around macromolecules, restricting their motion. The two compartments exhibit significantly different relaxation behaviors: free water generally displays longer T_1 values, whereas bound water exhibits much shorter relaxation times due to restricted motion. The observed longitudinal relaxation rate is modeled as a weighted average of the two compartments:

$$\frac{1}{T_1} = \frac{b}{T_{1b}} + \frac{1-b}{T_{1f} + \tau_e} \tag{2.11}$$

where T_{1b} and T_{1f} are the T_1 values for bound state and free state water, respectively, τ_e is the residence time of a proton in the restricted compartment, and b is the fractional volume of bound water. Typically, $\tau_e << T_{1f}$, thus it can be often neglected when considering free water dominance. In the free compartment, rotational and translational motions are coupled and characterized by a single correlation time ($\tau_c \sim 1$ ps), generally considered frequency-independent. The temperature dependence of T_{1f} can be approximated by Arrhenius-like relation:

$$T_{1f} \propto e^{\frac{-E_{af}}{k_B T}} \tag{2.12}$$

where E_{af} is the activation energy for relaxation in the free state. Conversely, bound water is characterized by restricted molecular motion and structural ordering, resulting in a broad distribution of correlation times. This distribution can be effectively modeled using a log-Gaussian distribution $g(\tau_{gb})$:

$$g(\tau_{cb}) = \frac{\alpha}{\tau_{cb}\sqrt{\pi}} e^{-\left(\alpha ln \frac{\tau_{cb}}{\tau_0}\right)^2} \tag{2.13}$$

where both α and τ_0 are empirically temperature-dependent constants. However, over a narrow temperature range (e.g., ~ 40°C), the distribution $g(\tau_{gb})$ and consequently T_{1b} remain relatively constant. Thus, when relaxation is primarily dominated by the free water (typical in most biological tissues), the overall T_1 temperature dependence can still be effectively approximated by:

$$T_1 \propto e^{\frac{-E_A}{k_B T}} \tag{2.14}$$

where E_a is an empirical parameter. Over a narrow temperature range (e.g., $\sim 40°$C), this exponential dependence can be locally approximated by a linear relationship. Regarding transverse relaxation (T_2), it generally exhibits weaker sensitivity to temperature variations than T_1, particularly when influenced by exchange phenomena, molecular diffusion, and compartmental heterogeneity. Therefore, the FETS model provides a more comprehensive and physiologically realistic framework than simpler single-compartment models for interpreting relaxation dynamics in biological tissues. In summary, it offers a robust theoretical basis for understanding temperature-dependent T_1 relaxation in post-mortem brain tissue, accounting for compartmental water dynamics, molecular mobility, and proton exchange.

Several studies have investigated the relationship between temperature and the longitudinal relaxation rate in post-mortem brain MRI, highlighting the temperature sensitivity of different brain compartments. *Birkl et al.* [9, 36] conducted studies on fresh post-mortem brain slices subjected to controlled heating using a 3T MRI scanner. Their regression models demonstrated that T_1 exhibits the strongest temperature dependence in the cortex, followed by the basal ganglia and white matter, confirming that different brain compartments have distinct temperature coefficients.

Other studies have examined temperature effects on relaxation parameters in post-mortem MRI using a 1.5T scanner, with core temperature assessment as a key factor (*Ruder et al.* [8], *Flach et al.* [45], *Busch et al.* [46], *Scheurer et al.* [47], *Tashiro et al.* [7], *Zech et al.* [48]). Specifically, *Zech et al.* [48] investigated the influence of temperature on relaxation parameters *in situ*, using esophageal measurements to assess core temperature. *Toft et al.* [49] proposed a correction method based on the diffusion constant in the cerebrospinal fluid (CSF), tested on two post-mortem samples with enlarged ventricular volumes.

Further *in situ* studies monitored brain temperature directly. *Berger et al.* [10] found a significant correlation between T_1 and temperature, with a

stronger sensitivity in certain brain structures, consistent with the results of *Birkl et al.* [9, 36]. In a separate study, *Berger et al.* [50] monitored forehead temperature and observed comparable effects when considering both forehead and brain temperature.

2.4 The Role of Iron in the Brain

Iron Homeostasis and Distribution in the Brain

Iron is a crucial element in the brain, involved in a wide range of biological processes, including oxygen transport, mitochondrial energy production, myelin synthesis, and neurotransmitter synthesis and metabolism [51].
MRI techniques—particularly phase imaging, relaxation-based methods, and susceptibility mapping—are commonly employed to estimate regional iron distribution in the living brain [52]. Post-mortem studies using single-origin tissue have confirmed that iron is unevenly distributed in the brain, with highly compartimentalized concentrations in specific anatomic regions [53]. In areas such as the basal ganglia and thalamus, iron plays a crucial physiological role [54], acting both as a reservoir and as a cofactor in essential enzymatic processes [55].
Average iron concentrations across different brain regions are summarized in Table 2.1.

The transport of iron into the brain is tightly regulated, primarily through receptor-mediated endocytosis of iron-bound transferrin at the blood-brain barrier [57]. After crossing the barrier, non-transferrin-bound iron is released into the brain interstitium, where it contributes to mantaining iron homeostasis, which is essential for maintaining neuronal health and function [58].

Iron Storage Mechanisms: Ferritin and Hemosiderin

In the brain, iron is primarily stored in two forms: ferritin (Ft) and hemosiderin (Hm). Ferritin, a protein complex made of heavy (H) and light (L) subunits, is the main iron storage molecule, responsible for accumulating more than

Region	**N**	**Iron Concentration (mg/kg)**	**Reference**
Globus Pallidus	25	205 ± 39	[53]
Putamen	49	160 ± 37	[53]
Caudate Nucleus	49	105 ± 27	[53]
Thalamus	49	50 ± 12	[53]
Corpus Callosum	67	29 ± 10	[53]
Frontal WM	73	47 ± 11	[53]
Temporal WM	72	46 ± 11	[53]
Occipital WM	73	36 ± 9	[53]
Frontal CX	6	25.5 ± 6	[56]
Occipital CX	6	40.7 ± 10	[56]

Table 2.1: Chemically determined mean iron concentrations grouped by brain regions. Values are expressed in mg/kg of wet tissue.

Values are given as mean ± standard deviation (inter-quartile range).
N represents the number of samples included in the analysis.
WM = white matter.
CX = cortex.

90% of non-heme iron. It can store iron in a non-toxic and redox-inert form, with ferric iron (Fe^{3+}) stored as hydratetd iron oxide nanocrystals, commonly referred to as ferrihydrite ($5Fe_2^{3+}O_3 \cdot 9H_2O$) [55].

Iron's ability to transition between its ferrous (Fe^{2+}) and ferric (Fe^{3+}) oxidation states plays a crucial role in regulating the balance between iron absorption, utilization, and storage. These redox reactions are central to the formation of reactive oxygen species (ROS) and include the well-known Fenton reaction and related Fenton-like processes. In the classic Fenton reaction, ferrous iron reacts with hydrogen peroxide to produce ferric iron, hydroxyl radicals, and hydroxide ions (equation 2.15). Conversely, under certain conditions, ferric iron can be reduced back to the ferrous form via a Fenton-like reaction, generating a hydroperoxyl radical and a proton (equation 2.16).

$$\mathrm{Fe^{2+} + H_2O_2 \longrightarrow Fe^{3+} + HO\bullet + OH^-} \tag{2.15}$$

$$\mathrm{Fe^{3+} + H_2O_2 \longrightarrow Fe^{2+} + HOO\bullet + H^+} \tag{2.16}$$

When ferritin storage capacity is exceeded, excess iron forms hemosiderin, a less soluble form and less easily mobilized form of iron. Hemosiderin is generally considered a ferritin degradation product and tends to accumulate in areas where iron regulation is impaired. Its presence has been associated with pathological conditions such as hemochromatosis, in which iron overload causes tissue damage [55].

The Role of Iron in Neurodegenerative Disorders

The balance between ferritin and hemosiderin is essential for preventing oxidative damage in the brain, as it reflects the equilibrium between safely stored and potentially reactive iron pools. When the buffering capacity of ferritin and hemosiderin is exceeded, unbound iron accumulates in its free form, catalyzing the production of reactive oxygen species (ROS). These ROS contribute to oxidative stress, ultimately promoting neuronal injury and degeneration [52,

59]. Under physiological conditions, such redox reactions are tightly regulated to maintain iron homeostasis and safeguard neuronal integrity. However, excessive iron accumulation has been implicated in various neurodegenerative disorders [60], including Parkinson's disease, Alzheimer's disease, and multiple sclerosis [61, 62, 63, 17]. Thus, preserving iron balance is critical for brain health and for preventing iron-mediated neurotoxicity [64]. The following section explores age-related changes in cerebral iron metabolism and how these alterations may contribute to the development of age-related neurodegenerative disorders.

Iron Accumulation in the Aging Brain

Iron accumulation in the brain is a progressive process that begins shortly after birth and continues throughout life. With age, iron accumulates progressively in multiple regions of the brain, although the rate and extent of deposition vary substantially across regions [65].

One of the most influential studies on this topic is the seminal work by Hallgren and Sourander [54], which quantitatively analyzed how non-heme iron concentrations vary across the lifespan in different brain areas. Their results demonstrated a consistent age-related increase in iron content in all investigated regions—except for the medulla oblongata—based on post-mortem samples from subjects spanning a wide age range. This accumulation is particularly evident in areas of the extrapyramidal system—including the globus pallidus, putamen, and caudate nucleus—as well as in cortical areas, gray and white matter. Notably, the rate of iron accumulation differs among brain regions, as reflected by the varying slopes of their accumulation curves. Despite this variability, most regions tend to reach a plateau during adulthood. For illustration, Fig.2.5 and Fig.2.6, reproduced from Hallgren 's study [54], show the distinct age-related iron accumulation patterns in the putamen and various cortical regions, respectively.

The causes of iron accumulation in brain aging are complex and include factors such as increased blood-brain barrier permeability, inflammation, and

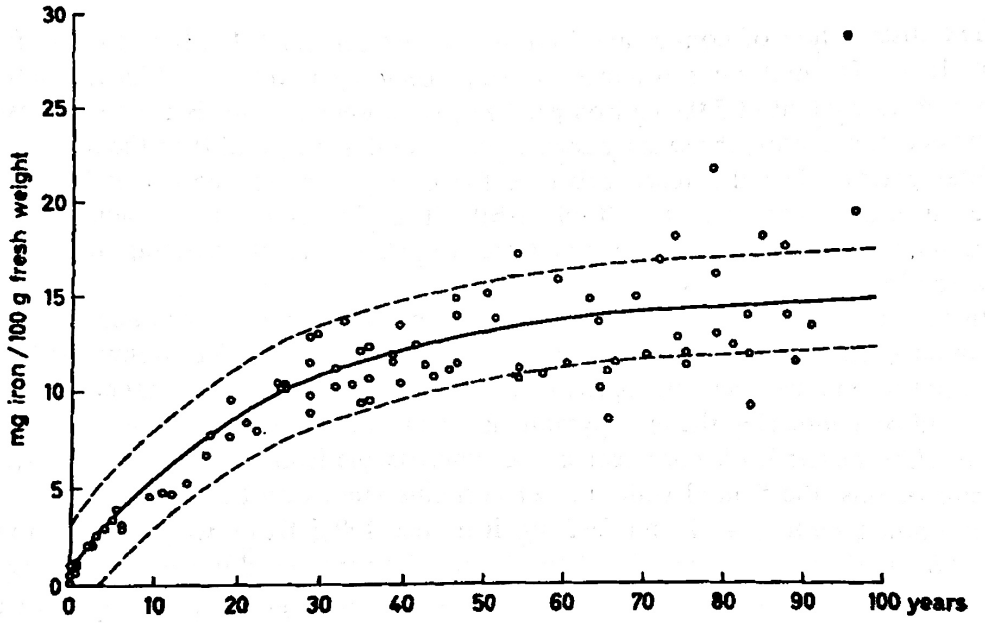

Figure 2.5: Non-haemin iron in the putamen. S.E. of estimate = ±2.60

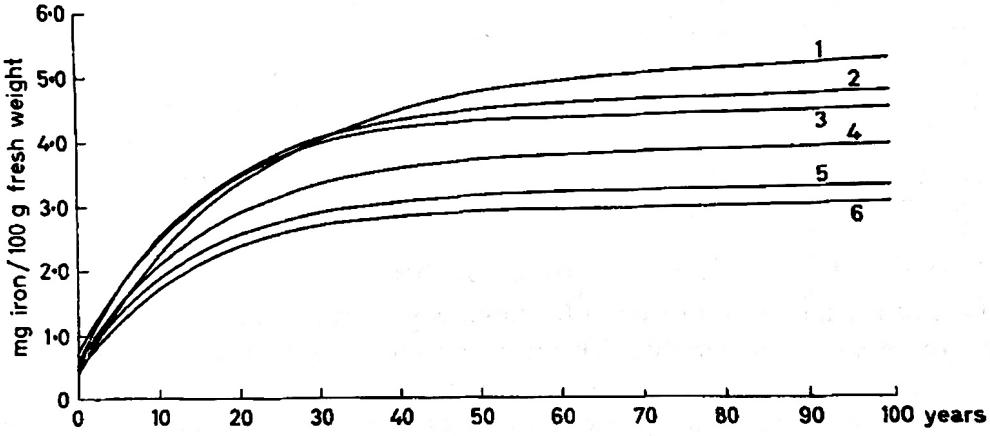

Figure 2.6: Relation between the non-haemin iron and the age in different cortical fields. (1) motor cortex; (2) occipital cortex; (3) sensory cortex; (4) parietal cortex; (5) temporal cortex; (6) prefrontal cortex.

iron redistribution within the brain. These factors can compromise the brain's iron homeostasis system, leading to iron accumulation that is not efficiently bound by storage proteins or other molecules [66, 67]. Excess iron accumulation can also result in oxidative stress, which damages cells and contributes to neurodegenerative processes [61].

Impact of Iron Levels on R_1 Relaxation Rate

Although the role of iron in enhancing proton relaxation has been extensively studied in ferritin model systems [68], its impact on longitudinal relaxation rate (R_1) in brain tissue is less well defined. Iron in the brain—predominantly stored as ferritin and hemosiderin—is paramagnetic and capable of influencing R_1, but the extent and consistency of this effect remain unclear, as reported findings are often contradictory. Some studies have reported significant correlations between iron concentration and R_1, particularly in regions with high iron content [22, 13, 1, 17]. Conversely, other investigations have failed to detect such associations [69, 70], underscoring the complexity of the underlying mechanisms and the need for further research.

Vymazal et al. [22] conducted a post-mortem MRI study using unfixed brain tissue from the frontal cortex, caudate nucleus, putamen, and globus pallidus. They found that differences in R_1 across these regions correlated well with iron content, in agreement with previous in vivo findings [14]. However, the correlation was primarily evident across regions, while intra-regional variability showed weak or nonsignificant associations, suggesting the presence of additional factors influencing R_1.

In an in vivo study, *Ogg et al.* [13] investigated age-related changes in R_1, further supporting the role of iron in modulating relaxation properties. Using an age-based regression model to estimate iron concentration [54], they examined the relationship between R_1 and estimated iron levels in the cortex, putamen, caudate, and frontal white matter.

A significant linear correlation between R_1 and iron concentration was observed across brain regions, with relaxivity and coefficient of determination

varying notably: 5.5 s^{-1}/mg/kg in the cortex ($R^2 = 0.53$), 6.1 s^{-1}/mg/kg in the frontal white matter ($R^2 = 0.19$), 1.7 s^{-1}/mg/kg in the putamen ($R^2 = 0.48$), and 1.0 s^{-1}/mg/kg in the caudate nucleus ($R^2 = 0.45$). These findings indicate that while relaxivity is highest in cortical and white matter regions, the strength of the association with iron concentration is greater in cortex and putamen, suggesting region-specific variability in how iron modulates longitudinal relaxation. These findings highlight the complex and multifactorial nature of the Fe–R_1 relationship, suggesting that the effect of iron on longitudinal relaxation depends not only on total iron concentration, but also on factors such as the molecular form of iron, its binding state, and the surrounding tissue microenvironment. In particular, myelin appears to play a crucial modulatory role. As a highly diamagnetic substance, myelin can partially counteract the paramagnetic effects of ferritin-bound iron on local magnetic susceptibility, especially in white matter [71, 72, 73, 74]. This diamagnetic shielding reduces the influence of iron on surrounding water protons, thereby attenuating its effect on relaxation rates. Post-mortem studies using quantitative susceptibility mapping (QSM) have confirmed this phenomenon, reporting weaker correlations between iron content and magnetic susceptibility in white matter compared to gray matter [53]. In addition to influencing susceptibility, the myelin-rich environment of white matter may also limit water mobility and alter spin–lattice interactions, further modulating the contribution of iron to R_1.

Moreover, the influence of iron on qMRI parameters may be temperature-dependent, in accordance with the Curie's Law for paramagnetic materials. Since paramagnetism arises from unpaired electrons, the magnetic susceptibility (χ) of iron-containing compounds is inversely proportional to temperature:

$$\chi = \frac{C}{T} \tag{2.17}$$

where C is the Curie constant and T is the absolute temperature. At very high magnetic fields, however, the magnetization reaches saturation and influence of temperature on the magnetic properties of iron becomes negligible.

Since molecular motion plays a crucial role in relaxation processes, temperature variations can alter the efficiency of water-proton interactions with paramagnetic iron. A decrease in χ at higher temperatures may reduce the local field fluctuations induced by iron, thereby influencing relaxation dynamics [75, 15]. Specifically, reduced temperatures slow down molecular motion, increasing the efficiency of proton–iron interactions and thereby shortening T_1. This phenomenon is particularly relevant in post-mortem imaging, where uncontrolled temperature fluctuations may introduce variability in R_1 measurements [41].

Chapter 3

Materials and Methods

3.1 Subject characteristics

Thirteen post-mortem human subjects were included in this study. The age of the individuals ranged from 48 to 81 years (mean age = 65.9 ±10.2 years). For each case, the post-mortem interval (PMI), defined as the time between death and the beginning of MRI acquisition, was known and directly recorded by forensic personnel. Therefore, no estimation methods (e.g., Henssge's nomogram [76]) were required. However, for one subject, PMI was not recorded.

Due to variability in the duration of cooling and the time spent at room temperature during forensic procedures, core body values differed among subjects (range = 4.6–23.7°C). After the forensic examination, all subjects were transported to the MRI facility. At least one hour passed between temperature measurement and scan onset, during which passive warming occurred. Consequently, the recorded values likely underestimate the actual brain temperature at scan onset, which was probably closer to ambient. In the same subject for whom PMI was unavailable, no thermal data were collected. This subject was therefore excluded from temperature-related analyses but retained for all other evaluations, including those investigating the association between iron concentration and longitudinal relaxation rate (R_1).

The inclusion criteria for subject selection were:

- PMI $<$ 72 hours;
- Absence of diagnosed neurological or neurodegenerative disorders;
- Absence of visible brain trauma;
- No ferromagnetic implants or MRI contraindications.

Ethical approval for this study was obtained from the local institutional review board, and informed consent for autopsy and research use of tissue was secured from the next of kin.

3.2 MRI Acquisition

MRI data were acquired using a 3T whole-body scanner (Magnetom TimTrio, Siemens Healthcare, Erlangen, Germany) equipped with a 12-channel head coil array.

For each subject, longitudinal relaxation time (T_1) was estimated at two time points:

- At the beginning of the scan session ($T_{1,\text{start}}$),
- At the end of the scan session ($T_{1,\text{end}}$).

Both measurements were acquired using a 3D Inversion Recovery (IR) Turbo Spin Echo (TSE) sequence optimized for post-mortem imaging. Multiple inversion times (TIs) were sampled to enable voxel-wise estimation of T_1 via curve fitting. Main acquisition parameters included:

- Repetition Time (TR): 8000 ms (8290 ms for TI = 3000 ms);
- Echo Time (TE): 8.5 ms;
- Inversion Times (TI): 100, 200, 400, 800, 1200, 2000, 3000 ms;
- Voxel size: $1 \times 1 \times 4$ mm^3;
- Field of View (FOV): 256×256 mm^2;
- Parallel imaging: GRAPPA (factor = 2);
- Bandwidth: 349 Hz/Px;
- Flip angle: 180°;
- Number of slices: 22 contiguous slices (4.0 mm thickness);
- Orientation: Axial (transverse plane).

Each T_1 dataset thus consisted of seven IR-TSE images with varying inversion times, both at the start and at the end of the scan session. This

multi-TI acquisition scheme enabled robust estimation of the T_1 relaxation time across different brain regions and provided a means to investigate intra-scan temperature-related changes in tissue relaxation dynamics. Additional MRI sequences (e.g., T_2 mapping, T_2^* mapping, and DTI) were acquired between the two T_1 mapping datasets as part of a broader post-mortem protocol. These acquisitions contributed to scan duration and potential intra-scan temperature changes, but were not included in the present analysis.

3.3 Tissue Preparation and Iron Quantification

Following MRI acquisition, autopsy was performed within 12 hours. Brains were extracted with ligation of the main supplying blood vessels to minimize blood washout and avoid the formation of air bubbles. Extracted brains were immersion-fixed in 4% phosphate-buffered formaldehyde solution (pH 7.0 $\pm$ 0.5) for 3–5 weeks, with a formalin replacement after four days to ensure complete fixation.

Brains were sectioned axially into 10 mm thick slices, approximately matching the orientation of the MRI acquisition. Although additional ROIs were generated during MRI processing, tissue specimens for ICP-MS analysis were dissected only from the following predefined brain regions, selected based on anatomical landmarks and MRI visibility:

- Gray matter: globus pallidus, putamen, caudate nucleus, frontal cortex, temporal cortex, occipital cortex;
- White matter: frontal, temporal, and occipital white matter.

To increase statistical robustness, cortex and other gray matter samples were divided into two subunits (anterior and posterior), and white matter samples into three (anterior, central, and posterior). The globus pallidus was not subdivided due to its small volume. Sample volumes were approximately $10\times10\times10\text{mm}^3$, adjusted based on anatomical constraints. All dissections were performed using ceramic knives to prevent metal contamination.

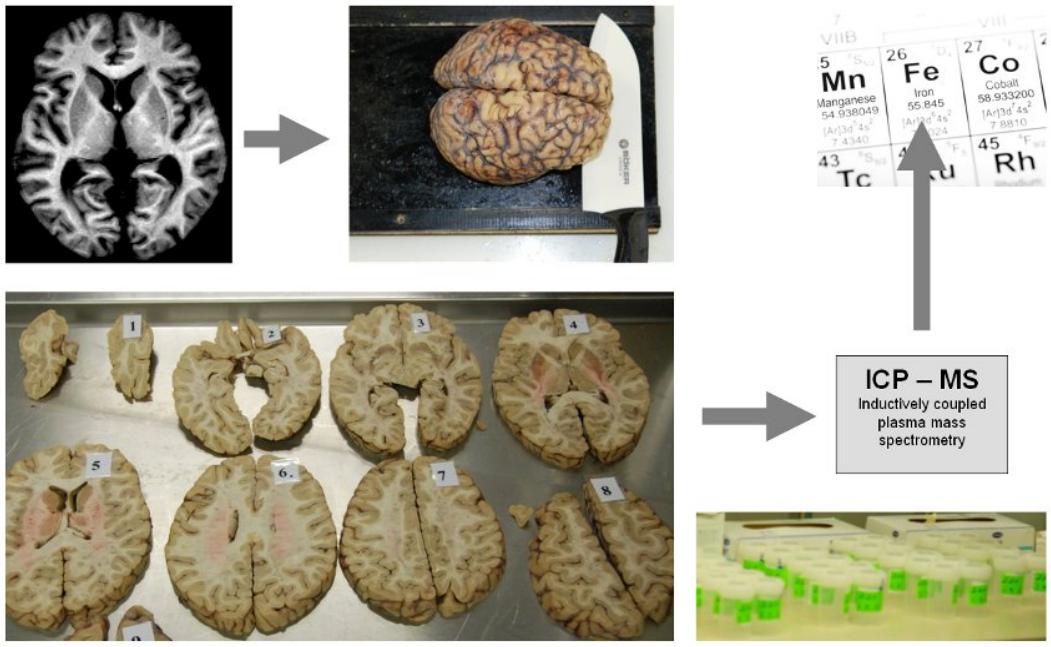

Figure 3.1: Workflow schematic of post-mortem tissue analysis: in situ T_1-weighted MRI, brain slicing, and ICP-MS iron quantification

Prior to chemical analysis, samples were freeze-dried and weighed before and after lyophilization to enable the calculation of iron concentration relative to fresh tissue weight. Mineralization was performed at 250°C for 30 minutes in an UltraCLAVE III microwave-heated autoclave (EMLS, Leutkirch, Germany). Iron content was measured using inductively coupled plasma mass spectrometry (ICP-MS, Agilent 7500ce, Santa Clara, CA, USA) at a mass-to-charge ratio of 56, in Helium collision mode (He flow rate = 5.3mL/min) to reduce polyatomic interferences. Measurement accuracy was validated against the certified NIST RM 8414 bovine muscle reference standard. Iron concentrations are reported in mg/kg of fresh tissue.

A schematic overview of the processing pipeline (from MRI acquisition to ICP-MS) is shown in Fig. 3.1.

3.4 T_1 Mapping

Quantitative T_1 maps were generated separately for the beginning ($T_{1,\text{start}}$) and end ($T_{1,\text{end}}$) of each MRI session. For each time point, seven inversion recovery (IR) datasets were acquired at different inversion times (TI = 100, 200, 400,

800, 1200, 2000, 3000 ms) using the 3D IR-TSE sequence. This protocol allowed sampling of the recovery curve of the longitudinal magnetization after inversion.

Voxel-wise T_1 estimation was performed by fitting the signal intensities $S(TI)$ across the seven inversion times to a three-parameter inversion recovery model:

$$S(TI) = M_0 \left(1 - 2\alpha \exp\left(-\frac{TI}{T_1}\right)\right) \tag{3.1}$$

where:

- M_0 is the equilibrium magnetization,
- T_1 is the longitudinal relaxation time,
- α is an inversion efficiency factor that accounts for deviations from the ideal 180° inversion. It captures imperfections due to inaccurate flip angles, B_1 inhomogeneities, and non-ideal RF pulse profiles.

All fittings were implemented in MATLAB (MathWorks, Natick, MA, USA) using custom-developed scripts.

Figure 3.2 further illustrates the anatomical correspondence by showing a central brain slice from the IR-weighted image alongside its respective T_1 map.

To visualize the IR dataset and generate parametric maps (T_1, M_0, α, R_1), a separate Python script was developed in Google Colab. The script combined the inversion time images into a 4D dataset, performed voxel-wise fitting, and exported the resulting parameter maps. The inversion factor map provides a voxel-level estimate of inversion pulse efficiency.

Figure 3.3 shows the signal evolution at each inversion time for the central slice of a representative subject, illustrating the contrast variation across the IR dataset.

Example data and model fits from three manually selected voxels—representative of white matter, cortex, and basal ganglia—are shown in Fig. 3.4. These voxels were identified from the central axial slice, and their inversion

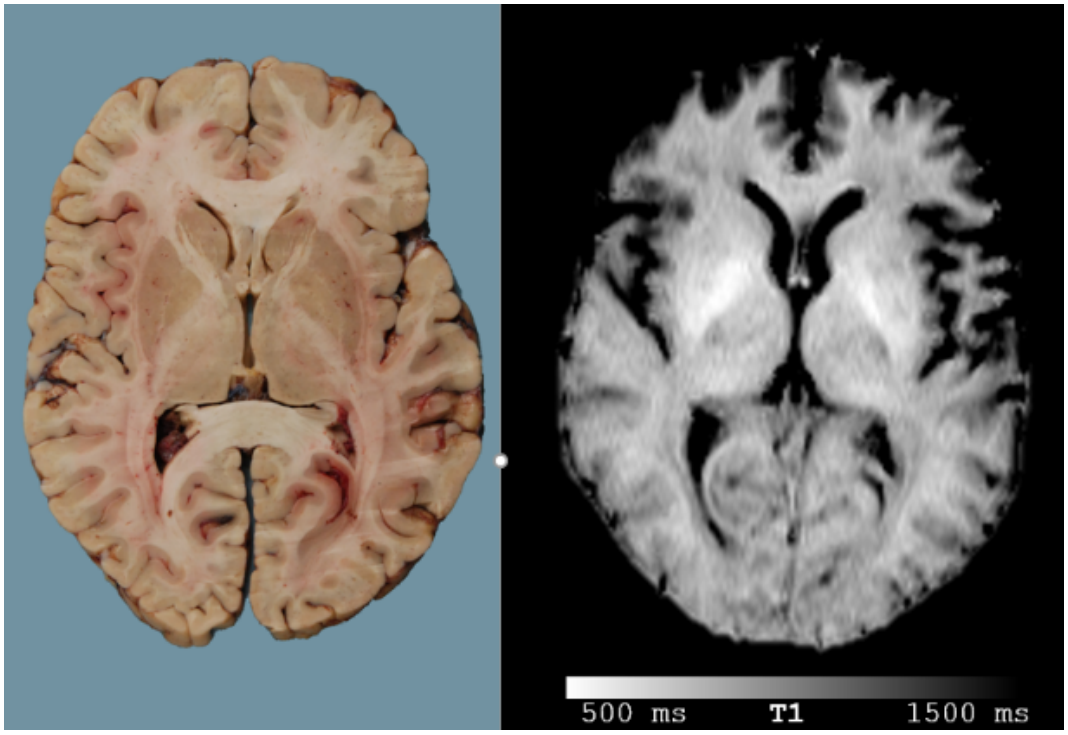

Figure 3.2: Left: anatomical reference slice from an image; Right: corresponding quantitative T_1-weighted image. This comparison highlights the spatial alignment between structural features and relaxation-based tissue contrast.

recovery curves illustrate the typical signal evolution and fitting quality across distinct tissue types.

Figure 3.5 displays the resulting parametric maps derived from the three-parameter model, including T_1, M_0, α, and R_1, for the central axial slice of a representative subject.

3.5 ROI Definition and Extraction

Regions of interest (ROIs) were manually delineated on anatomical images selected for high tissue contrast, with the aim of extracting T_1 values from the same brain regions sampled for ICP-MS quantification. Manual segmentation was performed of the following brain regions were included:

- Gray matter: globus pallidus, putamen, caudate nucleus, thalamus, frontal cortex, temporal cortex, occipital cortex;
- White matter: frontal, temporal, and occipital white matter.

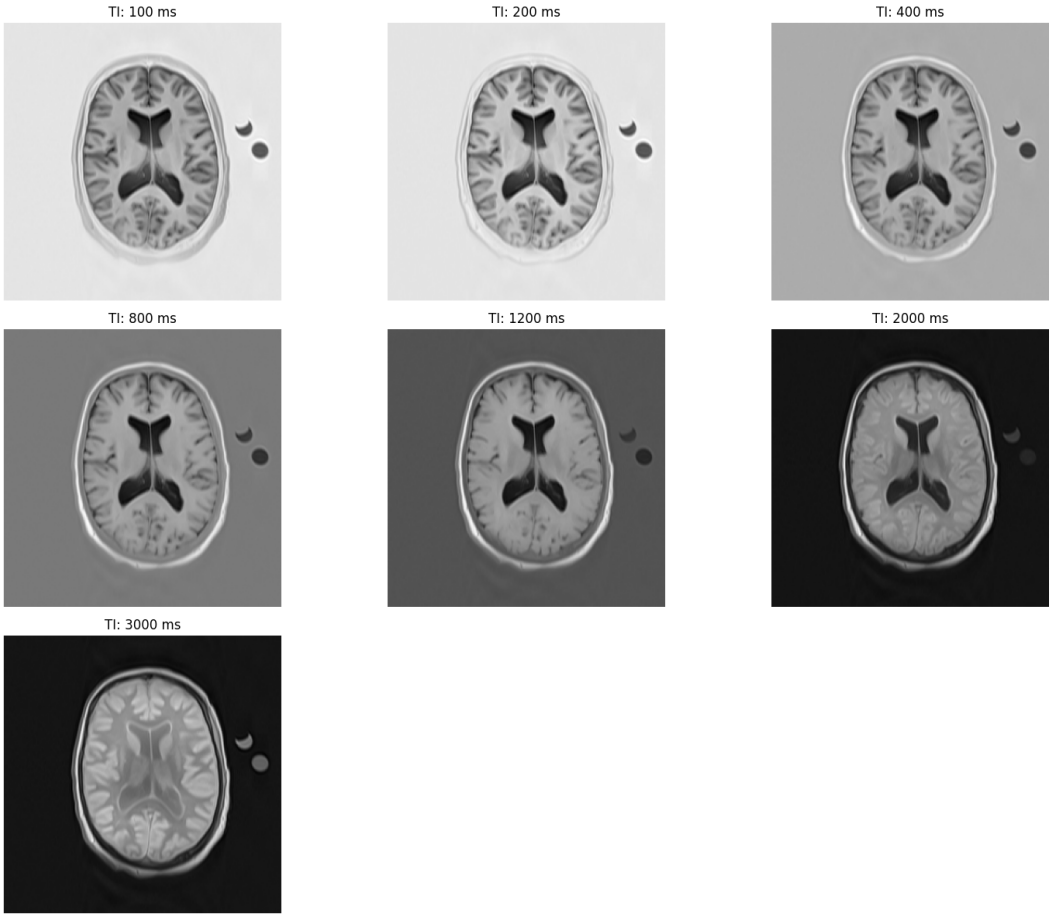

Figure 3.3: Turbo-spin-echo (TSE) images acquired at different inversion times (TI = 100–3000 ms) for the central axial slice of a 56-year-old subject. The contrast variation across TIs enables voxel-wise estimation of longitudinal relaxation times.

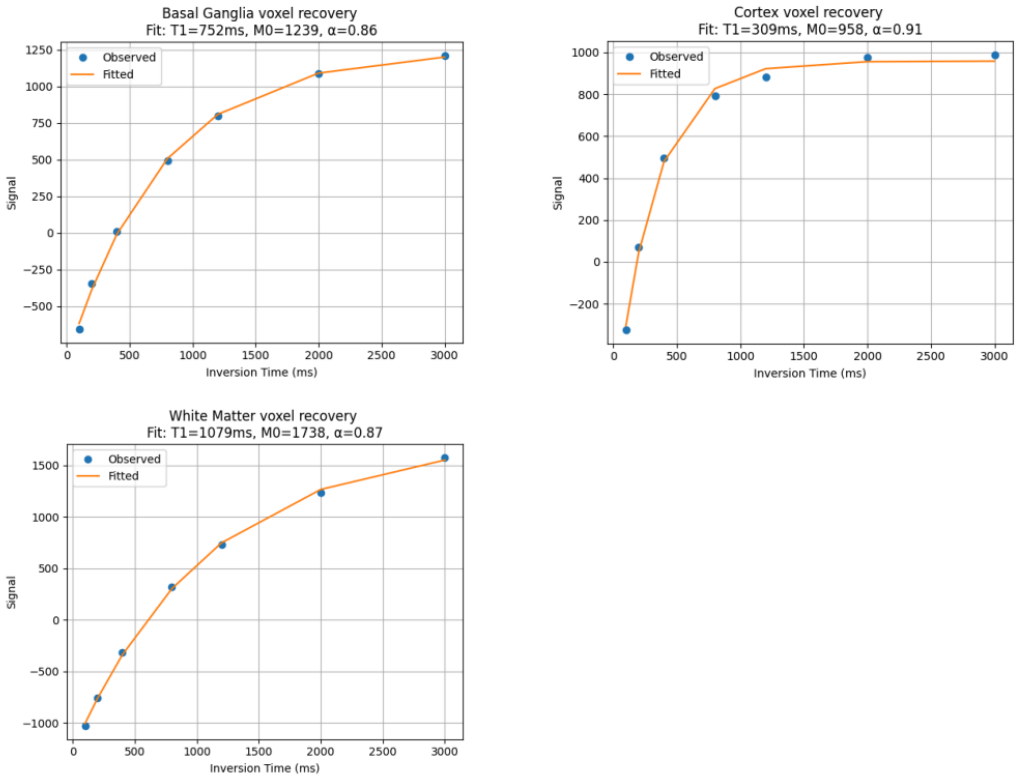

Figure 3.4: Longitudinal recovery curves from representative voxels in white matter, cortex, and basal ganglia for the same subject. Observed signal intensities (dots) at different inversion times (TI) are shown alongside the fitted 3-parameter inversion recovery model (solid lines). Voxel coordinates were manually selected from the central axial slice.

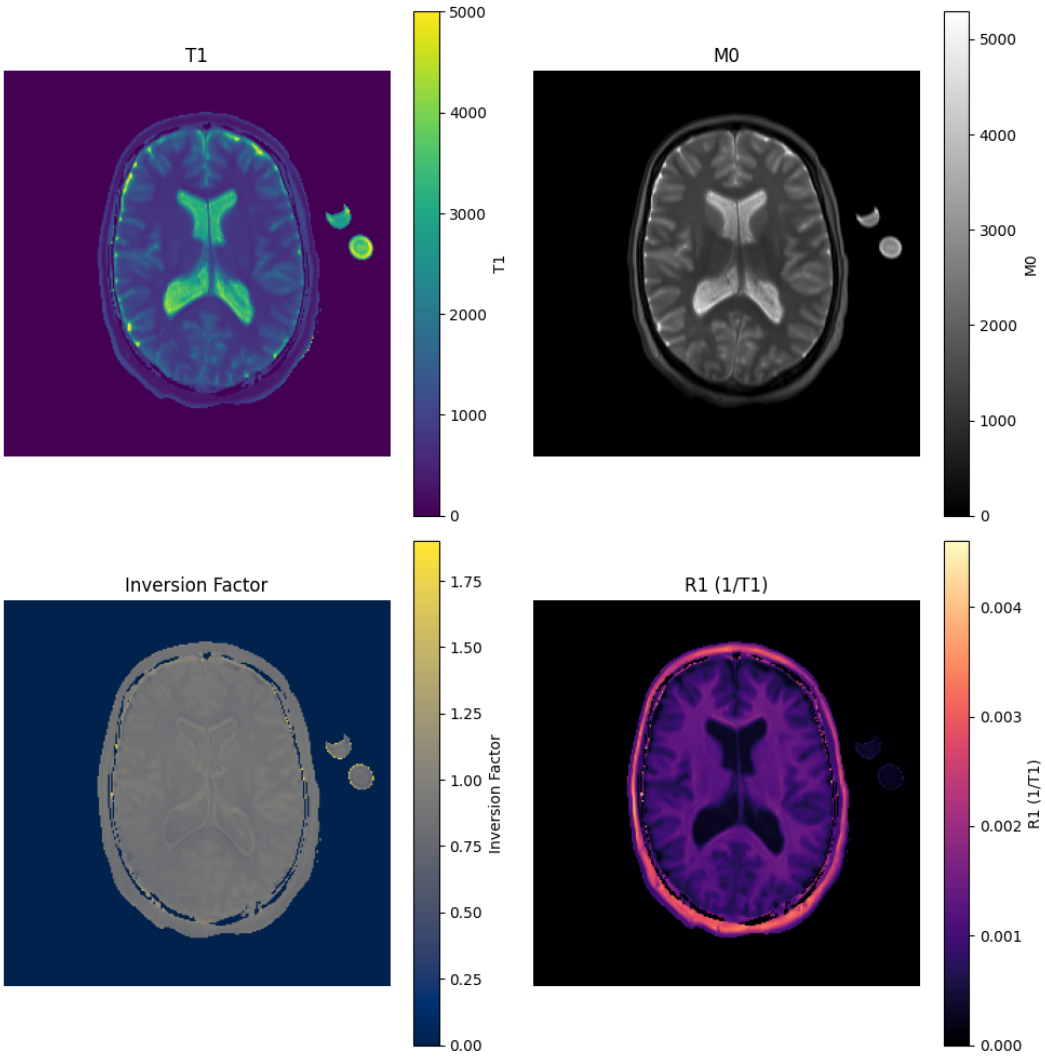

Figure 3.5: Parametric maps derived from the three-parameter IR model for the central slice of the same subject. Top row: T_1 and M_0 maps; bottom row: α and R_1 maps.

ROI placement was guided by anatomical landmarks to ensure correspondence with the anatomical location of the tissue specimens used for chemical analysis. Regions were delineated bilaterally when applicable, and ROI mask sizes were manually adjusted to approximate the physical volume of the dissected samples (~$10 \times 10 \times 10$ mm^3).

To align the segmented ROIs with the T_1 maps, affine registration was performed using FSL tools [77]. ROI masks were then applied voxel-wise to the T_1 parametric maps to extract mean regional values for subsequent statistical analysis. This procedure ensured spatial correspondence between the MRI-derived relaxation metrics and the iron concentrations obtained via ICP-MS.

For each subject, quantitative measurements (T_1 and iron concentration) were extracted from the following anatomical subregions:

- Basal ganglia: globus pallidus, putamen, and caudate nucleus;
- White matter: frontal, temporal, and occipital white matter;
- Cortex: frontal, temporal, and occipital cortex.

Due to the progressive extension of the sampling protocol, cortical ROIs were available only for the last eight subjects. Consequently, analyses involving cortical measurements were limited to this subset, while all thirteen subjects were included in analyses of the basal ganglia and white matter. This strategy maximized data usage but introduced a sample size imbalance across regions, which was considered in the interpretation of results. These subregions were grouped accordingly in subsequent analyses.

3.6 Data quality control

Before statistical analysis, specific data points were excluded based on completeness and plausibility criteria:

- Measurements with $T_{1,\text{end}} = 0$ were excluded, as they indicate failed

fitting or missing signal recovery. This affected occipital and frontal cortex measurements for one subject.

- Globus pallidus measurements from a subject were excluded due to extremely high and non-physiological iron values.

These exclusions were applied to ensure data reliability and biological plausibility, and they are transparently reported to maintain reproducibility of the analysis.

3.7 Statistical analysis

All statistical analyses were performed using R (version 4.4.2). Data processing and visualization were conducted using the following packages, grouped by function:

- Data import and manipulation: `readxl`, `dplyr`, `tidyr`, `tibble`
- Statistical analysis: `broom`, `car`, `PMCMRplus`, `FSA`, `nlme`
- Visualization: `ggplot2`, `ggpmisc`

Unless otherwise specified, results with $p < 0.05$ were considered statistically significant.

Overview of comparisons

The relationship between tissue parameters (T_1 and R_1) and either temperature or iron concentration was investigated using both descriptive and inferential statistical approaches. Analyses were performed at multiple levels:

- **Temperature effects** were assessed through two complementary strategies:
  - A cross-sectional analysis relating core temperature to $T_{1,\text{start}}$, using region-wise linear regression (naive pooled approach);

  - An intra-scan analysis comparing $T_{1,\text{start}}$ and $T_{1,\text{end}}$ using paired t-tests, as well as pooled, subject-specific level, and mixed-effects regression models.

- **Iron effects** were explored by comparing iron concentration across regions and by evaluating its association with R_1 through pooled, subject-level, and mixed-effects regression models.

Temperature analysis

Two complementary strategies were used to evaluate the effect of temperature on T_1 relaxation time:

1. **Effect of initial temperature on $\mathbf{T_{1,\,Start}}$**

   - Linear regression models were fitted between reported core temperature and $T_{1,\text{Start}}$ values, separately for each brain region (basal ganglia, white matter, and cortex). This modeling choice is theoretically supported by the Fast Exchange Two-State model, which predicts an approximately linear temperature dependence of T_1 over narrow temperature ranges [20]. A naive pooled approach was adopted, treating all regional samples as independent observations despite their clustering within subjects. This approach was adopted for descriptive purposes and to increase statistical power, although it may underestimate standard errors due to intra-subject dependencies.
   - Model assumptions were assessed using Shapiro-Wilk test and visual inspection of residuals.
   - Regression slopes were used to extrapolate T_1 values at 37°C, which were compared to reference values from the literature.

2. **Intra-scan T_1 changes ($T_{1,\textbf{end}}$ vs. $T_{1,\textbf{start}}$)**

   - Paired t-tests were used to compare mean T_1 values at the beginning and end of the scan for each tissue type.

- Linear regression models were fitted separately for each brain region using a naive pooled approach, in which all regional samples were treated as independent observations.
- Separate linear models were fitted for each subject and brain region to assess inter-subject variability in slope estimates.
- Welch's ANOVA was used to test for differences in the mean slopes across brain regions, followed by Games-Howell post-hoc comparisons.
- Linear mixed-effects models were used to account for intra-subject correlation:
  - An interaction model including $T_{1,\text{start}}$, brain region, and their interaction as fixed effects, with subject as a random intercept;
  - Region-specific mixed models were also fitted independently for basal ganglia, white matter, and cortex.
- Model assumptions (normality, homoscedasticity, independence) were assessed using the Shapiro–Wilk test and visual inspection of residual plots.
- Akaike Information Criterion (AIC) was used to compare the relative performance of simple linear models and mixed-effects models.

Iron analysis

The effect of iron concentration on the longitudinal relaxation rate (R_1) was evaluated through a structured multilevel approach:

1. **Descriptive comparison of iron concentration across brain regions**
   - Iron concentrations (mg/kg of fresh tissue) were summarized by computing the mean, median, and standard deviation for each of the three macroregions: basal ganglia, white matter, and cortex.

- Normality of the distributions was assessed using the Shapiro–Wilk test.
- Due to significant deviations from normality in all regions, inter-regional differences were tested using the Kruskal–Wallis test, followed by pairwise post-hoc comparisons using the Dunn test with Bonferroni correction.

2. **Linear modeling of R_1 as a function of iron concentration**

   - Region-wise linear regression models were fitted between R_1 and iron concentration. A naive pooled approach was adopted for descriptive purposes, treating all regional samples as independent despite their clustering within subjects.
   - Model assumptions were assessed using the Shapiro–Wilk test and visual inspection of residuals and QQ plots.
   - Separate subject-level linear models were also fitted within each brain region to examine inter-individual variability in regression parameters (slope, intercept, R^2).
   - Linear mixed-effects models were used to account for intra-subject correlation, including iron concentration as a fixed effect and subject as a random intercept. These models were fitted independently for basal ganglia, white matter, and cortex.
   - Akaike Information Criterion (AIC) was used to compare the relative performance of fixed versus mixed-effects models.

3. **Subregional analysis of the basal ganglia**

   - Iron concentration was analyzed separately in the globus pallidus, putamen, and caudate nucleus. Descriptive statistics and normality tests were computed for each subregion individually.
   - The Kruskal–Wallis test was used to evaluate iron concentration differences across subregions, followed by Dunn's pairwise comparisons with Bonferroni correction.

- Separate linear regression models were fitted between R_1 and iron concentration within each subregion to evaluate local effects.
- Model assumptions were assessed through residual normality testing and visual inspection of residual plots. Due to repeated measures within subjects, results were interpreted cautiously with respect to the independence assumption.

The results of the analyses described above are presented and discussed in the following chapters.

Chapter 4

Results

This chapter presents the results of the quantitative MRI analyses performed on post-mortem human brain tissue, with the aim of investigating how longitudinal relaxation is influenced by temperature and iron concentration. Particular attention is given to regional differences across white matter, cortex, and basal ganglia, as well as to methodological challenges specific to post-mortem imaging, such as the uncertainty in temperature measurements and potential violations of independence assumptions.

The first part of the chapter focuses on the relationship between T_1 and brain temperature measured prior to the MRI scan. Linear regression models are fitted separately for white matter, cortex, and basal ganglia, and results are compared to those from prior post-mortem studies. Extrapolated T_1 values at 37°C are also compared with *in vivo* reference values from the literature.

Given the limitations of core temperature as a proxy for brain temperature at scan onset, a second analysis investigates intra-scan changes in T_1 between the beginning and end of the acquisition session. This part assesses a progressive warming of the tissue due to RF-induced heating and environmental equilibration. Paired t-tests, pooled and region-specific linear regressions, subject-level models, and mixed-effects models are employed to explore the dynamics of T_1 variation and their tissue-specific patterns.

Finally, the last section addresses the effect of iron concentration on R_1, under the assumption that all brains reached a relatively uniform final temperature by the end of the scan. The analysis is structured in two steps: first, linear. subject-level and mixed-effects models are applied across major tissue types (basal ganglia, white matter, cortex) to assess the overall association between iron and R_1 ; second, a more detailed analysis is conducted within basal ganglia subregions (putamen, caudate nucleus, globus pallidus) to investigate whether the global association observed in the basal ganglia is driven by true within-region effects or merely reflects regional clustering of iron levels.

	Intercept (ms)	Slope (ms/°C)	R^2	p-value	SE Slope (%)
Basal Ganglia	711 ± 30	3.6 ± 2.0	0.10	**<0.01***	28
White Matter	837 ± 21	–1.4 ± 1.4	0.02	0.06	53
Cortex	710 ± 98	15.5 ± 5.7	0.30	**<0.01***	18

Table 4.1: Summary of linear regression models assessing the relationship between temperature and T_1 across brain regions. Reported values include intercept and slope (in ms), coefficient of determination (R^2), p-value, and relative standard error of the slope (SE, %).

Together, these analyses contribute to clarifying how temperature and iron concentration influence relaxation properties in unfixed post-mortem brain tissue, offering useful context for interpreting quantitative MRI findings in *ex vivo* conditions.

4.1 Initial T_1 vs. Temperature

Region-specific linear regression models

Linear regression analyses were performed to investigate the relationship between brain temperature and T_1 relaxation times across different brain regions. Figures 4.1, 4.2, and 4.3 illustrate the temperature-dependent variations in T_1 for the basal ganglia, white matter and cortex, respectively, with linear fits overlaid. Table 4.1 reports the main parameters of the regression models, including slope, intercept, R^2, p-values, and the standard error of the slope expressed as a percentage. The estimated temperature coefficients were 15.5 ms/°C for the cortex, 3.6 ms/°C for the basal ganglia, and –1.4 ms/°C for the white matter. The models for cortex and basal ganglia yielded statistically significant results ($p < 0.01$), while the model for white matter did not reach significance ($p = 0.06$). The corresponding R^2 values were 0.30, 0.10, and 0.02 for cortex, basal ganglia, and white matter, respectively.

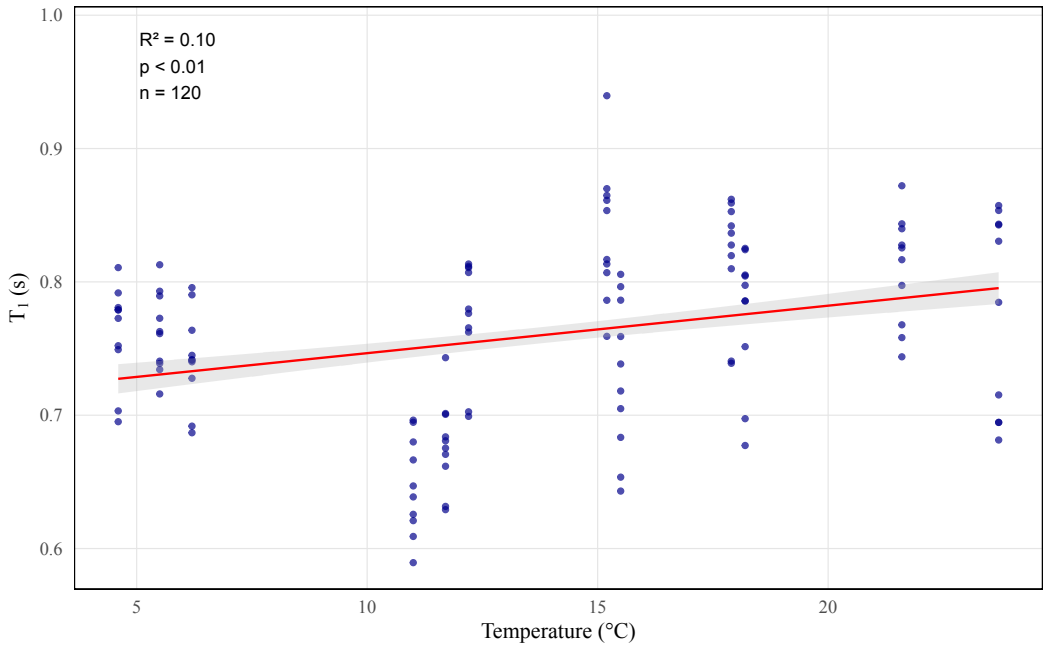

Figure 4.1: Linear regression of T_1 relaxation time as a function of temperature across basal ganglia samples. The red line represents the linear fitted model; the shaded gray area indicates the ± 1 standard error (SE) interval.

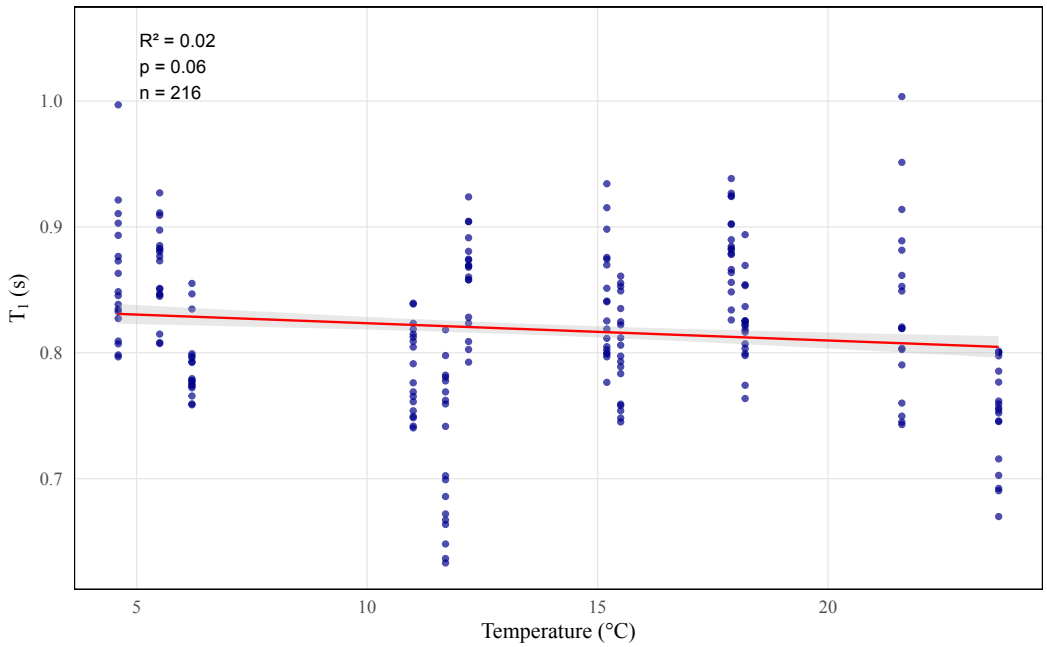

Figure 4.2: Linear regression of T_1 relaxation time as a function of temperature across white matter samples. The red line represents the linear fitted model; the shaded gray area indicates the ± 1 standard error (SE) interval.

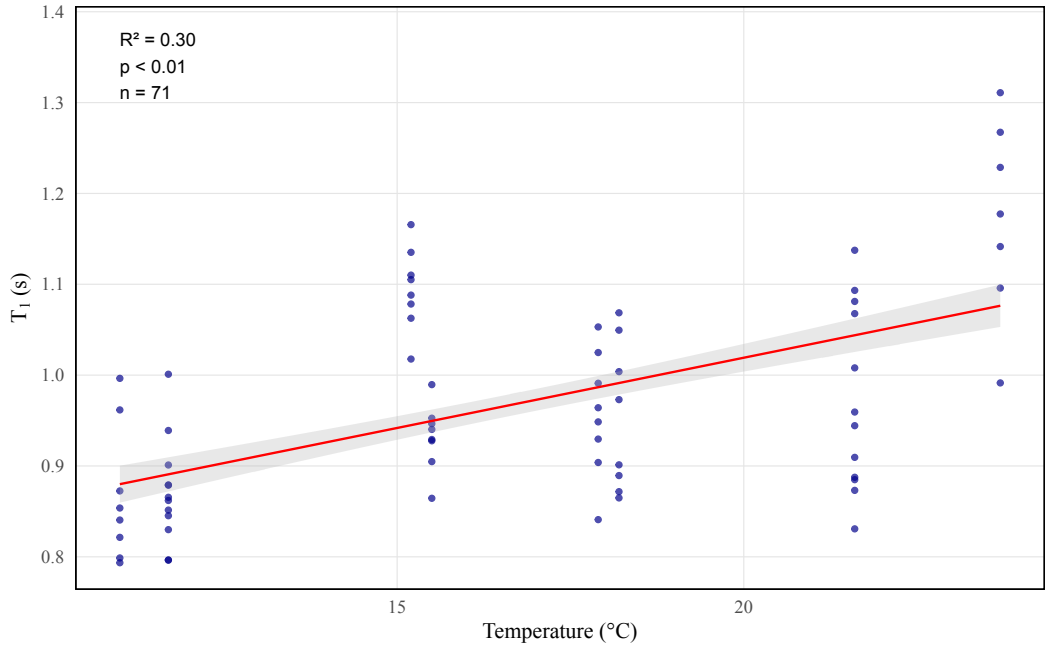

Figure 4.3: Linear regression of T_1 relaxation time as a function of temperature across cortical gray matter samples. The red line represents the linear fitted model; the shaded gray area indicates the ±1 standard error (SE) interval.

	This study (ms/°C)	**Literature (ms/°C)**	**Reference**
Basal Ganglia	3.6 ± 2.0	13 ± 1	[9]
White Matter	–1.4 ± 1.4	3 ± 1	[9]
Cortex	15.5 ± 5.7	17 ± 5	[9]

Table 4.2: Comparison of temperature coefficients (T_1 change per °C) between this study and values reported by *Birkl et al.* [9].

Comparison with literature and extrapolated values

Table 4.2 compares the temperature coefficients from this study with values reported by *Birkl et al.* [9], who performed controlled heating experiments on unfixed post-mortem brain slices. The coefficients observed here are lower overall, particularly in the white matter.

To further contextualize the results, Table 4.3 presents T_1 values extrapolated to 37°C for each brain region, alongside *in vivo* reference values from the literature and corresponding percentage differences. While the regression mod-

	This Study (ms)	In Vivo (ms)	Reference	Difference (%)
Basal Ganglia	843 ± 48	1363 ± 58	[26]	–38.2
White Matter	786 ± 35	838 ± 50	[25]	–6.2
Cortex	1282 ± 117	1607 ± 112	[26]	–20.2

Table 4.3: Comparison of T_1 values extrapolated to 37°C in this study with in vivo literature values, including the percentage difference between the two.

els confirm region-specific temperature dependencies, the extrapolated values were consistently lower than *in vivo* measurements. The largest discrepancy was observed in the basal ganglia (∼38%), followed by the cortex (∼20%), while white matter showed a smaller difference (∼6%).

Residual analysis and model interpretation

The normality of residuals was assessed using the Shapiro–Wilk test. No significant deviations from normality were detected for white matter ($p = 0.13$) and cortex ($p = 0.43$), whereas residuals from the basal ganglia model did not meet the normality assumption ($p < 0.01$). However, visual inspection of residual plots and Q–Q plots did not indicate substantial deviations from normality, as shown in Figure 4.4.

Although the linear models appear adequate based on residual diagnostics, it is important to acknowledge the potential lack of independence among data points, as multiple measurements per subject were included. Consequently, these regression analyses should be interpreted as descriptive and exploratory rather than inferential.

Notably, although the extrapolated T_1 value for white matter was numerically closest to literature values, it was derived from a regression model with a negative and non-significant slope. This suggests that the white matter result may not reliably reflect a physiological relationship between temperature and longitudinal relaxation, and should be interpreted with caution.

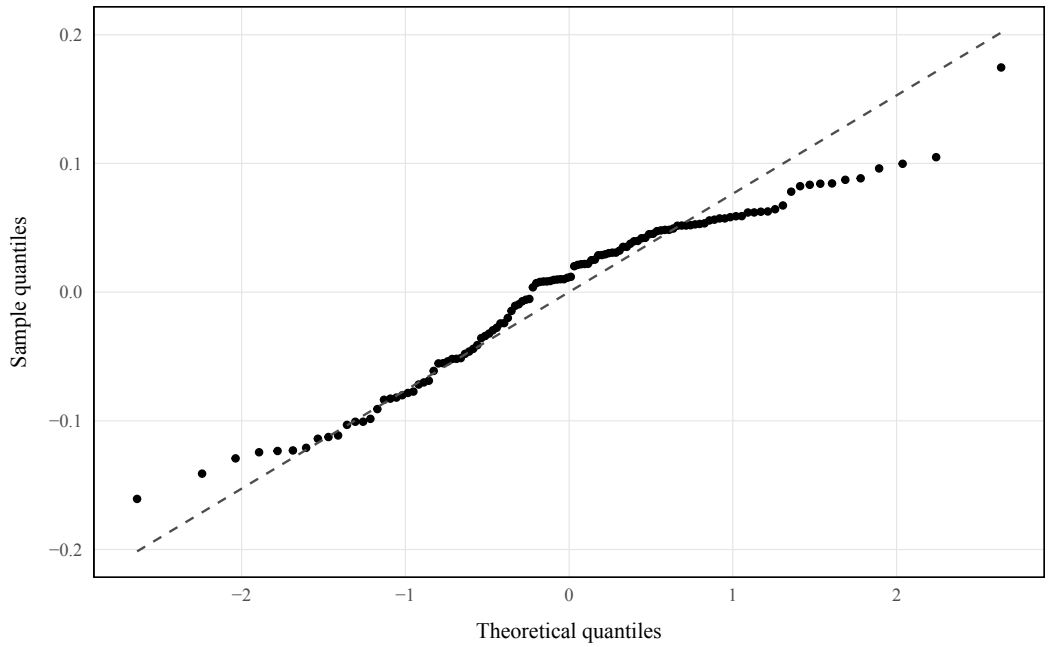

Figure 4.4: Q–Q plot of residuals from the linear regression model between T_1 values and temperature for basal ganglia. Despite the Shapiro–Wilk test indicating non-normality, visual inspection reveals only minor deviations from the expected normal distribution.

Finally, potential discrepancies between extrapolated and in vivo values may stem from multiple sources: (i) the temperature measurements were taken at the core body, not directly from the brain, and may not accurately reflect actual brain temperature; (ii) temperature was recorded up to several hours prior to scanning, during which passive warming likely occurred, making brain temperature at scan onset closer to room temperature in most cases; and (iii) the assumption of independence may be violated due to repeated measures within subjects.

To further investigate temperature-related variation in T_1, the next section explores changes in T_1 between the beginning and end of the scan session. This analysis assumes a progressive tissue warming over time, driven by RF-induced heating and passive equilibration toward room temperature.

	$\mathbf{T_{1,\,Start}}$ **(ms)**	$\mathbf{T_{1,\,End}}$ **(ms)**
Basal Ganglia	755 ± 71	796 ± 82
White Matter	816 ± 64	840 ± 71
Cortex	840 ± 119	1052 ± 144

Table 4.4: Mean longitudinal relaxation times (T_1) measured at the beginning and end of the scan session, reported as mean ± standard deviation for each brain region. The observed increases are consistent with a rise in temperature during scanning.

4.2 Temperature Effects on T_1 Variation

Paired comparison of T_1 values at scan start and end

To assess the intra-scan variation of longitudinal relaxation times in post-mortem brain tissue, mean T_1 values for the basal ganglia, white matter, and cortex were computed at both the beginning and end of the scan session. These values, expressed as mean ± standard deviation (SD), are reported in Table 4.4. To better illustrate the regional differences in intra-scan T_1 variation, Figure 4.5 shows the mean increase in T_1 ($\Delta T_1 = T_{1,\text{end}} - T_{1,\text{start}}$) across brain regions, together with standard deviation bars. The largest increase is observed in the cortex, followed by the basal ganglia and white matter. Normality of the paired differences was evaluated using the Shapiro–Wilk test, which indicated non-normality for white matter and cortex ($p < 0.05$). Nonetheless, histogram and Q–Q plot inspection did not suggest major deviations from normality (Figure 4.6). A paired t-test was therefore performed, revealing a significant increase in T_1 across all regions ($p < 0.01$). This finding is consistent with a temperature increase during the scan session, which is likely to affect relaxation times.

Region-specific linear regression models

A preliminary analysis was conducted to assess the correlation between T_1 values at the beginning and end of the scan across all brain regions combined. The Pearson correlation coefficient was $r = 0.96$ ($p < 0.01$), indicating a strong

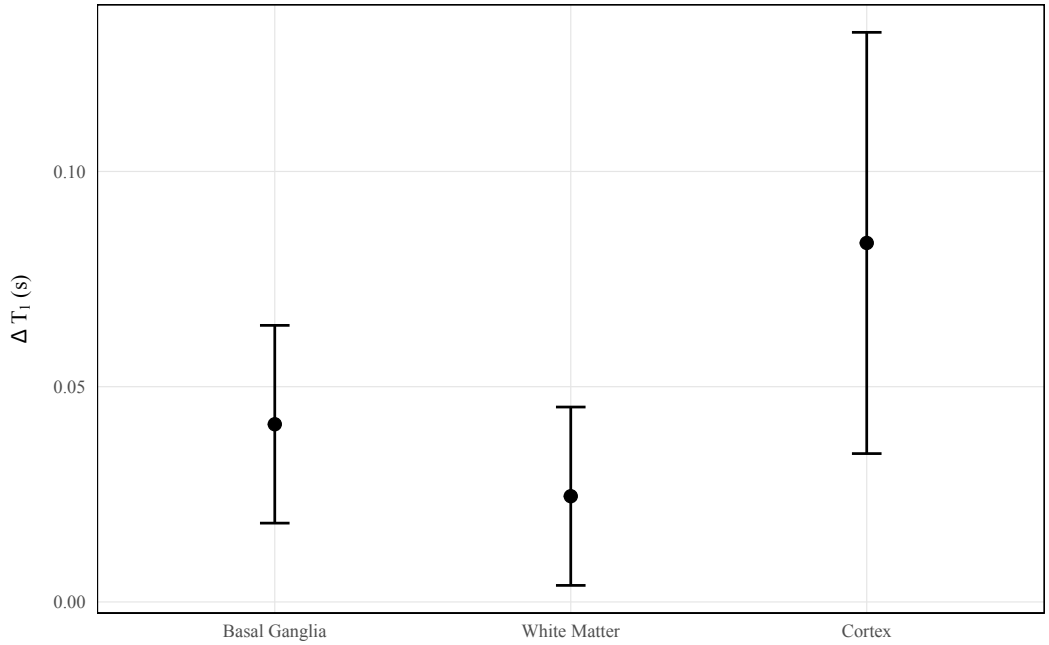

Figure 4.5: Mean intra-scan increase in longitudinal relaxation time ($\Delta T_1 = T_{1,\text{end}} - T_{1,\text{start}}$) across brain regions. Points represent the mean; vertical lines indicate ± 1 standard deviation.

linear relationship. Figure 4.7 illustrates the relationship between mean T_1 and ΔT_1, providing a complementary visualization of this intra-scan association.

To further investigate temperature-induced variation, linear regression models were fitted for each brain region to predict final T_1 from initial values. As expected under RF-induced or passive thermal equilibration, final T_1 values were consistently higher. Regression results are summarized in Table 4.5, and visualized in Figure 4.9. All models were statistically significant ($p < 0.01$), with $R^2 > 0.90$ in all regions, confirming strong predictive relationships.The assumption of residual normality was statistically supported for the cortex and basal ganglia models (Shapiro–Wilk $p > 0.05$), but not for white matter ($p < 0.01$). Nonetheless, visual inspection of the residual Q–Q plot for the white matter model (Figure 4.8) did not reveal major deviations from normality, suggesting that the residual distribution is approximately Gaussian, with only minor deviations in the tails. Residuals were homoscedastic and symmetrically distributed across all models.

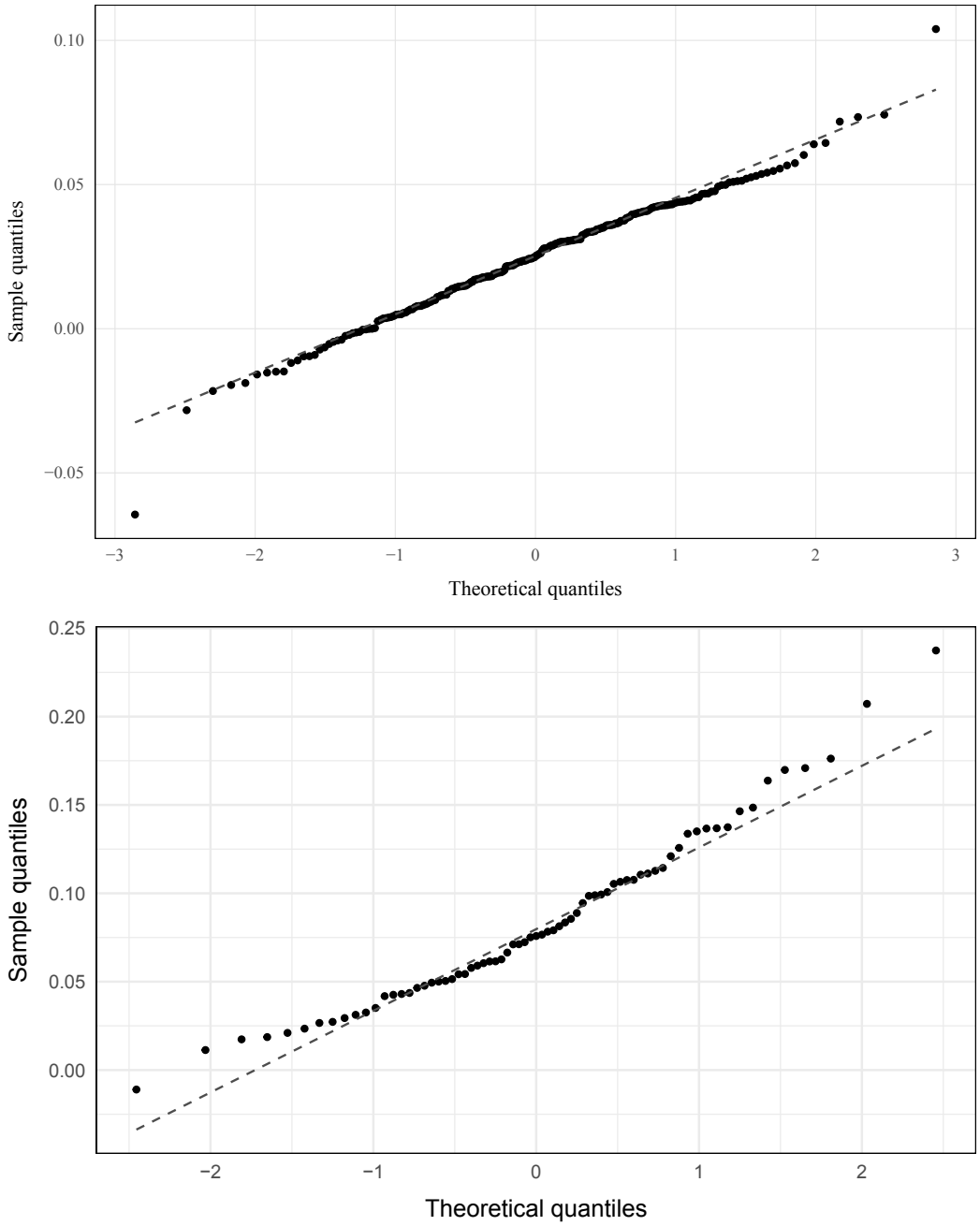

Figure 4.6: Q–Q plots of paired differences in T_1 values between the beginning and end of the scan session ($\Delta T_1 = T_{1,\text{end}} - T_{1,\text{start}}$), separately for white matter (top) and cortex (bottom). Despite statistical non-normality in Shapiro–Wilk tests ($p < 0.05$), visual inspection suggests only minor deviations from normality, mostly in the distribution tails.

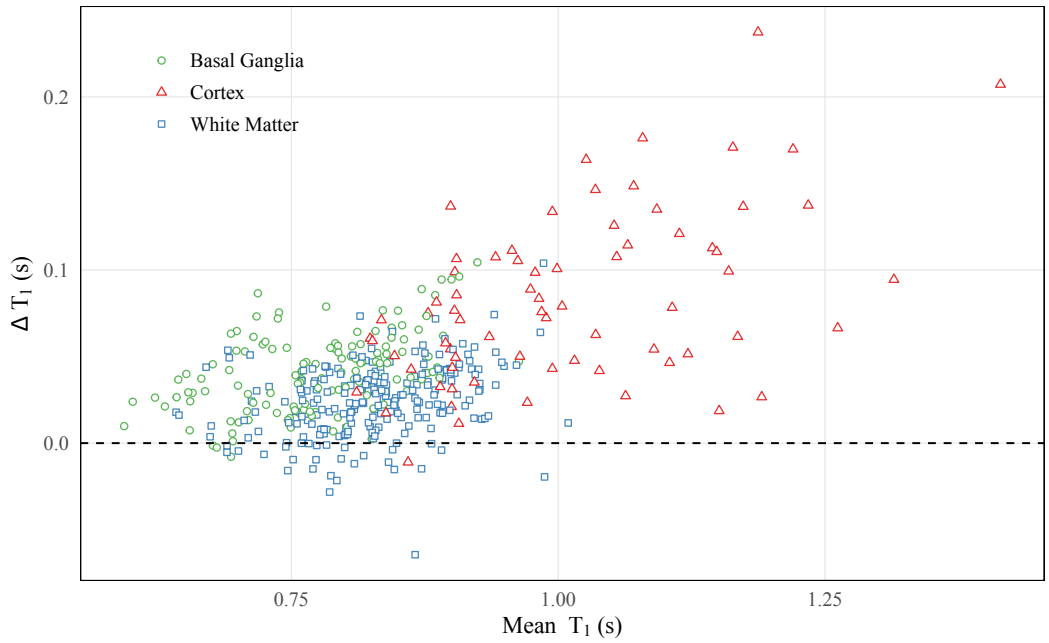

Figure 4.7: Relationship between mean T_1 values and intra-scan changes ($\Delta T_1 = T_{1,\text{end}} - T_{1,\text{start}}$) across all brain regions. Each point represents a tissue sample, color-coded and shaped by region: basal ganglia (red circles), white matter (blue squares), and cortex (green triangles). The dashed black line at $\Delta T_1 = 0$ indicates no change between start and end of scan. Samples above the line show an increase in T_1 during the scan session, consistent with progressive tissue warming.

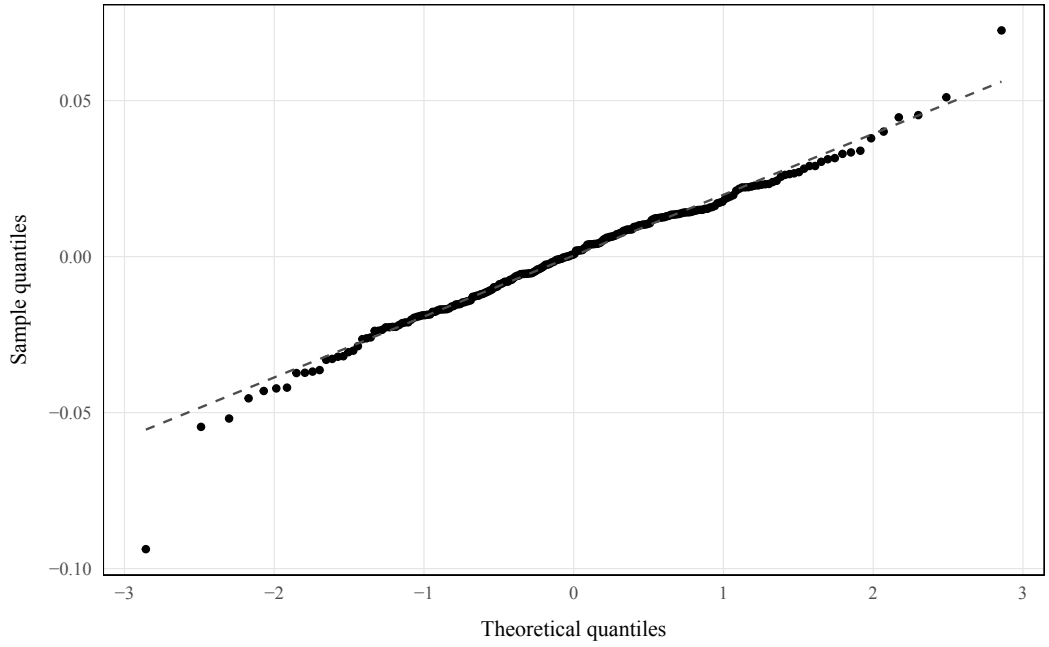

Figure 4.8: Q–Q plot of residuals for the white matter linear model. Although the Shapiro–Wilk test suggested non-normality, the visual inspection supports an approximately normal distribution.

	Intercept (s)	Slope	R^2	p-value	SE Slope (%)
Basal Ganglia	–0.05 ± 0.04	1.12 ± 0.05	0.93	**<0.01***	2.42
White Matter	–0.02 ± 0.03	0.92 ± 0.04	0.92	**<0.01***	1.97
Cortex	–0.05 ± 0.09	1.14 ± 0.09	0.90	**<0.01***	4.06

Table 4.5: Linear regression results modeling T_1 values at the end of the scan as a function of those at the beginning, reported separately for each brain region.

Notably, the slopes were highest in the cortex, followed by basal ganglia and white matter, suggesting regional differences in the effect of temperature. This trend is consistent with the previous pooled and region-specific analyses.

Subject-specific regression models

To assess individual-level trends, linear regressions were performed separately for each subject and region. In subjects with all three regions available, cortex typically showed the steepest slopes, while white matter had consistently lower values. Slopes across subjects are reported in Table 4.6. A summary of the subject-level regression parameters is shown in Table 4.7, and examples of individual fits are displayed in Figure 4.10. Figure 4.11 presents the regression lines for a representative subject, illustrating the fitted trends across all regions.

To statistically compare regional slopes, Welch's ANOVA was used due to a borderline violation of the homoscedasticity assumption (Levene's test: $p = 0.05$) and unequal sample sizes across regions, particularly the smaller number of cortical observations. A significant difference in slopes across regions was observed ($p < 0.01$). Post-hoc Games–Howell tests revealed that white matter slopes were significantly lower than those in basal ganglia ($p < 0.01$) and cortex ($p < 0.01$), while no significant difference was found between basal ganglia and

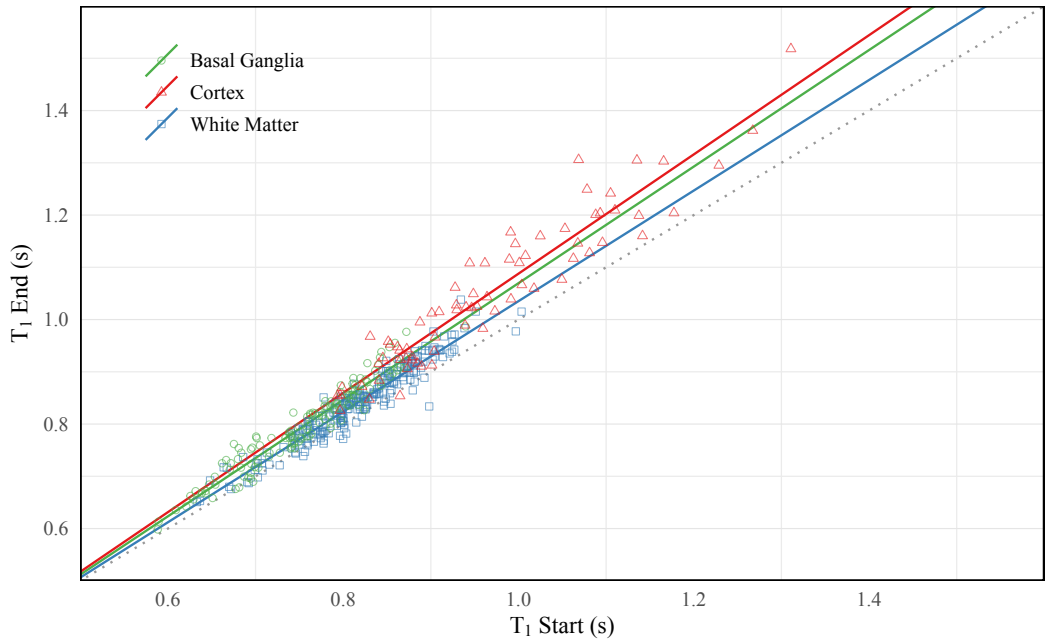

Figure 4.9: Linear regressions between T_1 measured at the beginning and end of the scan session, shown separately for each brain region. Each point represents a tissue sample: basal ganglia (green circles), cortex (red triangles), and white matter (blue squares). Colored lines indicate region-specific linear fits; the dotted gray line represents the identity line ($y = x$), corresponding to no intra-scan variation. The deviation from this line reflects an increase in T_1 during scanning, likely due to progressive tissue warming.

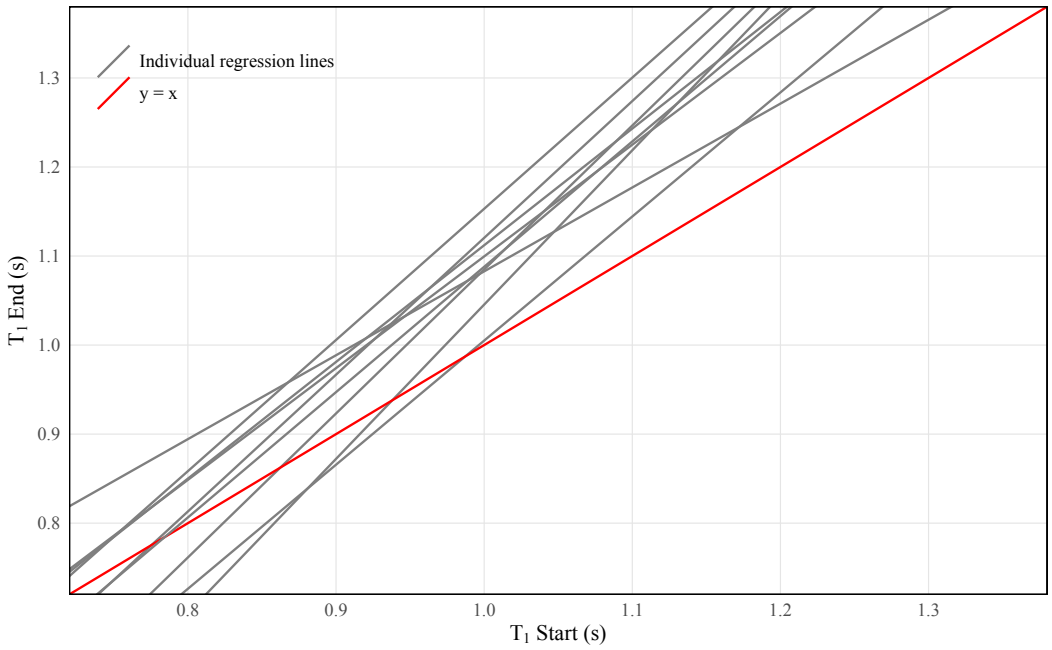

Figure 4.10: Regression analysis of cortical T_1 values at the beginning and end of the MRI session. Subject-wise fits are shown in gray; the red identity line ($y = x$) indicates perfect correspondence.

Subj ID	WM Slope	BG Slope	CX Slope
1	0.87	1.17	–
2	1.01	1.24	–
3	1.00	1.09	–
4	0.96	1.32	–
5	1.00	1.35	–
6	1.21	1.20	1.62
7	1.12	1.15	1.31
8	1.07	1.20	1.39
9	1.04	1.39	1.47
10	1.19	1.15	1.73
11	1.06	1.38	1.54
12	0.98	1.59	0.94
13	1.09	1.44	1.25

Table 4.6: Linear regression results modeling T_1 values at the end of the scan as a function of those at the beginning, reported separately for each brain region. All models showed strong linear relationships with high R^2 values. Abbreviations: BG = basal ganglia, WM = white matter, CX = cortex.

Region	Slope	Intercept (s)	R^2
Basal Ganglia	1.28 ± 0.04	–0.17 ± 0.03	0.96 ± 0.01
White Matter	1.05 ± 0.03	–0.01 ± 0.02	0.88 ± 0.02
Cortex	1.41 ± 0.09	–0.32 ± 0.10	0.87 ± 0.02

Table 4.7: Summary of subject-level linear regression models between T_1 values at the beginning and end of the scan across brain regions. Values are reported as mean ± standard deviation.

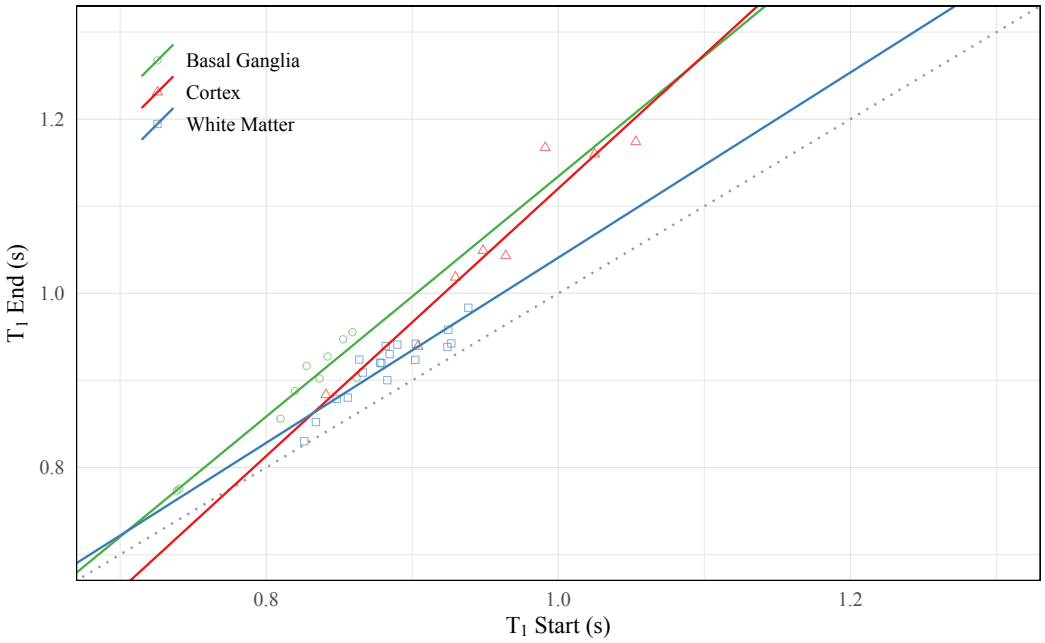

Figure 4.11: Subject-specific linear regressions between T_1 values at the beginning and end of the scan for a subject, plotted separately for each brain region. Colored points represent individual samples from the basal ganglia (green circles), cortex (red triangles), and white matter (blue squares). Dashed lines show region-wise regression fits, and the dotted gray line indicates the identity line $y = x$.

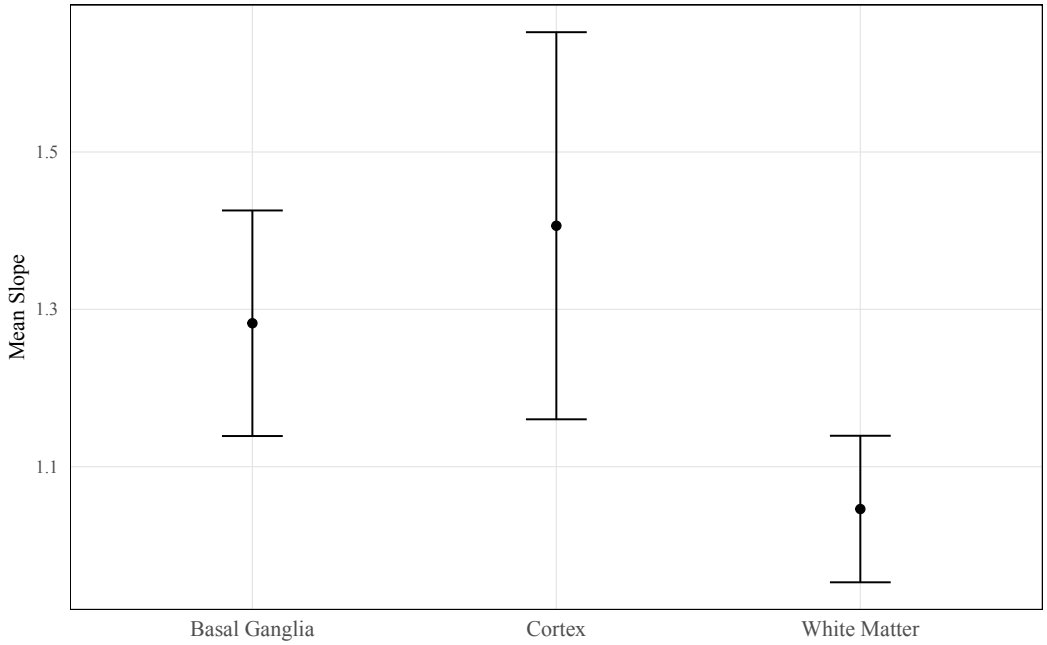

Figure 4.12: Mean slopes of the linear regressions between $T_{1,\text{start}}$ and $T_{1,\text{end}}$ for each tissue type. Error bars indicate standard deviation across subjects.

cortex ($p = 0.43$). These results are visualized in Figures 4.12 and 4.13.

Mixed-effects models and model selection

To account for repeated measures and inter-subject variability, a linear mixed-effects model was fitted with brain region and T_1 start value (and their interaction) as fixed effects, and a subject-level random intercept. As shown in Table 4.8, a significant interaction term for white matter suggests a weaker relationship between initial and final T_1 in this region compared to the baseline (basal ganglia). No significant interaction was found for cortex. Residual inspection (Figure 4.14) indicated heteroscedasticity, especially for high T_1 values in cortical samples, suggesting the need for caution in interpreting model assumptions.

To validate these results, region-specific mixed-effects models were also fitted. As shown in Table 4.9, these models confirmed the previously observed trends: the slope was lowest in white matter, and higher in cortex and basal ganglia. Residual diagnostics were satisfactory overall. AIC comparisons (Ta-

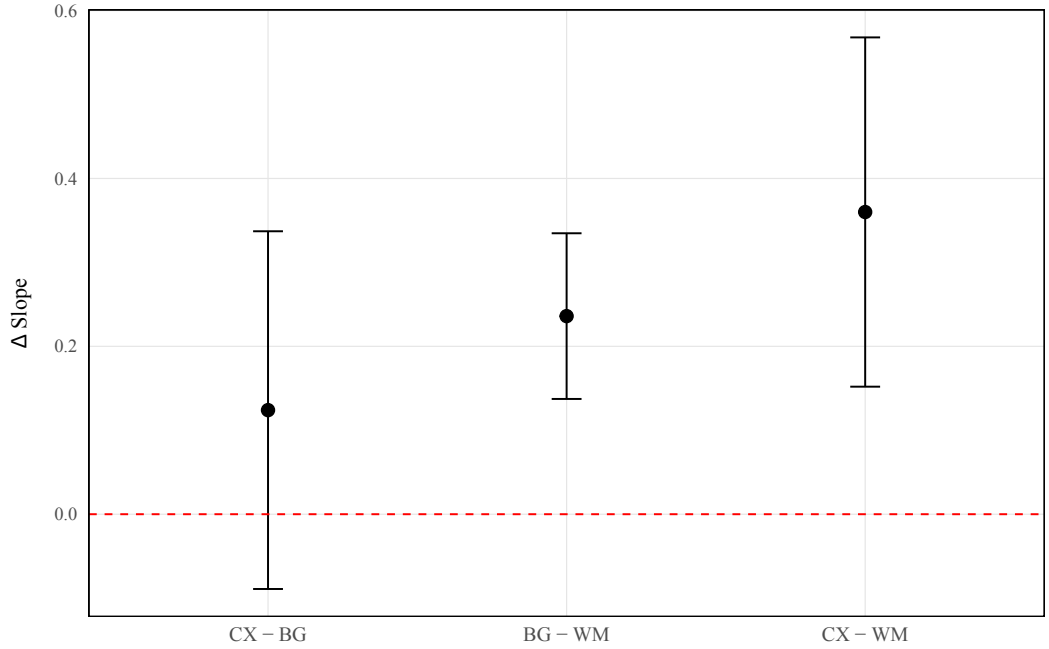

Figure 4.13: Pairwise differences in mean slope estimates between basal ganglia (BG), white matter (WM), and cortex (CX), with 95% confidence intervals. Differences are considered significant when the confidence interval does not cross zero.

Fixed Effects			
Term	**Estimate**	**Std. Error**	**t-value**
Intercept	–0.075	0.025	–3.02
T_1 Start	1.153	0.032	35.80
Cortex Effect	–0.048	0.033	–1.48
White Matter Effect	0.070	0.031	2.29
$T_{1,\,\text{Start}} \times$ Cortex	0.056	0.039	1.45
$T_{1,\,\text{Start}} \times$ White Matter	–0.118	0.039	–3.01
Random Effects			
Effect	**Variance**	**Std. Dev.**	
Subject Intercept	0.00017	0.013	
Residual	0.00054	0.023	

Table 4.8: Linear mixed-effects model results for each brain region. Models include a fixed effect for T_1 at the beginning of the scan and a subject-specific random intercept to account for inter-individual variability.

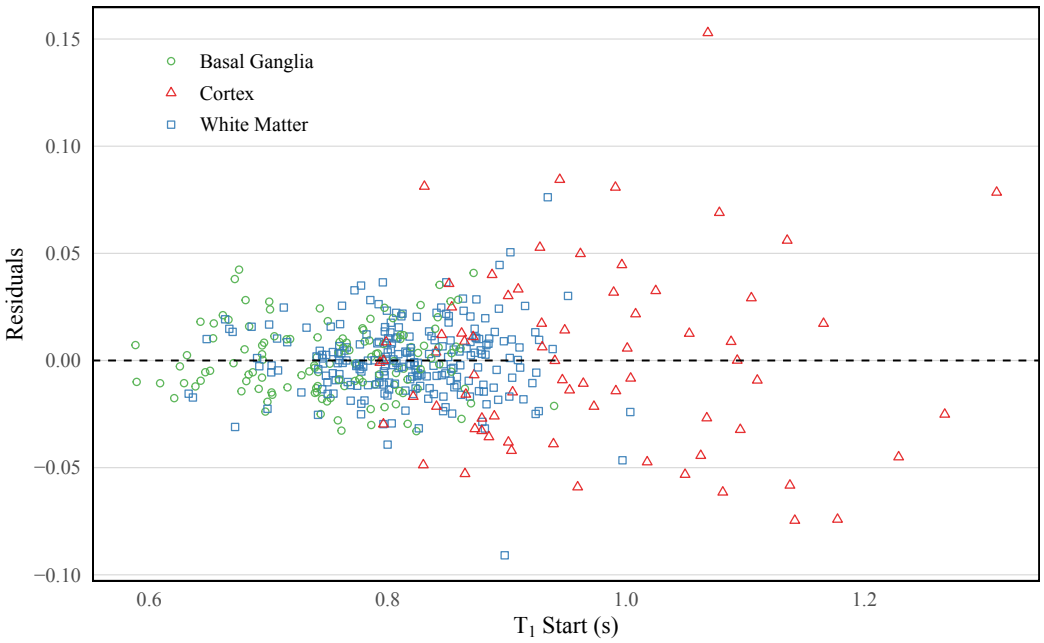

Figure 4.14: Residuals from the linear mixed-effects model predicting T_1 at the end of the scan as a function of T_1 at the beginning. Each point represents a sample, color-coded and shaped by brain region: basal ganglia (green circles), cortex (red triangles), and white matter (blue squares). The dashed horizontal line at zero indicates perfect model fit. Residuals are symmetrically distributed around zero; vertical spread in cortical samples suggests higher residual variance compared to other regions.

	Intercept (s)	**Slope**	**Inter-subject Var. (%)**	**Residual Var. (%)**
Basal Ganglia	–0.14 ± 0.02	1.24 ± 0.03	66.90	33.10
White Matter	–0.00 ± 0.02	1.03 ± 0.02	31.12	68.88
Cortex	–0.11 ± 0.06	1.19 ± 0.06	15.80	84.20

Table 4.9: Results from linear mixed-effects models fitted separately for each brain region to predict T_1 at the end of the scan based on T_1 at the beginning. Reported values include the intercept and slope of the fixed effects, and the percentage of variance attributed to inter-subject and residual components.

	Model	**AIC**
Basal Ganglia	Linear Model	–615.2
	Mixed-Effects Model	–676.7
White Matter	Linear Model	–1153.0
	Mixed-Effects Model	–1187.1
Cortex	Linear Model	–230.9
	Mixed-Effects Model	–217.6

Table 4.10: Comparison of Akaike Information Criterion (AIC) values between standard linear regression and linear mixed-effects models for each brain region. Lower AIC values indicate a better model fit.

ble 4.10) suggested that the mixed-effects model provided a better fit than the simple linear model for basal ganglia and white matter, while the linear model was slightly preferred for cortex.

In summary, T_1 values increased from the beginning to the end of the scan session, likely due to progressive tissue warming. This increase was more pronounced in gray matter (basal ganglia and cortex) compared to white matter. This suggest a convergence toward a common final temperature (approximately room temperature) by the end of the scan. The following section investigates the relationship between iron concentration and R_1.

	Mean ± SD (mg/kg)	Median (Q1–Q3) (mg/kg)
Basal Ganglia	146 ± 51	133 (105–179)
White Matter	44 ± 12	43 (35–51)
Cortex	35 ± 12	33 (27–42)

Table 4.11: Iron concentration in basal ganglia, white matter, and cortex, reported as mean ± standard deviation (SD) and median with interquartile range (Q1–Q3).

4.3 Iron Effects on R_1 Variation

Region-wise summary of iron concentration

To characterize iron content across brain tissues, the mean, median, and standard deviation (SD) of iron concentration were computed for each region of interest (ROI), as reported in Table 4.11. A visual representation is provided in Figure 4.15. The Shapiro–Wilk test indicated non-normal distribution of iron concentration in all three regions ($p < 0.05$). Consequently, a non-parametric Kruskal–Wallis test was applied, revealing a significant effect of brain region on iron concentration ($p < 0.01$). Post hoc pairwise comparisons using Dunn's test with Bonferroni correction showed significantly higher iron levels in the basal ganglia compared to both white matter and cortex ($p < 0.01$). In addition, white matter had significantly higher iron content than cortex ($p < 0.01$).

Region-specific linear regression models

To evaluate the relationship between iron concentration and longitudinal relaxation rate (R_1), linear regression models were fitted separately for each brain region. The results are summarized in Table 4.12. In the basal ganglia, the regression showed a significant positive association ($p < 0.01$) with a modest explanatory power ($R^2 = 0.15$), indicating that iron concentration accounts for a small proportion of R_1 variability. This relationship is illustrated in Figure 4.16. In white matter, the association was weak and negative ($R^2 = 0.02$), with a slope that was marginally significant ($p = 0.05$). In the

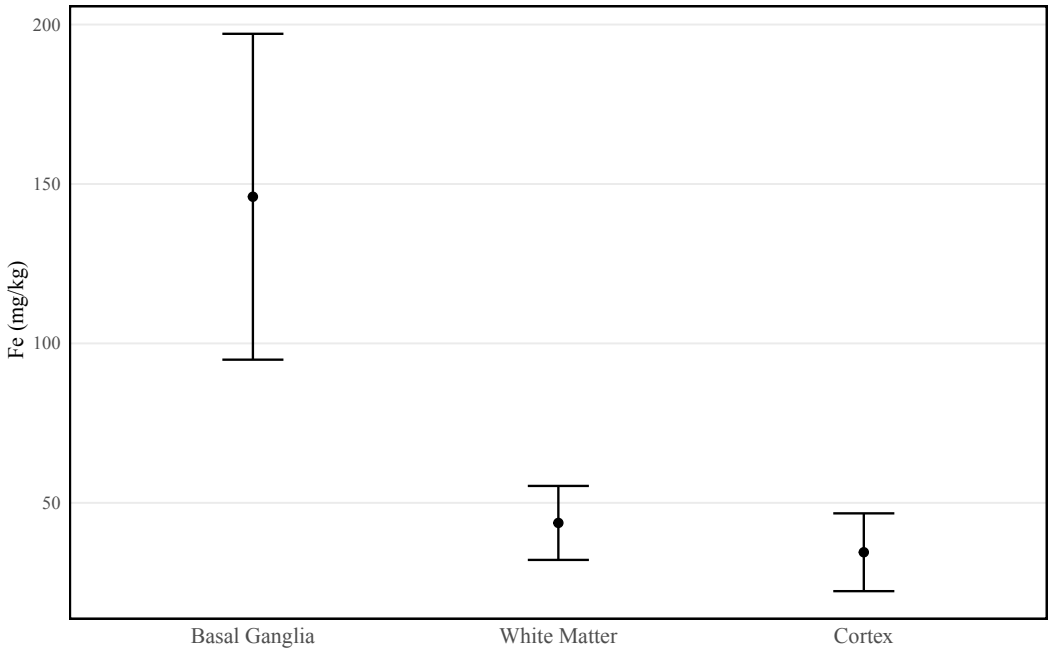

Figure 4.15: Mean iron concentration across brain regions, measured in mg/kg of fresh tissue. Vertical error bars represent ±1 standard deviation.

	Intercept (s^{-1})	**Slope (s^{-1}/mg/kg)**	**R^2**	**p-value**
Basal Ganglia	1.12	1.01×10^{-3}	0.15	**<0.01***
White Matter	1.25	-1.15×10^{-3}	0.02	0.05
Cortex	0.86	3.08×10^{-3}	0.09	**0.01***

Table 4.12: Linear regression results between iron concentration and R_1 in different brain regions.

cortex, a significant positive slope was observed ($p = 0.01$), but the low R^2 value ($R^2 = 0.09$) suggests limited predictive value of the linear model. The cortical relationship is shown in Figure 4.17.

Residual diagnostics were performed to assess the validity of model assumptions. According to the Shapiro–Wilk test, residuals in basal ganglia and cortex did not significantly deviate from normality ($p = 0.10$ and $p = 0.34$, respectively), while the white matter model failed the normality test ($p < 0.01$). Nonetheless, Q–Q plots and residual histograms revealed only minor deviations from normality, mostly confined to the distribution tails (Figure 4.18).

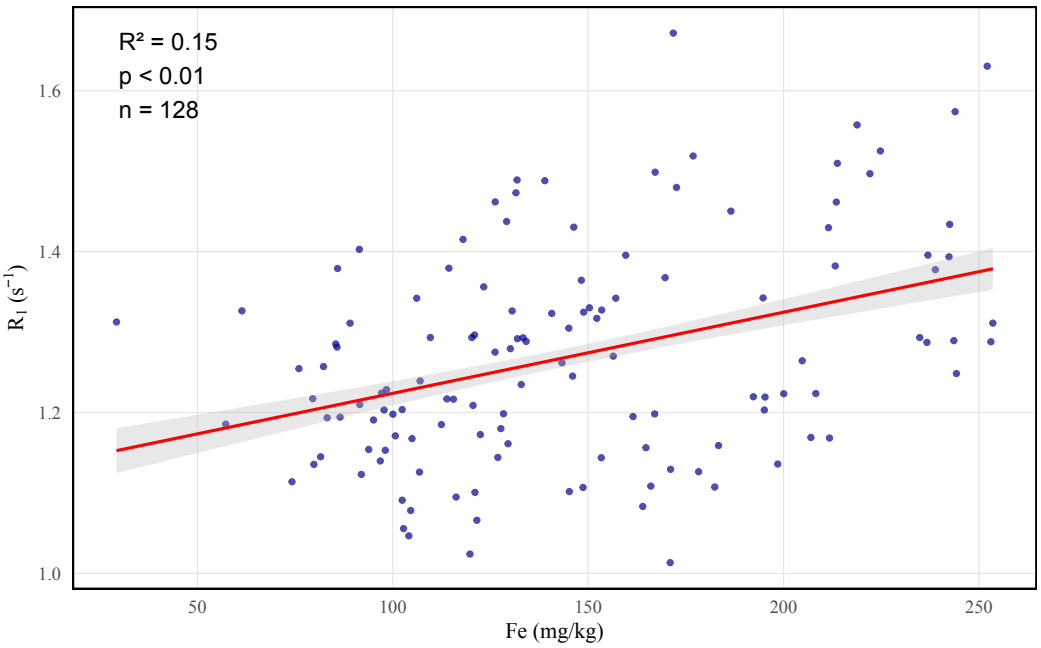

Figure 4.16: Linear regression between iron concentration and R_1 in the basal ganglia. Each point represents a matched MRI–ICP-MS sample. The regression line is shown with ±1 standard error (SE).

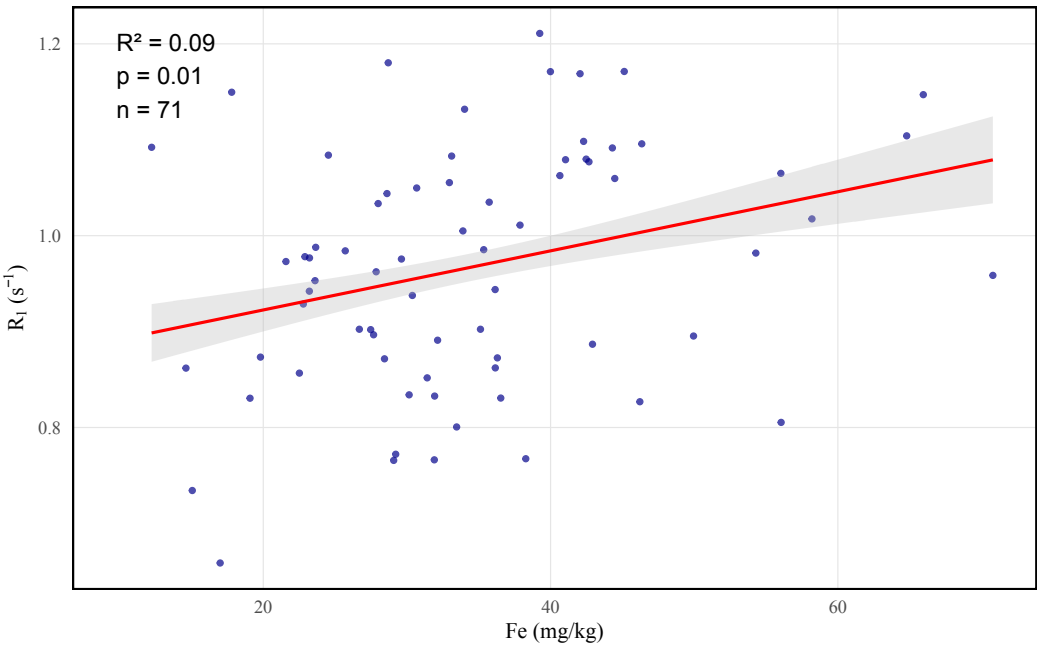

Figure 4.17: Linear regression between iron concentration and R_1 in the cortex. Each point represents a matched MRI–ICP-MS sample. The regression line is shown with ±1 standard error (SE).

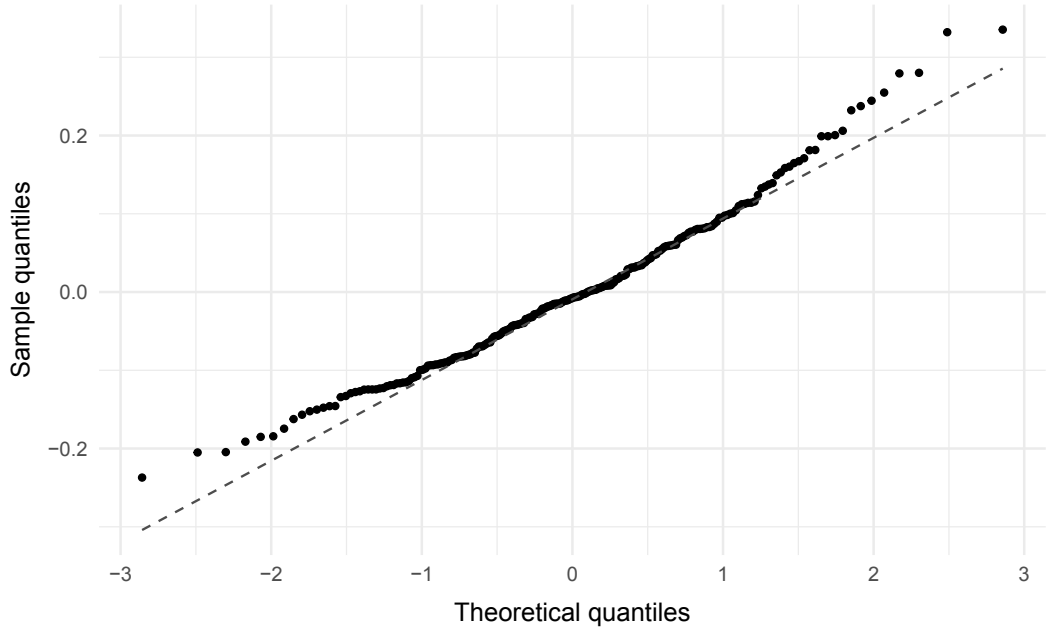

Figure 4.18: Q–Q plot of residuals from the linear regression model between iron concentration and R_1 in white matter. Despite the Shapiro–Wilk test indicating non-normality, visual inspection reveals only minor deviations from the expected normal distribution.

Subject-specific regression models

To assess inter-individual variability in the relationship between iron concentration and longitudinal relaxation rate, subject-specific linear regression models were fitted separately for each brain region. Table 4.13 reports the mean ± standard error (SE) of slope, intercept, and R^2 across individual models, along with the number of subjects exhibiting statistically significant fits.

In the basal ganglia, regression slopes were generally positive, ranging from 3.7×10^{-4} to 6.5×10^{-3}. Most intercepts were close to 1.0, with values spanning 0.89 to 1.23. These results are visualized in Figure 4.19, which displays individual regression lines for each subject.

In the white matter, regression slopes varied in direction, ranging from -6.9×10^{-3} to 9.7×10^{-3}, with weak overall associations (R^2 ranging from $<$ 0.01 to 0.44). Intercepts spanned 1.07 to 1.66, and only two models reached significance.

In the cortex, regression slopes were predominantly positive, ranging from 1.0×10^{-3} to 1.1×10^{-2}, with modest associations (R^2 between 0.02 and 0.62).

	Intercept (s^{-1})	**Slope (s^{-1}/mg/kg)**	**R^2**	**n**
Basal Ganglia	0.98 ± 0.05	$(2.1 \pm 0.5) \cdot 10^{-3}$	0.65 ± 0.07	11
White Matter	1.22 ± 0.05	$(-3.5 \pm 1.2) \cdot 10^{-4}$	0.10 ± 0.04	2
Cortex	0.80 ± 0.05	$(4.8 \pm 1.9) \cdot 10^{-3}$	0.26 ± 0.08	1

Table 4.13: Summary of subject-specific linear regression models between iron concentration and R_1 across brain regions. Values are reported as mean $\pm$ standard error (SE). "n" indicates the number of significant models per region.

Intercepts varied from 0.63 to 0.98, clustering around 0.8.

Mixed-effects models and model selection

To account for repeated measurements within subjects, linear mixed-effects models were fitted for each brain region, including a fixed effect for iron concentration and a subject-specific random intercept. Model results are presented in Table 4.14.

In the basal ganglia, a significant positive association was found ($t = 10.79$), with iron concentration explaining a substantial portion of R_1 variance. The inter-subject variability accounted for 71% of the total variance, indicating considerable heterogeneity in baseline R_1 values across individuals.

In white matter, no significant relationship was observed ($t = -0.28$) and the model revealed a relatively balanced contribution of inter-subject (53.5%) and residual (46.5%) variance. In the cortex, a significant positive association was detected ($t = 3.85$), with a similar variance distribution (52.3% vs 47.7%).

Residual analysis supported the validity of the model assumptions. The Shapiro–Wilk test confirmed normal distribution of residuals in all regions, and Q–Q plots indicated symmetrical, approximately Gaussian distributions. Based on AIC comparisons (Table 4.15), mixed-effects models outperformed their corresponding fixed-effects models in all three regions, suggesting im-

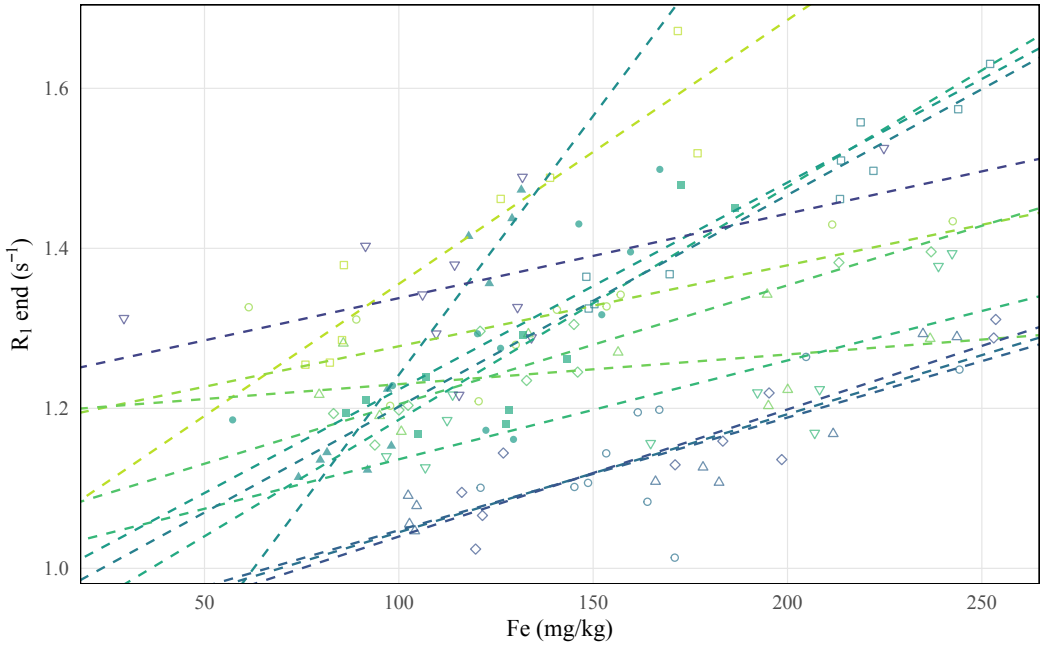

Figure 4.19: Subject-specific linear regressions between iron concentration and R_1 relaxation rate in the basal ganglia. Each point represents a matched MRI–ICP-MS measurement, and each dashed line corresponds to a linear model fitted separately for each subject. Colors and shapes are used to identify subjects.

proved model fit when accounting for subject-specific variability.

4.4 Iron Effects on R_1 in Basal Ganglia Subregions

Subregion-wise summary of iron concentration

Given the significant association observed between iron concentration and R_1 in the basal ganglia, a follow-up analysis was conducted to determine whether this relationship is consistent across its subregions–namely the putamen, caudate nucleus, and globus pallidus–or primarily driven by regional differences in iron content. Figure 4.20 displays the scatterplot of iron concentration versus R_1, color-coded by subregion.

To assess differences in iron content among subregions, mean, median, and standard deviation (SD) were calculated and are reported in Table 4.16. As

	Intercept ($\mathbf{s^{-1}}$)	**Slope** ($\mathbf{s^{-1} \cdot kg/mg}$)	**Inter-subject Variance** (%)	**Residual Variance** (%)
Basal Ganglia	1.05 ± 0.04	$(1.55 \pm 0.14) \cdot 10^{-3}$	71.03	28.97
White Matter	1.21 ± 0.03	$(-1.70 \pm 5.90) \cdot 10^{-4}$	53.49	46.51
Cortex	0.84 ± 0.05	$(3.66 \pm 0.95) \cdot 10^{-3}$	52.32	47.68

Table 4.14: Linear mixed-effects model results describing the relationship between iron concentration and R_1 across brain regions. Reported values include the fixed-effect estimates (intercept and slope) and the proportion of total variance attributed to inter-subject and residual components.

	Model	**AIC**
Basal Ganglia	Linear Model	-164
	Mixed-Effects Model	-244
White Matter	Linear Model	-394
	Mixed-Effects Model	-501
Cortex	Linear Model	-95
	Mixed-Effects Model	-105

Table 4.15: Comparison of Akaike Information Criterion (AIC) values between standard linear and mixed-effects models for each brain region. Lower AIC values indicate better model fit.

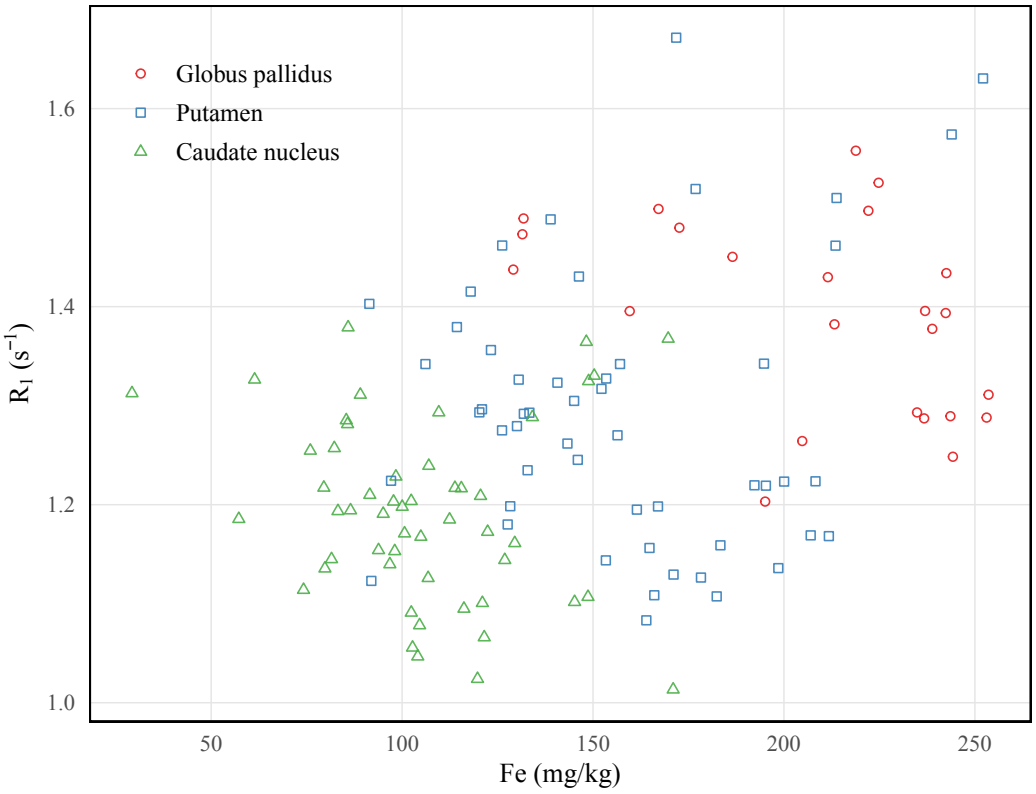

Figure 4.20: Relationship between iron concentration and longitudinal relaxation rate R_1 in basal ganglia subregions. Each point represents a tissue sample from the globus pallidus (red circles), putamen (blue squares), or caudate nucleus (green triangles).

Region	Mean ± SD (mg/kg)	Median (Q1–Q3) (mg/kg)
Globus Pallidus	208 ± 40	221 (183–240)
Putamen	158 ± 38	153 (130–183)
Caudate Nucleus	106 ± 28	103 (86–121)

Table 4.16: Iron concentration in basal ganglia subregions, reported as mean ± standard deviation (SD) and median with interquartile range (Q1–Q3).

shown in Figure 4.21, the globus pallidus exhibited the highest iron concentration, followed by the putamen and caudate nucleus. The Shapiro–Wilk test indicated normal distribution for iron values in the putamen and caudate nucleus ($p = 0.30$), but not in the globus pallidus ($p < 0.05$). A non-parametric Kruskal–Wallis test confirmed significant differences among subregions ($p < 0.01$). Post hoc Dunn's tests with Bonferroni correction revealed statistically significant differences between all pairs ($p < 0.01$).

Subregion-specific linear regression models

To further investigate the relationship between iron concentration and R_1, separate linear regression models were fitted for each subregion. Results are summarized in Table 4.17 and visualized in Figure 4.22. Notably, the globus pallidus showed a significant negative association, in contrast with the overall positive trend observed in the pooled basal ganglia analysis. This may reflect subregion-specific tissue properties or measurement variability. In all three subregions, R^2 values were low, suggesting that iron alone explains only a small fraction of the observed variability in R_1.

Residual analysis was used to assess model assumptions. The Shapiro–Wilk test confirmed normal distribution of residuals in all three subregions ($p > 0.05$). This was further supported by Q–Q plots and histogram inspection, which showed symmetrical and unimodal distributions without evidence of outliers. While each data point corresponds to a distinct sample, the possibil-

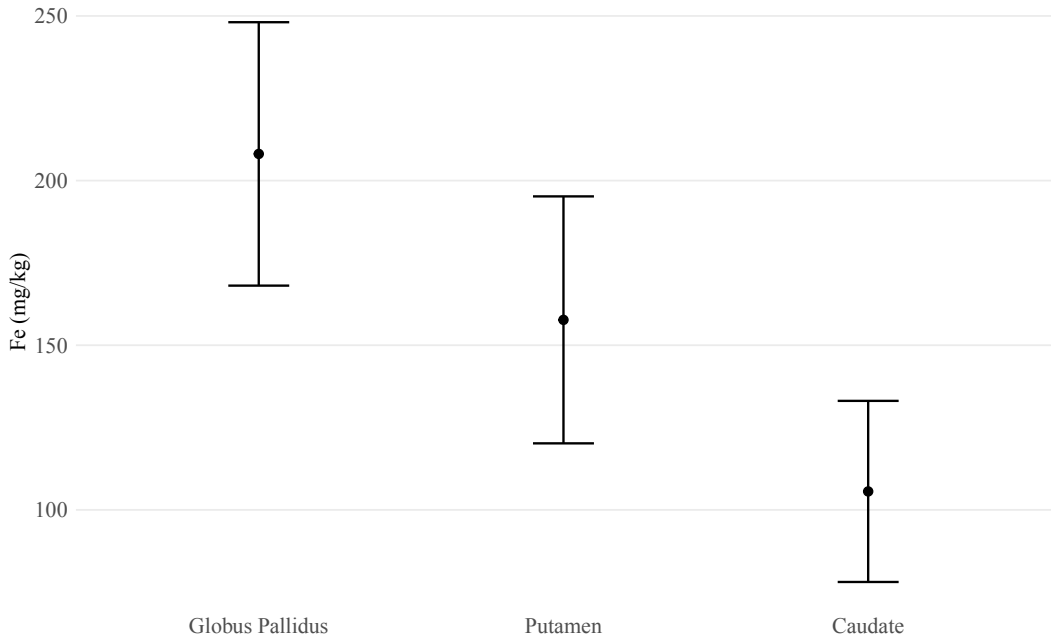

Figure 4.21: Mean iron concentration across basal ganglia subregions—globus pallidus, putamen, and caudate nucleus—expressed in mg/kg of fresh tissue. Vertical error bars represent standard deviations (SD).

	Intercept ($\mathbf{s^{-1}}$)	**Slope** ($\mathbf{s^{-1}/mg/kg}$)	**R^2**	**p-value**
Globus Pallidus	1.61	-1.07×10^{-3}	0.19	**0.03***
Putamen	1.22	0.45×10^{-3}	0.01	0.40
Caudate Nucleus	1.23	-0.39×10^{-3}	0.01	0.41

Table 4.17: Linear regression results between iron concentration (Fe) and R_1 in different basal ganglia subregions. Statistically significant results are indicated with an asterisk.

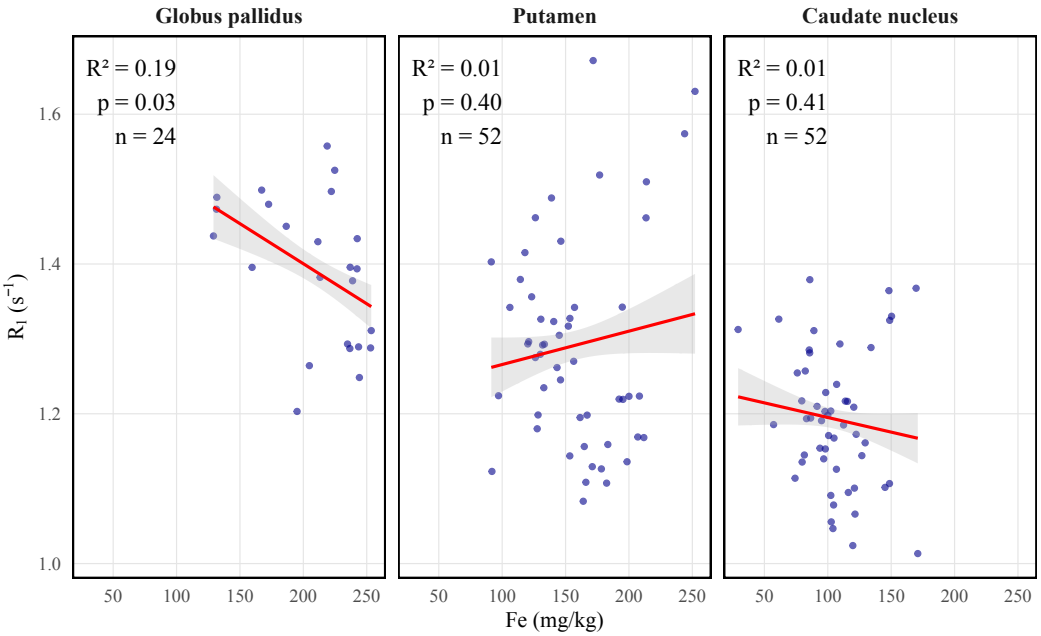

Figure 4.22: Linear regressions between R_1 and iron concentration in basal ganglia subregions. Separate models are shown for the globus pallidus, putamen, and caudate nucleus. Each subplot includes the regression line with shaded area indicating ± 1 standard error.

ity of residual dependence due to within-subject clustering cannot be entirely excluded. As such, these regression results should be interpreted with caution.

Taken together, these results highlight region-specific and subregion-specific patterns in the relationship between iron content and longitudinal relaxation. The observed variability, particularly within the basal ganglia, suggests that other tissue characteristics may modulate the effect of iron on R_1. These aspects are further explored in the Discussion section.

Chapter 5

Discussion and Conclusion

This chapter provides a critical interpretation of the results presented in the previous section, with the aim of assessing the physiological and methodological significance of the observed trends. The discussion is structured to mirror the organization of the Results chapter, enabling a focused interpretation of each specific analysis. Particular attention is given to the reliability of temperature measurements and their influence on T_1 estimation, the tissue-specific sensitivity to temperature changes, and the potential role of iron content in modulating R_1 values. Limitations related to experimental design, such as post-mortem interval, and intra-subject data structure, are also addressed. The chapter concludes with a summary of the main findings, highlighting their implications for future post-mortem MRI reasearch and for the interpretation of relaxation parameters under post-mortem conditions.

5.1 Temperature Dependence of T_1 Relaxation

The results of this study confirm a temperature dependence of longitudinal relaxation time (T_1) in post-mortem brain tissue, with significant positive trends observed in gray matter regions such as the cortex and basal ganglia. These findings align with prior literature reporting linear temperature–T_1 relationships in unfixed, in-situ post-mortem brain tissue [10, 48, 50]. However, the temperature coefficients estimated here are notably lower than those reported by *Birkl et al.* [9, 36], who conducted controlled heating of unfixed brain slices to precisely quantify the temperature-dependent relaxation changes. This discrepancy likely reflects a central difference of the present dataset: the temperature values used in the regression analysis were based on core body temperature measurements acquired externally (e.g., in the body bag) several hours before the MRI scan. Such measurements are not only temporally displaced, but they may also be physiologically distant from the actual brain temperature during acquisition, which can differ substantially from core body temperature due to region-specific cooling dynamics and thermal equilibration occurring over time [78].

Post-mortem brain temperature is also known to change during scanning

due to both passive thermal equilibration with the ambient environment and RF-induced heating, resulting in gradual warming of brain tissue toward room temperature [8, 79]. In the present analysis, the lack of real-time brain or forehead temperature monitoring precluded accurate estimation of the tissue temperature at the time of image acquisition, thereby undermining the quantitative robustness of the regression. Notably, despite white matter presenting an extrapolated T_1 value closest to the literature reference, the regression model in this region yielded a negative and non-significant slope, further highlighting the unreliability of the core temperature data. In line with previous findings, the minimal temperature dependence observed in white matter may also reflect inherent biophysical properties of this tissue, such as the limited molecular mobility in the intracellular cytoplasm of myelinated axons and the overall lower water content compared to gray matter, both of which are known to influence longitudinal relaxation dynamics [80, 81].

As shown in Table 4.3, T_1 values extrapolated to 37°C were consistently lower than in vivo reference values, with discrepancies ranging from –6.2% in white matter to –38.2% in the basal ganglia. While such underestimation may suggest an intrinsic post-mortem shift in relaxation behavior, previous studies have shown that accurate extrapolation can yield values close to in vivo reference even in unfixed tissue. In particular, *Birkl et al.* [9] performed controlled heating of unfixed brain samples and obtained extrapolated T_1 estimates at 37°C that closely matched those measured in living subjects. The discrepancy observed here therefore likely reflects methodological limitations — chiefly, the imprecise estimation of brain temperature at scan onset. In addition, unmodeled covariates such as post-mortem interval, tissue hydration, and myelin content may contribute to regional T_1 variability and should be considered in future studies aiming to bridge post-mortem and in vivo relaxation metrics.

It is also important to acknowledge that T_1 values in the cortex were available only for a subset of subjects, due to the progressive extension of ROI segmentation during the study. This reduced sample size may have influenced the stability of the regression estimates and limited the generalizability of the cortical results. Consequently, comparisons between cortical and subcortical

structures should be interpreted with caution, as they may be partially confounded by unequal subject representation across regions.

Additionally, while tissue temperature in this study was not directly measured and was unlikely to reach critical thresholds, it is worth noting that elevated temperatures can, in other contexts, accelerate enzymatic degradation in unfixed samples [44]. Hence, thermal monitoring remains advisable in post-mortem MRI, especially for long or high-energy protocols.

Direct comparison with previous studies is further complicated by substantial differences in experimental setup. While *Zech et al.* [48] relied on core temperatures measured in the esophagus, and *Birkl et al.* [9] performed controlled heating of extracted brain tissue, the present study was conducted in situ without the possibility of acquiring brain temperature data or scanning the same subjects at multiple temperature points. These constraints limited the ability to quantify subject-specific temperature effects and to assess the role of underlying structural features, such as regional myelin content, in modulating T_1 [1]. Although pooling measurements across voxels and regions may have reduced intra-subject variability due to tract-specific effects, it likely averaged out physiologically meaningful differences in tissue composition, particularly in white matter.

Moreover, variations in post-mortem interval (PMI), tissue hydration, and water content can alter relaxation properties, especially in white matter where low water content and anisotropic microstructure constrain molecular mobility [82]. In particular, PMI has been shown to influence the biochemical composition of brain tissue, including metabolite concentrations measurable via MRS [47]. As PMI increases, ongoing autolysis and decomposition processes may progressively modify tissue integrity and microstructure, potentially altering relaxation dynamics [82]. In the present study, PMI varied between subjects and was not included as a covariate in the regression models. This decision was motivated by the inverse relationship observed between PMI and initial core temperature: longer PMI typically corresponds to prolonged refrigeration and, consequently, lower temperature at the time of scanning. Including both variables as independent predictors would likely introduce multicollinear-

ity, making it difficult to disentangle their individual contributions. Although PMI was not explicitly modeled, its potential influence on tissue characteristics may have contributed to inter-subject variability and to the uncertainty of the estimated regression slopes.

An additional aspect relates to the structure of the dataset, which includes multiple T_1 measurements per subject and per region. In this context, the assumption of independence underlying simple linear models may not be fully met. Although the naive pooled regression approach—treating all observations as independent—offers a useful descriptive framework and facilitates comparison with previous studies, it does not explicitly account for within-subject dependencies. To address this limitation and better model intra-subject variability, additional analyses were performed using linear mixed-effects models.

While visual inspection of residuals did not suggest clear model violations, the resulting p-values and slope estimates must be interpreted cautiously. Overall, given the cumulative impact of these limitations–especially the unreliable temperature estimates–the regression analysis should be viewed as descriptive rather than inferential, and interpreted primarily as a qualitative exploration of temperature-related trends.

To avoid the issue of poorly defined absolute core temperatures, a complementary analysis was performed by comparing T_1 values at the beginning and end of each scan session, thus leveraging within-scan thermal dynamics to isolate temperature-driven changes. This approach — closer to the strategies adopted in studies using real-time forehead or brain temperature monitoring [10, 50] — provides an alternative and potentially more robust means of capturing temperature effects in post-mortem MRI. The results of this analysis are discussed in the following section.

5.2 Intra-Scan Temperature Effects on T_1

The comparison between T_1 values at the beginning and end of the scan revealed a consistent increase across all brain regions, with the most pronounced effect observed in gray matter. These findings are in line with the hypothesis

that brain tissue warms progressively during the scanning session, likely due to a combination of passive thermal equilibration with the ambient environment and RF-induced heating [8, 79]. Although direct temperature measurements were not available, the observed trends are consistent with prior studies in post-mortem imaging showing gradual warming of brain tissue over time [10, 50].

The high correlation ($r = 0.96$) between start and end T_1 values suggests that despite the temperature rise, the relative differences in relaxation times across regions and subjects are preserved. Linear regression analyses confirmed significant increases in T_1 with strong fits ($R^2 > 0.90$) in all brain regions, with slopes highest in the cortex, followed by the basal ganglia and white matter. However, this ordering was not consistent across models: in the linear mixed-effects model, the slope for the basal ganglia was slightly greater than that of the cortex, and the subject-specific regression models showed no significant difference between these two regions. These results suggest that, while earlier studies have reported higher temperature sensitivity in the cortex [9, 36], the present data do not support a significant distinction in slope between the two gray matter structures. This consistency across models reinforces the idea that gray matter as a whole exhibits stronger temperature dependence than white matter, but without substantial differentiation between its subregions.

Individual-level analyses further support these findings, showing that slopes were consistently lower for white matter across most subjects. The significance of these differences was statistically confirmed through Welch's ANOVA and post hoc comparisons, which revealed that white matter differed significantly from the cortex and basal ganglia, while no significant differences were found between the two gray matter regions. These observations are consistent with earlier findings and support the notion that white matter's relaxation behavior is less influenced by temperature variation, likely due to its structural composition.

The application of mixed-effects models added further robustness to the interpretation by accounting for inter-subject variability. The results confirmed a significant interaction between initial T_1 values and brain region, particularly

in white matter, where the slope relating $T_{1,\text{start}}$ to $T_{1,\text{end}}$ was lower than in other regions. Notably, the random effect component was minimal, suggesting that most of the observed variance is attributable to fixed effects rather than subject-specific differences. This supports the generalizability of the observed trends across the study cohort.

Finally, model comparison based on Akaike Information Criterion (AIC) values provided further insights into model adequacy across regions. As shown in Table 4.10, the mixed-effects model was preferred over the simple linear model for both the basal ganglia and white matter, indicating that incorporating subject-level variability improves model performance in these regions. In contrast, for the cortical region, the linear model yielded a lower AIC, suggesting that additional subject-level random effects did not substantially enhance model fit. This result is consistent with the relatively low inter-subject variance estimated in the cortex and may reflect more homogeneous T_1 responses to temperature in this region. It is also worth noting that this finding could be influenced by the smaller number of subjects with available cortical measurements compared to the basal ganglia and white matter (8 vs. 13 subjects), potentially limiting the ability of the mixed-effects model to capture subject-level variability in this region. This caveat applies more broadly to all cortex-related analyses, including pooled and individual-level regressions, which were necessarily based on a reduced subset of subjects.

Intra-scan temperature effects are particularly critical in post-mortem imaging, where the absence of thermoregulatory mechanisms can result in considerable heating during high-resolution acquisitions. Unlike the in vivo setting — where perfusion and vasodilation help maintain tissue homeostasis — unfixed post-mortem samples are thermally passive, and the energy absorbed from continuous RF pulses is not dissipated [31]. Inversion recovery sequences, especially those with long repetition times (TR), are associated with higher energy deposition, increasing the likelihood of progressive tissue warming during the scan [31]. These effects are further exacerbated when the initial temperature of the specimen is lower than ambient, as commonly occurs with refrigerated samples.

Although the results were consistent across modeling approaches, it is important to note that both the initial region-wise regressions and subject-specific models assumed independence between observations. In the case of the pooled models, this may have led to underestimation of standard errors, while the subject-level regressions, although more robust to clustering, did not correct for unequal sample sizes across subjects or regions. These limitations were partially mitigated by the application of linear mixed-effects models, which formally incorporated subject-level variability and provided a more appropriate framework for inference.

Despite the strength of these results, some limitations must be acknowledged. The lack of direct temperature monitoring prevents precise estimation of the temperature change during the scan. In addition, the assumption that all subjects reached similar final temperatures is unverified and could introduce bias, especially if different subjects started at different thermal states or experienced heterogeneous heating rates. The cone-shaped residual pattern observed in the mixed model further suggests that temperature-related variability may not be fully captured, particularly in regions like the cortex where heating might be more rapid or substantial.

Overall, the intra-scan T_1 variation provides compelling indirect evidence of temperature effects on longitudinal relaxation time and supports the hypothesis that tissue temperature increases during the course of the MRI acquisition. This reinforces the importance of accounting for scan duration and thermal dynamics when interpreting post-mortem T_1 measurements, especially in studies aiming to compare across individuals or time points.

5.3 Iron-Related Modulation of R_1

The relationship between iron concentration and the longitudinal relaxation rate (R_1) was examined across different brain regions using multiple statistical approaches. A significant positive association was observed in the basal ganglia, consistent with its high iron concentration as previously reported in the literature [53, 54] and confirmed in the present dataset (see Table 2.1). How-

ever, the coefficient of determination was relatively low ($R^2 = 0.15$), suggesting that iron concentration accounts for only a limited portion of the variability in relaxation rate. In white matter, a negative and borderline-significant trend was observed ($p = 0.05$), whereas the cortical region showed a statistically significant positive slope but a similarly low explanatory power ($R^2 = 0.01$). These findings indicate that, although a correlation exists in some regions, the strength of the association is modest and possibly influenced by other tissue-specific factors.

It is important to note that iron concentrations reported in this study were obtained using inductively coupled plasma mass spectrometry (ICP-MS) on tissue samples. This technique provides an absolute and highly sensitive measure of total elemental iron in milligrams per kilogram of fresh brain tissue, and has been validated in previous post-mortem imaging studies, including QSM-based investigations [56]. However, it does not distinguish between chemical forms of iron (e.g., ferritin-bound vs. labile), nor does it account for microstructural properties such as compartmentalization, myelin content, or water mobility. These factors - especially relevant in white matter - may modulate the effectiveness of iron-proton interactions and help explain the weaker and more variable R_1 dependencies observed in regions with lower iron concentrations (see Fig. 4.15).

Subject-specific regression models revealed further complexity. In the basal ganglia, most subjects showed a positive slope between R_1 and iron, with slope estimates ranging from 3.7×10^{-4} to 6.5×10^{-3} $\mathrm{s}^{-1}/(\mathrm{mg/kg})$. This reinforces the idea of an overall positive association at the population level. However, individual model performance varied considerably in terms of explained variance, and not all models reached significance. In the cortex and white matter, findings were more heterogeneous, with slope directions varying and only a few significant models. These inconsistencies emphasize the role of inter-subject variability and microstructural differences in shaping R_1 values, particularly in regions with lower iron content.

Mixed-effects models provided more robust estimates by incorporating subject-level random effects. These models confirmed a significant positive

relationship between iron and R_1 in both the basal ganglia and cortex, but not in white matter. In the cortex, the limited number of subjects with available iron and R_1 data may have reduced the sensitivity of the models, and the results should be considered preliminary. In the basal ganglia, the slope estimate from the mixed-effects model was higher than in the global linear model, and most of the variance was attributable to inter-subject differences. This suggests that while iron contributes to the relaxation rate in this region, baseline differences between individuals (e.g., age, PMI, or brain temperature) play an important role. The model comparison via AIC confirmed that mixed-effects models provided better fit across all regions, highlighting the importance of accounting for subject-level heterogeneity when studying biophysical tissue in post-mortem data. However, even when inter-subject variability is explicitly modeled, the association between R_1 and iron likely reflects the influence of additional unmeasured covariates — such as tissue hydration, myelin content, or temperature — that were not included in the models. These factors may interact with iron concentration in region-specific ways, limiting the generalizability of the observed relationships.

A critical concern, however, is whether the significant iron-R_1 association observed in the basal ganglia reflects a true continuous relationship or is confounded by regional clustering of iron values. Indeed, the globus pallidus exhibited substantially higher iron concentrations than the caudate nucleus and putamen, consistent with prior studies [53, 54]. The large inter-subregional differences may inflate the correlation observed when treating the basal ganglia as a single pooled region. To address this, regression analyses were repeated separately within each subregion. Results showed that only the globus pallidus had a significant (and unexpectedly negative) association between iron and R_1, while the putamen and caudate nucleus did not show significant relationships. Moreover, the direction of the slope in the globus pallidus contradicts the general expectation, raising doubts about the robustness of the overall finding. Rather than a true region-wide association, this pattern likely reflects a confounding effect introduced by aggregating structurally and chemically heterogeneous subregions. This kind of artifact–sometimes referred to as *ag-*

gregation bias or *ecological fallacy*–occurs when a correlation observed at the group level does not hold within the subgroups, due to systematic differences in group means. Such effects emphasize the importance of stratified analyses, especially when interpreting relaxation-iron relationships across anatomically heterogeneous brain structures, where pooled associations may obscure more complex or divergent local behaviors. In this case, the apparent relationship between iron and R_1 may be primarily driven by the higher mean iron concentration in the globus pallidus, rather than a meaningful voxel-wise or subject-level relationship across the basal ganglia.

Such interpretation aligns with prior evidence. Studies by *Vymazal et al.* [22] and *Koenig et al.* [68] found that while regional iron concentration can explain inter-regional differences in R_1, intra-regional correlations are often weak or absent. Similarly, the study by *Ogg et al.* [13] demonstrated substantial regional differences in iron relaxivity across cortex, white matter, and basal ganglia, suggesting that the magnetic and biochemical state of iron - as well as its interaction with surrounding water and myelin - varies substantially across the brain. This is further supported by the observation that regions such as the cortex and white matter, which contain lower and more homogeneous iron concentrations (as shown in Fig. 4.15), exhibited weaker and more inconsistent R_1 dependencies.

Temperature may also influence the observed associations. According to Curie's Law, the paramagnetic susceptibility of iron decreases with increasing temperature, potentially reducing its impact on R_1 [75]. Since brain temperature during post-mortem MRI is not constant and not directly measured in this dataset, inter-subject variability in temperature may contribute to the observed inter-subject variance and to the region-specific model differences. This is particularly relevant given that the mixed-effects model for the basal ganglia attributed more than 70% of variance to inter-subject effects.

Additionally, it should be acknowledged that prolonged post-mortem interval (PMI) may not only alter general tissue integrity but also influence the mobility and binding state of iron, thereby affecting its contribution to relaxation behavior. Although the direct effect of PMI on iron relaxivity remains

poorly characterized, prior studies have shown that autolytic processes during decomposition can disrupt the molecular structure and water compartmentalization [82, 83]. These alterations may interfere with the magnetic interactions between iron and surrounding water protons, particularly in unfixed tissue. In this dataset, PMI ranged from 12 to 64 hours, introducing an additional layer of subject-level variability that cannot be explicitly modeled but should be considered when interpreting the model and region-specific iron-R_1 associations.

In conclusion, while the data provide partial evidence of an association between iron concentration and R_1 in post-mortem brain tissue–especially in the basal ganglia–this relationship appears modest, region-specific, and potentially confounded by inter-subregional clustering and subject-level factors. The results underscore the complexity of iron-related relaxation mechanisms and support the need for future multimodal studies combining quantitative MRI, histology, and biochemical mapping to disentangle the effects of iron, myelin, temperature, and tissue degradation in post-mortem brain imaging.

5.4 General Conclusions and Future Perspectives

This study provides an integrative assessment of how temperature and iron concentration influence longitudinal relaxation parameters in post-mortem brain tissue. By combining quantitative MRI with post-mortem biochemical analyses, it offers complementary perspectives on the biophysical mechanisms underlying T_1 and R_1 variability in unfixed human brains.

Three key findings emerge from the analyses:

- T_1 relaxation time shows clear sensitivity to temperature changes, both across and within scan sessions. This effect is stronger in gray matter than in white matter, consistent with prior evidence and the known structural differences between these tissue types.
- A significant positive association between iron concentration and R_1 was

observed in the basal ganglia, supporting prior findings on the paramagnetic effects of iron on relaxation rates.

- However, further analysis suggested that this relationship may be largely driven by regional clustering of iron levels, rather than by continuous within-region variation.

Despite these findings, methodological limitations—such as imprecise temperature measurements, unmodeled covariates (e.g., PMI, hydration, myelin), and substantial inter-subject variability—should be considered when interpreting the results, as they may affect the robustness of linear model estimates without necessarily diminishing the biological relevance of the observed trends.

Overall, these results highlight the complex interplay between thermal dynamics, tissue composition, and magnetic properties in shaping post-mortem relaxation behavior. They also emphasize the importance of multimodal approaches and stratified analyses in studies aiming to bridge imaging and histological measures in neuropathology.

Future work should prioritize the integration of more precise physiological monitoring (e.g., real-time brain temperature) and improved characterization of tissue microstructure, while leveraging the available complementary imaging modalities already included in this dataset, such as diffusion tensor imaging (DTI) and magnetic resonance spectroscopy (MRS). The addition of further techniques, including quantitative susceptibility mapping (QSM), may help refine the interpretation of post-mortem MRI data and strengthen its translational relevance for validating in vivo biomarkers and advancing our understanding of neurodegenerative diseases.

Bibliography

[1] Carsten Stüber et al. "Myelin and iron concentration in the human brain: A quantitative study of MRI contrast". In: *NeuroImage* 93 (2014), pp. 95–106. ISSN: 1053-8119. DOI: https://doi.org/10.1016/j.neuroimage.2014.02.026. URL: https://www.sciencedirect.com/science/article/pii/S1053811914001359.

[2] Cornelia Laule et al. "Magnetic Resonance Imaging of Myelin". In: *Neurotherapeutics* 4.3 (2007). Advances in Neuroimaging/Neuroethics, pp. 460–484. ISSN: 1878-7479. DOI: https://doi.org/10.1016/j.nurt.2007.05.004. URL: https://www.sciencedirect.com/science/article/pii/S1878747923006463.

[3] Kenneth P Whittall et al. "In vivo measurement of T2 distributions and water contents in normal human brain". In: *Magnetic Resonance in Medicine* 37.1 (1997), pp. 34–43. DOI: https://doi.org/10.1002/mrm.1910370107. eprint: https://onlinelibrary.wiley.com/doi/pdf/10.1002/mrm.1910370107. URL: https://onlinelibrary.wiley.com/doi/abs/10.1002/mrm.1910370107.

[4] Shachar Moskovich, Oshrat Shtangel, and Aviv A. Mezer. "Approximating R1 and R2: A Quantitative Approach to Clinical Weighted MRI". In: *Human Brain Mapping* 45.18 (2024). e70102 HBM-24-0824.R1, e70102. DOI: https://doi.org/10.1002/hbm.70102. eprint: https://onlinelibrary.wiley.com/doi/pdf/10.1002/hbm.70102. URL: https://onlinelibrary.wiley.com/doi/abs/10.1002/hbm.70102.

[5] Norihiko Saito et al. "Comparative Study of Postmortem MRI and Pathological Findings in Malignant Brain Tumors". en. In: *Cureus* (Mar. 2024).

ISSN: 2168-8184. DOI: 10.7759/cureus.56241. URL: https://www.cureus.com/articles/237492-comparative-study-of-postmortem-mri-and-pathological-findings-in-malignant-brain-tumors.

[6] Tomoya Kobayashi et al. "Characteristic signal intensity changes on postmortem magnetic resonance imaging of the brain". In: *Japanese Journal of Radiology* 28.1 (2010), pp. 8–14. DOI: 10.1007/s11604-009-0373-9. URL: https://doi.org/10.1007/s11604-009-0373-9.

[7] K. Tashiro et al. "Cerebral relaxation times from postmortem MR imaging of adults". In: *Magn Reson Med Sci* 14.1 (2015), pp. 51–56. DOI: 10.2463/mrms.2013-0126. eprint: https://doi.org/10.2463/mrms.2013-0126.

[8] T. D. Ruder et al. "The influence of body temperature on image contrast in post mortem MRI". In: *European Journal of Radiology* 81.6 (2012), pp. 1366–1370. DOI: 10.1016/j.ejrad.2011.02.062.

[9] C. Birkl et al. "Temperature Dependency of T1 Relaxation Time in Unfixed and Fixed Human Brain Tissue". In: *Biomed Tech (Berl)* 58.Suppl 1 (2013). DOI: 10.1515/bmt-2013-4290. URL: https://doi.org/10.1515/bmt-2013-4290.

[10] C. Berger et al. "Post mortem brain temperature and its influence on quantitative MRI of the brain". In: *MAGMA* 35.3 (2022), pp. 375–387. DOI: 10.1007/s10334-021-00971-8.

[11] Frank Shellock. "Radiofrequency Energy-Induced Heating During MR Procedures: A Review". In: *Journal of Magnetic Resonance Imaging* 12 (July 2000), pp. 30–36. DOI: 10.1002/1522-2586(200007)12:1<30::AID-JMRI4>3.0.CO;2-S.

[12] In: *Journal of Avian Medicine and Surgery* 39.1 (Mar. 2025). ISSN: 1082-6742. DOI: 10.1647/1082-6742-39.1.58. URL: https://bioone.org/journals/journal-of-avian-medicine-and-surgery/volume-39/issue-1/1082-6742-39.1.58/Editorial-Policy-Submission-

Requirements-and-Instructions-to-Authors-Updated-March/10.1647/1082-6742-39.1.58.full.

[13] R.J. Ogg and R.G. Steen. "Age-related changes in brain T1 are correlated with iron concentration". In: *Magn Reson Med* 40.5 (1998), pp. 749–753. DOI: 10.1002/mrm.1910400516.

[14] J Vymazal et al. "The quantitative relation between T1-weighted and T2-weighted MRI of normal gray matter and iron concentration". In: *Journal of Magnetic Resonance Imaging* 5.5 (1995), pp. 554–560. DOI: 10.1002/jmri.1880050514.

[15] Sam Mugiraneza and Alannah M. Hallas. "Tutorial: a beginner's guide to interpreting magnetic susceptibility data with the Curie-Weiss law". In: *Communications Physics* 5.1 (2022), p. 95. ISSN: 2399-3650. DOI: 10.1038/s42005-022-00853-y. URL: https://doi.org/10.1038/s42005-022-00853-y.

[16] Neil Gelman et al. "Interregional variation of longitudinal relaxation rates in human brain at 3.0 T: Relation to estimated iron and water contents". In: *Magnetic Resonance in Medicine* 45.1 (2001), pp. 71–79. DOI: https://doi.org/10.1002/1522-2594(200101)45:1<71::AID-MRM1011>3.0.CO;2-2. eprint: https://onlinelibrary.wiley.com/doi/pdf/10.1002/1522-2594%28200101%2945%3A1%3C71%3A%3AAID-MRM1011%3E3.0.CO%3B2-2. URL: https://onlinelibrary.wiley.com/doi/abs/10.1002/1522-2594%28200101%2945%3A1%3C71%3A%3AAID-MRM1011%3E3.0.CO%3B2-2.

[17] Josef Vymazal et al. "T1 and T2 in the Brain of Healthy Subjects, Patients with Parkinson Disease, and Patients with Multiple System Atrophy: Relation to Iron Content". en. In: *Radiology* 211.2 (May 1999), pp. 489–495. ISSN: 0033-8419, 1527-1315. DOI: 10.1148/radiology.211.2.r99ma53489. URL: http://pubs.rsna.org/doi/10.1148/radiology.211.2.r99ma53489.

[18] National Institute of Biomedical Imaging and Bioengineering. *Magnetic Resonance Imaging (MRI)*. Accessed: 2024-02-19. 2024. URL: https://www.nibib.nih.gov/science-education/science-topics/magnetic-resonance-imaging-mri.

[19] Paul S. Tofts. *Quantitative MRI of the brain: Measuring changes caused by disease*. Chichester, UK: Wiley, 2003. ISBN: 978-0-470-84721-3.

[20] T. R. Nelson and S. M. Tung. "Temperature dependence of proton relaxation times in vitro". In: *Magn Reson Imaging* 5.3 (1987), pp. 189–199. DOI: 10.1016/0730-725X(87)90020-8.

[21] A. Lazari and I. Lipp. "Can MRI measure myelin? Systematic review, qualitative assessment, and meta-analysis of studies validating microstructural imaging with myelin histology". In: *Neuroimage* 230 (2021), p. 117744. DOI: 10.1016/j.neuroimage.2021.117744. URL: https://doi.org/10.1016/j.neuroimage.2021.117744.

[22] Jiri Vymazal et al. "The relation between brain iron and NMR relaxation times: an in vitro study". In: *Magnetic Resonance in Medicine* 35.1 (1996), pp. 56–61. DOI: 10.1002/mrm.1910350108.

[23] Alan P. Manning, Alex L. MacKay, and Carl A. Michal. "Understanding aqueous and non-aqueous proton T1 relaxation in brain". In: *Journal of Magnetic Resonance* 323 (2021), p. 106909. ISSN: 1090-7807. DOI: https://doi.org/10.1016/j.jmr.2020.106909. URL: https://www.sciencedirect.com/science/article/pii/S1090780720302275.

[24] F. Kühne et al. "Assessment of myelination in infants and young children by T1 relaxation time measurements using the magnetization-prepared 2 rapid acquisition gradient echoes sequence". In: *Pediatric Radiology* 51.11 (2021), pp. 2058–2068. DOI: 10.1007/s00247-021-05109-5. URL: https://doi.org/10.1007/s00247-021-05109-5.

[25] H. Neeb, K. Zilles, and N. J. Shah. "A new method for fast quantitative mapping of absolute water content in vivo". In: *NeuroImage* 31.3 (2006), pp. 1156–1168. DOI: 10.1016/j.neuroimage.2005.12.063. eprint:

2006May2. URL: https://doi.org/10.1016/j.neuroimage.2005.12.063.

[26] P. J. Wright et al. "Water proton T1 measurements in brain tissue at 7, 3, and 1.5T using IR-EPI, IR-TSE, and MPRAGE: results and optimization". In: *Magnetic Resonance Materials in Physics, Biology and Medicine* 21.1 (2008), pp. 121–131. ISSN: 1352-8661. DOI: 10.1007/s10334-008-0104-8. URL: https://doi.org/10.1007/s10334-008-0104-8.

[27] Chen Lin et al. "Measurements of T1 Relaxation times at 3.0T: Implications for clinical MRA". In: *Proceedings of ISMRM*. Mayo Clinic. 2008.

[28] Christian Jackowski et al. "Virtopsy: postmortem imaging of the human heart in situ using MSCT and MRI". In: *Forensic Science International* 149.1 (2005), pp. 11–23. ISSN: 0379-0738. DOI: https://doi.org/10.1016/j.forsciint.2004.05.019. URL: https://www.sciencedirect.com/science/article/pii/S037907380400341X.

[29] Hamid Jalalzadeh et al. "Post-mortem imaging compared with autopsy in trauma victims – A systematic review". In: *Forensic Science International* 257 (2015), pp. 29–48. ISSN: 0379-0738. DOI: https://doi.org/10.1016/j.forsciint.2015.07.026. URL: https://www.sciencedirect.com/science/article/pii/S0379073815003047.

[30] Alard Roebroeck, Karla L. Miller, and Mayank Aggarwal. "Ex vivo diffusion MRI of the human brain: Technical challenges and recent advances". In: *NMR in Biomedicine* 32.4 (2019). Epub 2018 Jun 4, e3941. DOI: 10.1002/nbm.3941.

[31] Stefan W. Rieger et al. "A temperature-controlled cooling system for accurate quantitative post-mortem MRI". In: *Magnetic Resonance in Medicine* 90.6 (2023). Epub 2023 Aug 2, pp. 2643–2652. DOI: 10.1002/mrm.29816.

[32] Brian L. Edlow et al. “7 Tesla MRI of the ex vivo human brain at 100 micron resolution”. In: *Scientific Data* 6.1 (2019), p. 244. DOI: 10.1038/s41597-019-0254-8.

[33] Simon Foxley et al. “Improving diffusion-weighted imaging of post-mortem human brains: SSFP at 7 T”. In: *NeuroImage* 102 Pt 2 (Nov. 2014), pp. 579–589. DOI: 10.1016/j.neuroimage.2014.08.014.

[34] Wenchuan Wu et al. “High-resolution diffusion imaging in the unfixed post-mortem infant brain at 7 T”. In: *Imaging Neuroscience* 2 (Jan. 2024), pp. 1–20. ISSN: 2837-6056. DOI: 10.1162/imag_a_00069. eprint: https://direct.mit.edu/imag/article-pdf/doi/10.1162/imag_a_00069/2216708/imag_a_00069.pdf. URL: https://doi.org/10.1162/imag%5C_a%5C_00069.

[35] E. Moser et al. “Temperature- and pH-dependence of proton relaxation rates in rat liver tissue”. In: *Magnetic Resonance Imaging* 13.3 (1995), pp. 429–440. DOI: 10.1016/0730-725x(94)00135-p.

[36] C. Birkl et al. “Effects of formalin fixation and temperature on MR relaxation times in the human brain”. In: *NMR Biomed* 29.4 (2016), pp. 458–465. DOI: 10.1002/nbm.3477.

[37] R. J. Dawe et al. “Postmortem MRI of human brain hemispheres: T2 relaxation times during formaldehyde fixation”. In: *Magn Reson Med* 61.4 (2009), pp. 810–818. DOI: 10.1002/mrm.21909.

[38] Jan Klohs and Ann M. Hirt. “Investigation of the magnetic susceptibility properties of fresh and fixed mouse heart, liver, skeletal muscle and brain tissue”. In: *Physica Medica* 88 (2021), pp. 37–44. ISSN: 1120-1797. DOI: https://doi.org/10.1016/j.ejmp.2021.06.014. URL: https://www.sciencedirect.com/science/article/pii/S1120179721002362.

[39] Paul E. Thelwall et al. “Effects of temperature and aldehyde fixation on tissue water diffusion properties, studied in an erythrocyte ghost tissue model”. In: *Magnetic Resonance in Medicine* 56.2 (Aug. 2006), pp. 282–289. DOI: 10.1002/mrm.20962.

[40] Heinz Fraenkel-Conrat and Howard S. Olcott. “The reaction of formaldehyde with proteins; cross-linking between amino and primary amide or guanidyl groups”. In: *Journal of the American Chemical Society* 70.8 (Aug. 1948), pp. 2673–2684. DOI: 10.1021/ja01188a018.

[41] Yves Gossuin et al. “Relaxation induced by ferritin and ferritin-like magnetic particles: the role of proton exchange”. In: *Magn Reson Med* 43.2 (2000), pp. 237–243. DOI: 10.1002/(sici)1522-2594(200002)43:2<237::aid-mrm10>3.0.co;2-5.

[42] P. A. Bottomley et al. “A review of normal tissue hydrogen NMR relaxation times and relaxation mechanisms from 1-100 MHz: dependence on tissue type, NMR frequency, temperature, species, excision, and age”. In: *Medical Physics* 11.4 (1984), pp. 425–448. DOI: 10.1118/1.595535.

[43] Ian R. Young et al. “Modeling and observation of temperature changes in vivo using MRI”. In: *Magnetic Resonance in Medicine* 32.3 (Sept. 1994), pp. 358–369. DOI: 10.1002/mrm.1910320311.

[44] Carlo Pietro Campobasso, Giancarlo Di Vella, and Francesco Introna. “Factors affecting decomposition and Diptera colonization”. In: *Forensic Science International* 120.1 (2001). Forensic Entomology, pp. 18–27. ISSN: 0379-0738. DOI: https://doi.org/10.1016/S0379-0738(01)00411-X. URL: https://www.sciencedirect.com/science/article/pii/S037907380100411X.

[45] P. M. Flach et al. “Deep Into the Fibers! Postmortem Diffusion Tensor Imaging in Forensic Radiology”. In: *American Journal of Forensic Medicine and Pathology* 36.3 (2015), pp. 153–161. DOI: 10.1097/PAF.0000000000000177.

[46] J. R. Busch et al. “Post-mortem MRI-based volumetry of the hippocampus in forensic cases of decedents with severe mental illness”. In: *Forensic Science, Medicine, and Pathology* 15.2 (2019), pp. 213–217. DOI: 10.1007/s12024-019-00101-w.

[47] E. Scheurer et al. “Forensic application of postmortem diffusion-weighted and diffusion tensor MR imaging of the human brain in situ”. In: *AJNR American Journal of Neuroradiology* 32.8 (2011), pp. 1518–1524. DOI: 10.3174/ajnr.A2508.

[48] W. D. Zech et al. “Post-mortem 1.5T MR quantification of regular anatomical brain structures”. In: *International Journal of Legal Medicine* 130.4 (2016), pp. 1071–1080. DOI: 10.1007/s00414-016-1318-3.

[49] P. S. Tofts et al. “Imaging cadavers: cold FLAIR and noninvasive brain thermometry using CSF diffusion”. In: *Magnetic Resonance in Medicine* 59.1 (2008), pp. 190–195. DOI: 10.1002/mrm.21456.

[50] C. Berger et al. “Temperature correction of post mortem quantitative magnetic resonance imaging using real-time forehead temperature acquisitions”. In: *Forensic Science International* 348 (2023), p. 111738. DOI: 10.1016/j.forsciint.2023.111738.

[51] Robert R Crichton and Johan R Boelaert. *Inorganic biochemistry of iron metabolism: from molecular mechanisms to clinical consequences*. John Wiley & Sons, 2001.

[52] Vanessa Wiggermann. “Chapter 3 - Iron imaging in neuroinflammation”. In: *Imaging Neuroinflammation*. Ed. by Cornelia Laule and John D. Port. Vol. 9. Advances in Magnetic Resonance Technology and Applications. Academic Press, 2023, pp. 51–78. DOI: https://doi.org/10.1016/B978-0-323-91771-1.00013-7. URL: https://www.sciencedirect.com/science/article/pii/B9780323917711000137.

[53] Christian Langkammer et al. “Quantitative susceptibility mapping (QSM) as a means to measure brain iron? A post mortem validation study”. In: *NeuroImage* 62.3 (2012), pp. 1593–1599. DOI: 10.1016/j.neuroimage.2012.05.049. URL: https://www.sciencedirect.com/science/article/pii/S105381191200537X.

[54] B. Hallgren and P. Sourander. “The effect of age on the non-haemin iron in the human brain”. In: *J Neurochem* 3.1 (1958), pp. 41–51. DOI: 10.1111/j.1471-4159.1958.tb12607.x.

[55] C. Quintana et al. “Study of the localization of iron, ferritin, and hemosiderin in Alzheimer’s disease hippocampus by analytical microscopy at the subcellular level”. In: *J Struct Biol.* 153.1 (2006), pp. 42–54. DOI: 10.1016/j.jsb.2005.11.001.

[56] C. Langkammer et al. “Susceptibility induced gray-white matter MRI contrast in the human brain”. In: *NeuroImage* 59.2 (2012), pp. 1413–1419. DOI: 10.1016/j.neuroimage.2011.08.045.

[57] J Fisher et al. “Ferritin: a novel mechanism for delivery of iron to the brain and other organs”. In: *American Journal of Physiology-Cell Physiology* 293.2 (Aug. 2007), pp. C641–C649. DOI: 10.1152/ajpcell.00599.2006.

[58] T. Moos. “Brain iron homeostasis”. In: *Dan Med Bull* 49.4 (2002), pp. 279–301.

[59] M. Sánchez et al. “Iron chemistry at the service of life”. In: *IUBMB Life* 69.6 (2017), pp. 382–388. DOI: 10.1002/iub.1602.

[60] G. Bartzokis et al. “Brain ferritin iron as a risk factor for age at onset in neurodegenerative diseases”. In: *Annals of the New York Academy of Sciences* 1012 (2004), pp. 224–236. DOI: 10.1196/annals.1306.019.

[61] R. J. Ward et al. “The role of iron in brain ageing and neurodegenerative disorders”. In: *Lancet Neurol.* 13.10 (2014), pp. 1045–1060. DOI: 10.1016/S1474-4422(14)70117-6.

[62] David Berg and Moussa B. Youdim. “Role of iron in neurodegenerative disorders”. In: *Topics in Magnetic Resonance Imaging* 17.1 (Feb. 2006), pp. 5–17. DOI: 10.1097/01.rmr.0000245461.90406.ad.

[63] M. Khalil et al. “Determinants of brain iron in multiple sclerosis: a quantitative 3T MRI study”. In: *Neurology* 77.18 (Nov. 2011), pp. 1691–1697. DOI: 10.1212/WNL.0b013e318236ef0e.

[64] J. Wang and K. Pantopoulos. “Regulation of cellular iron metabolism”. In: *Biochemical Journal* 434.3 (2011), pp. 365–381. DOI: 10.1042/BJ20101825.

[65] D. Aquino et al. “Age-related iron deposition in the basal ganglia: quantitative analysis in healthy subjects”. In: *Radiology* 252.1 (2009), pp. 165–172. DOI: 10.1148/radiol.2522081399.

[66] J. R. Conde and W. J. Streit. “Microglia in the aging brain”. In: *Journal of Neuropathology and Experimental Neurology* 65.3 (2006), pp. 199–203. DOI: 10.1097/01.jnen.0000202887.22082.63.

[67] Andrew J. Farrall and Joanna M. Wardlaw. “Blood–brain barrier: Ageing and microvascular disease – systematic review and meta-analysis”. In: *Neurobiology of Aging* 30.3 (2009), pp. 337–352. ISSN: 0197-4580. DOI: https://doi.org/10.1016/j.neurobiolaging.2007.07.015. URL: https://www.sciencedirect.com/science/article/pii/S0197458007002904.

[68] SH Koenig et al. “Relaxometry of ferritin solutions and the influence of the Fe3+ core ions”. In: *Magnetic Resonance in Medicine* 3.5 (1986), pp. 755–767. DOI: 10.1002/mrm.1910030511.

[69] B Drayer et al. “MRI of brain iron”. In: *American Journal of Roentgenology* 147.1 (1986). PMID: 3487201, pp. 103–110. DOI: 10.2214/ajr.147.1.103.

[70] R.Grant Steen, Wilburn E Reddick, and Robert J Ogg. “More than meets the eye: significant regional heterogeneity in human cortical T1 ”. In: *Magnetic Resonance Imaging* 18.4 (2000), pp. 361–368. ISSN: 0730-725X. DOI: https://doi.org/10.1016/S0730-725X(00)00123-5. URL: https://www.sciencedirect.com/science/article/pii/S0730725X00001235.

[71] Christian Langkammer et al. “Quantitative MR imaging of brain iron: a postmortem validation study”. In: *Radiology* 257.2 (Nov. 2010). Erratum

in: Radiology. 2011 Mar;258(3):962, pp. 455–462. DOI: 10.1148/radiol.10100495.

[72] Jongho Lee et al. “The contribution of myelin to magnetic susceptibility-weighted contrasts in high-field MRI of the brain”. In: *NeuroImage* 59.4 (Feb. 2012), pp. 3967–3975. DOI: 10.1016/j.neuroimage.2011.10.076.

[73] Chunlei Liu et al. “High-field (9.4 T) MRI of brain dysmyelination by quantitative mapping of magnetic susceptibility”. In: *NeuroImage* 56.3 (June 2011), pp. 930–938. DOI: 10.1016/j.neuroimage.2011.02.024.

[74] Ferdinand Schweser et al. “Quantitative imaging of intrinsic magnetic tissue properties using MRI signal phase: An approach to in vivo brain iron metabolism?” In: *NeuroImage* 54.4 (2011), pp. 2789–2807. ISSN: 1053-8119. DOI: https://doi.org/10.1016/j.neuroimage.2010.10.070. URL: https://www.sciencedirect.com/science/article/pii/S1053811910013789.

[75] M. Ali et al. “Temperature Dependence of R1, R2* and Magnetic Susceptibility in Ferritin-Doped Agar Phantoms at 7T”. In: *Proceedings of the 24th Annual Meeting of ISMRM*. Abstract. 2016, p. 1528. URL: https://archive.ismrm.org/2016/1528.html.

[76] C. Henssge et al. “Todeszeitbestimmung durch Messung der zentralen Hirntemperatur [Determination of the time of death by measurement of central brain temperature]”. German. In: *Zeitschrift für Rechtsmedizin* 93.1 (1984), pp. 1–22. DOI: 10.1007/BF00202979.

[77] Stephen M. Smith et al. “Advances in functional and structural MR image analysis and implementation as FSL”. In: *NeuroImage* 23.Suppl 1 (2004), S208–S219. ISSN: 1053-8119. DOI: 10.1016/j.neuroimage.2004.07.051.

[78] Celine Berger et al. “Investigation of post mortem brain, rectal and forehead temperature relations”. In: *Journal of Thermal Biology* 115 (2023), p. 103615. ISSN: 0306-4565. DOI: https://doi.org/10.1016/j.

jtherbio.2023.103615. URL: https://www.sciencedirect.com/science/article/pii/S0306456523001560.

[79] Frank G Shellock and John V Crues. "MR procedures: biologic effects, safety, and patient care". In: *Radiology* 232.3 (2004), pp. 635–652.

[80] H. Neeb, K. Zilles, and N.J. Shah. "A new method for fast quantitative mapping of absolute water content in vivo". In: *NeuroImage* 31.3 (2006), pp. 1156–1168. ISSN: 1053-8119. DOI: https://doi.org/10.1016/j.neuroimage.2005.12.063. URL: https://www.sciencedirect.com/science/article/pii/S1053811906000176.

[81] Heiko Neeb, Karl Zilles, and N. Jon Shah. "Fully-automated detection of cerebral water content changes: Study of age- and gender-related H2O patterns with quantitative MRI". In: *NeuroImage* 29.3 (2006), pp. 910–922. ISSN: 1053-8119. DOI: https://doi.org/10.1016/j.neuroimage.2005.08.062. URL: https://www.sciencedirect.com/science/article/pii/S105381190500594X.

[82] Timothy M. Shepherd et al. "Postmortem interval alters the water relaxation and diffusion properties of rat nervous tissue — Implications for MRI studies of human autopsy samples". In: *NeuroImage* 44.3 (2009), pp. 820–826. ISSN: 1053-8119. DOI: https://doi.org/10.1016/j.neuroimage.2008.09.054. URL: https://www.sciencedirect.com/science/article/pii/S1053811908010628.

[83] R. J. Dawe et al. "Postmortem MRI of human brain hemispheres: T2 relaxation times during formaldehyde fixation". In: *Magnetic Resonance in Medicine* 61.4 (Apr. 2009), pp. 810–818. DOI: 10.1002/mrm.21909.